# Novel Synthesis of Silica-Supported Fischer-Tropsch Catalysts for Second Generation Biofuels

By

**Phylander Omosigho Atubi**


A thesis submitted to the University of Huddersfield

in partial fulfilment of the requirements for

the degree of Doctor of Philosophy

**January 2015**

The Department of Chemical Sciences

University of Huddersfield

Queensgate

Huddersfield HD1 3DH

# COPYRIGHT STATEMENT

i. The author of this thesis owns any copyright in it (the "Copyright") and he has given the University of Huddersfield the right to use such Copyright for any administrative, promotional and/or teaching purposes.

ii. Copies of this thesis, either in full or in extracts, may be made only in accordance with the regulations of the University Library. Details of these regulations may be obtained from the Librarian and this page must form part of any such copies made.

# ABSTRACT

The objective of this study is to improve the catalytic performance of silica-supported Fischer-Tropsch cobalt based catalyst. Iron and nickel catalyst were also briefly studied.

Initial work focused on synthesis of porous silica via oxidative thermal decomposition of polydimethylsiloxane (PDMS) and its characterisation. It was shown that PDMS undergoes at least two thermal degradation steps to form silica powder. It was also demonstrated that increase in isothermal time at constant temperature and increase in temperature at constant time could be used to tune the surface area and pore volume of the synthesized silica powder.

Subsequently, a novel one pot technique called the swelling in method (SIM) was developed, and employed to synthesize silica-supported cobalt, iron and nickel based Fischer-Tropsch catalyst. The results of silica-supported cobalt based catalyst prepared by the swelling in method were compared with those synthesized by incipient wet impregnation method. The colloidal method was also combined with the swelling in method to prepare silica-supported cobalt nanoparticles catalyst.

Characterisation of cobalt, iron and nickel based catalyst prepared by the swelling in method showed that PDMS as the initial catalyst support converted to silica powder after oxidative calcination. Physicochemical properties of silica-supported cobalt, iron and nickel catalyst prepared by the swelling in method suggest that the oxides of each metal were present inside the silica pores while cobalt based catalyst prepared by the same method had better surface area and pore volume compared to the catalyst synthesized by the incipient wetness impregnation technique.

Catalytic performance of the catalyst synthesized by the swelling in and incipient wetness methods were studied in High Temperature Fischer-Tropsch synthesis reaction condition.

The results showed that silica-supported cobalt based catalyst prepared by the swelling in method was overall more active, generated less methane and less susceptible to deactivation by sintering and carbon deposition when compared to the catalyst prepared by the impregnation technique. Silica-supported cobalt nanoparticles catalyst had the best catalytic activity in comparison to all the catalyst studied in this work. Silica-supported cobalt based catalyst prepared by the swelling in method using cobalt nitrate exhibited the best catalytic activity while the catalyst synthesized from cobalt acetate had the least activity. The addition of ruthenium to silica-supported cobalt catalyst contributed in minimising the formation of methane when compared to the catalyst without ruthenium. Silica-supported iron and nickel based catalyst showed reasonable catalytic activity, and as expected the amount of methane generated by nickel catalyst was relatively very high compared to all the catalyst studied in this thesis.

# ACKNOWLEDGEMENTS

I sincerely thank Dr Daniel John Belton (my main supervisor) and Dr Gareth Parkes (my second supervisor) for all their relentless support and contributions throughout the period of my PhD. My appreciation also goes to James Rooney for all his help and valuable intellectual inputs. My heart felt gratitude also goes to Professor Robert Brown for his fatherly intervention during my moments of difficulties. I would also like to thank some of the departmental technicians in the persons of Margaret Scott and Ibrahim George, who were always there to give a helping hand as and when necessary.

Meanwhile, I deeply appreciate my parents for giving me the privilege of reaching this academic height and also to my brother Justice for being there at all times.

But most importantly, my profound gratitude goes to the almighty God who gave me life and good health to see this dream to the end.

# DEDICATION

I would like to dedicate this thesis to my lovely wife, Evumena and my two beautiful daughters, Faith and Victory for all their prayers, encouragement and support during the period of this work.

I would also like to dedicate this work to Mr and Mrs Shittu and family, Dr and Dr Rotimi and family, Mr and Mrs Yusuf and family, OFNC Leeds youth fellowship members and their parents and to every member of the Overseas Fellowship of Nigerian Christians (OFNC) Leeds branch as well as to Dr and Dr Okoye and family for your palpable agape love shown to me and my family when we really needed it.

# LIST OF FIGURES

# LIST OF TABLES

# ABBREVIATIONS

| | |
|---|---|
| APCI | Atmospheric Pressure Chemical Ionization |
| APPI | Atmospheric Pressure Photoionization |
| ASF | Anderson Schulz Flory |
| ATR-FTIR | Attenuated Total Reflectance Fourier Transform Infrared |
| BET | Braunauer Emmett Teller |
| BJH | Barrett Joyner Halenda |
| CCS | Carbon Capture and Storage |
| CI | Chemical Ionization |
| Co-A | Cobalt acetate |
| Co-AA | Cobalt acetylacetonate |
| Co-N | Cobalt nitrate |
| CTL | Coal to liquid |
| DME | Dimethyl ether |
| DR | Dubinin-Radushkevich |
| DTG | Differential Thermogravimetry |
| EEA | European Environment Agency |
| EI | Electron Ionization |
| ESI | Electrospray Ionization |
| EU | European Union |
| EXAFS | Extended X-ray Absorption Fine Structure |
| FAB | Fast Atom Bombardment |
| FDI | Field Desorption Ionization |
| FFVs | Flexible Fuel Vehicles |

| | |
|---|---|
| FTS Synthesis | Fischer-Tropsch |
| GTL | Gas to liquid |
| HK | Horvath-Kawazoe |
| HTFT | High Temperature Fischer Tropsch |
| IWIM | Incipient wetness impregnation method |
| LTFT | Low Temperature Fischer Tropsch |
| MALDI | Matrix Assisted Laser Desorption Ionization |
| MPV | Micropore Volume |
| MS | Mass Spectrometry |
| MWCNT | Multiwalled Carbon Nanutubes |
| PDI | Plasma Desorption Ionization |
| PDMS | Polydimethylsiloxane |
| PEG | Polyethylene glycol |
| PMMOS | Polymethylmethoxysiloxane |
| Pw | Pore Width |
| p-XRD | Powder X-ray Diffraction |
| S.A | Surface Area |
| SASOL | South African Synthetic Oil Limited |
| SBA | Santa Barbara Amorphous |
| SHS | Silica hollow sphere |
| SIM | Swelling in method |
| SIMS | Secondary Ion Mass Spectrometry |
| SNG | Synthetic natural gas |
| TEM | Transmission Electron Microscopy |

| | |
|---|---|
| TG | Thermogravimetry |
| TGA | Thermogravimetry analysis |
| TOF | Turn over frequency |
| TPR | Temperature programmed reduction |
| TPV | Total Pore Volume |
| TW | Terawatts |
| WGS | Water gas shift |
| ZSM | Zeolite Socony Mobil |

# CONTENTS

# CHAPTER 1

# Introduction

---

This chapter covers the background, overview, overall objective as well as the specific objectives of this research work.

## 1.1. Background

At the present time there is scientific agreement about the damage caused by carbon dioxide and other greenhouse gases to the environment as a result of world dependence on fossil fuels to generate energy [1]. In 2009 fossil fuels generated almost 80% of the 16 terawatts (TW) of energy used worldwide with its combustion releasing about 7.8 billion metric tons of carbon [2]. These numbers are set to ascend due to population growth, regardless of invented technologies aimed to encourage efficient use of energy [3, 4]. To overcome this enormous challenge, it is expedient to introduce a range of new $CO_2$ constrained technologies for energy supplies [1, 5].

Biofuels have emerged as a viable solution to this problem. European countries commitments to the Kyoto protocol have also made biofuels development a priority as to achieve the indented targets for energy policies and emission reduction. This focus on renewable energy production aims to establish sustainable and an environmentally green source of energy for the industry and consumer societies [5].

First generation biofuels consisting of biodiesel and bioethanol have received substantial attention, but the competition between first generation biofuels and the food production industries over the issues for feedstocks availability as well as the possible increase in food prices due to the use of these materials for fuel production, has left serious questions over this innovation [6] .

Meanwhile, second generation biofuels produced from agricultural lignocellulosic biomass, which is derived from a variety of waste materials as feed-stocks, can help to resolve the issue of increase in food prices and to ensure sustainable production of biofuels. Large scale production of second generation biofuels is potentially comparable with standard petrol,

diesel and could be a very cost effective route to generate low carbon and renewable energy as transportation fuel [6].

Fischer-Tropsch Synthesis (FTS), which involves the transformation of a synthesis gas mixture ($CO + H_2$) into liquid hydrocarbon, is one feasible route of producing second generation biofuels. These fuels are potential alternative to fossil fuels which are globally known for $CO_2$ emission [1, 5].

Cobalt, iron and nickel in descending order have been proposed as catalysts for FT synthesis. Cobalt has received the most attention due to its high activity and selectivity towards linear hydrocarbons, high resistance to deactivation as well as low activity in respect to the water gas shift reaction, while on the other hand, nickel is least recommended because of its high methane formation [7, 8]. It has been extensively reported that the performance of these supported catalysts in Fischer-Tropsch synthesis strongly depends on their routes of preparation. Meanwhile, as Fischer-Tropsch reaction are highly exothermic, there is the possible problem of catalyst deactivation such as sintering while on stream which presents the challenge for catalyst stability and lifetime [8, 9]. As such, research is still needed in developing an innovative and robust route to synthesize these catalysts and also to carry out their characterisation.

In the last decade, various methods such as vapor-deposition, impregnation, plasma, co-precipitation and gas-phase incorporation have been reported for the design of silica-supported cobalt, iron and nickel catalysts for Fischer-Tropsch synthesis [10-16]. However, the vast majority of these catalysts focused on the conventional impregnation method [12, 13, 15, 16]. While most of these reported approaches seem very promising, it cannot be disputed that they are very time consuming, with lengthy periods of drying and the apparent problem of catalyst deactivation caused by calcination is still not being addressed.

In this research work, we report a facile and novel one-step process called the swelling in method (SIM) for the synthesis and characterisation of silica-supported cobalt, iron as well as nickel catalysts for Fischer-Tropsch synthesis. This method and the incipient wetness impregnation technique were used to prepare and characterise 2.5wt.%, 5wt.% and 10wt.% $Co/SiO_2$ using three types of cobalt precursors. Fischer-Tropsch synthesis was used to compare the performance of the catalysts synthesized via both methods. The swelling in method was also used to prepare and characterise iron and nickel based silica-supported catalysts and their catalytic performance were investigated using Fischer-Tropsch synthesis. Finally, the swelling in method was combined with the bottom up approach to synthesis and characterise 2.5wt%, 5wt% and 10wt% silica-supported cobalt nanoparticles. Fischer-Tropsch synthesis was also used to test the performance of these catalysts.

## 1.2. Overview

This work was motivated by the need to enhance stability and life time of catalysts used for Fischer-Tropsch synthesis. This need instigated our quest for an alternative and innovative route of preparing these catalysts. Although, iron and nickel metals were employed in this work, the entirety of this project was centred around cobalt based catalyst for Fischer-Tropsch synthesis.

At the beginning of this research, an extensive study on the thermal synthesis and characterisation of porous silica via oxidative decomposition of polydimethylsiloxane (PDMS) was carried out. Thermogravimetry (TG) was used to investigate the degradation profile of this polymer at different temperature and time. Attenuated Total Reflectance Fourier Transform Infrared Spectroscopy (ATR-FTIR), Powder X-ray diffraction (p-XRD) and $N_2$ adsorption were used to characterise the prepared silica. This route of preparing silica

powder was considered to have potential application for a one step synthesis of silica-supported catalyst for Fischer-Tropsch synthesis.

Subsequently, the focus was aimed at the development of a novel one step technique called the swelling in method (SIM) which was used to synthesis various amounts (wt.%) of $Co/SiO_2$ catalysts using different precursors, different weight percent of $Fe/SiO_2$ and $Ni/SiO_2$ catalysts were also prepared through this route. For the purpose of comparison, $Co/SiO_2$ catalysts were prepared by incipient wetness impregnation procedure. The bottom up approach coupled with the developed method (SIM) was used to prepare another set of $Co/SiO_2$ catalyst. All the prepared catalysts were characterised by FTIR, XRD, TG and $N_2$ physisorption. The Mass Spectrometry was used to screen the catalytic performance of the catalysts.

Finally, some of the cobalt based catalyst prepared by the swelling in method was calcined in vacuum under the flow of nitrogen instead of air so as to monitor the effect of calcination environment on the catalyst support. These catalysts were characterised and tested for catalytic performance. Data collection and review was carried out while repeat experiments were performed for confirmation of generated data.

## 1.3. Research objective

### 1.3.1. Overall objectives

To improve the catalytic performance of silica-supported cobalt based catalyst for Fischer-Tropsch synthesis.

1.3.2. Specific objective

1. To synthesis and characterise porous silica powder as catalyst support via thermal oxidative degradation of PDMS.

2. To employ an alternative method for the synthesis of silica-supported cobalt based catalyst.

3. To use the incipient wetness impregnation method to prepare $Co/SiO_2$ catalyst as a control.

4. To characterise and compare the catalytic performance of the various catalysts synthesized via both methods using Fischer-Tropsch synthesis.

5. To use the swelling in method to prepare some ruthenium promoted silica-supported cobalt catalyst and compare their catalytic performance with the catalyst without ruthenium.

6. To use the swelling in method in synthesizing other group 8 metals based silica-supported catalysts.

7. To characterise the group 8 metals based silica-supported catalysts and test their catalytic behaviour using Fischer-Tropsch synthesis.

**References**


1. Caspeta, L.; Buijs, N.A.; Nielsen, J. The role of biofuels in the future energy supply. *Energy & Environmental Science*. **2013**, 6, 1077.
2. Key World Energy Statistics. The International Energy Agency (EIA). *OECD Publishing*, Paris. **2011**, 6, 28.
3. Statistics, I.E.A. $CO_2$ Emissions from Fuel Combustion. The International Energy Agency (EIA). *OECD Publishing*, Paris. **2011**, 9, 45.
4. Lewis, N.S.; Nocera, D.G. Powering the planet: Chemical challenges in solar energy utilization. *Proceedings of the National Academy of Sciences*. **2006**, 103, 15729.
5. Damartzis, T.; Zabaniotou, A. Thermochemical conversion of biomass to second generation biofuels through integrated process design—A review. *Renewable and Sustainable Energy Reviews.* **2011**, 15, 366.
6. Naik, S.; Vaibhav, V.G.; Prasant, K.R.; Ajay, K.D. Production of first and second generation biofuels: a comprehensive review. *Renewable and Sustainable Energy Reviews.* **2010**, 14, 578.
7. Schulz, H. Short history and present trends of Fischer–Tropsch synthesis. *Applied Catalysis A: General.* **1999,** 186, 3.
8. Jahangiri, H.; Bennett, J.; Mahjoubi, P.; Wilson, K.; Gu, S. A review of advanced catalyst development for Fischer-Tropsch synthesis of hydrocarbons from biomass derived syn-gas. *Catalysis Science & Technology.* **2014**, 4, 2210.
9. Hu, J.; Yu, F.; Lu, Y. Application of Fischer–Tropsch Synthesis in Biomass to Liquid Conversion. *Catalysts.* **2012,** 2, 303.
10. Yan, Z.; Wang, Z.; Bukur, D. B.; Goodman, D. W. Fischer–Tropsch synthesis on a model $Co/SiO_2$ catalyst. *Journal of Catalysis*. **2009**, 268, 196.

11. Cheng-Hua, Z.; Yong, Y.; Zhi-Chao, T.; Wei-Xiang, H. Structural properties and reduction behavior of Ni promoted FeMnK/$SiO_2$ catalysts for Fischer-Tropsch synthesis. *Journal of Fuel Chemistry and Technology*. **2006**, 34, 695.

12. Surisetty, V.R.; Kozinski, J.; Dalai, A.K. Novel Ni-Co-Mo-K Catalysts Supported on Multiwalled Carbon Nanotubes for Higher Alcohols Synthesis. *Journal of Catalysts.* **2013**, 1, 1.

13. Tavasoli, A.; Trépanier, M.; Malek Abbaslou, R.M.; Dalai, A.K.; Abatzoglou, N. Fischer–Tropsch synthesis on mono-and bimetallic Co and Fe catalysts supported on carbon nanotubes. *Fuel Processing Technology.* **2009**, 90, 1486.

14. Okabe, K.; Li, X.; Wei, M.; Arakawa, H. Fischer–Tropsch synthesis over Co–$SiO_2$ catalysts prepared by the sol–gel method. *Catalysis today.* **2004,** 89, 431.

15. Khodakov, A.Y.; Chu, W.; Fongarland, P. Advances in the development of novel cobalt Fischer-Tropsch catalysts for synthesis of long-chain hydrocarbons and clean fuels. *Chemical Reviews.* **2007**, 107, 1692.

16. Kang, S.H.; Bae, J.W.; Woo, K.J.; Sai Prasad, P.S.; Jun, K.W. ZSM-5 supported iron catalysts for Fischer–Tropsch production of light olefin. *Fuel Processing Technology,* **2010**, 91, 399.

# CHAPTER 2

# Literature review

This chapter covers discussion on biofuels, second generation biofuels, lignocellulosic feedstocks as biomass as well as their thermochemical conversion routes for the production of second generation biofuels. Detailed review on Fischer-Tropsch Synthesis which includes brief history, the chemistry, FT catalysts and modes of operation; active sites and reduction of cobalt and iron based FT catalysts, product selectivity and distribution and also performance enhancement and deactivation of cobalt and iron catalysts. Finally the synthesis and characterisation of silica-supported Co, Fe and Ni catalysts were discussed as well.

## 2.1. Biofuels

The global relevance of biofuels as a viable alternative to the use of fossil fuels for the generation of energy is extensively documented in the literature [1-17]. Presently, 80% of the primary energy consumed worldwide is generated from fossil fuels with the transport sector using up 58%. While the sources of these fuels are not infinite, current research has also shown that their burning is a massive contributor to the rising level of atmospheric $CO_2$ which is directly responsible for global warming [2, 15, 16]. The demand for energy consumption is on the increase and the production of energy from fossil fuels is declining at the rate of 4-5% every year while it has been predicted that the world manufacture of oil is expected to peak and obviously plateau in years to come [14, 18].

Biofuels which refer to liquid, solid and gas fuels that are mainly obtained from biomass have favourable features such as degradability, renewability and its quality blends well with exhaust gases. Moreover, they could generate new sources of income as well as employment avenues in remote areas but most importantly, they have the capacity to reduce $CO_2$ emission because the crops used for their production consume $CO_2$ during growth [19]. Between the early eighties of the $20^{th}$ century and 2005, the global production of biofuels increased from 4.4 to 50.1 billion litres with a future increase expected. In 2010 worldwide production of biofuels exceeded 105 billion litres, this increase represents 17% of what was produced in 2009 with 2.7% directed towards transportation fuels [14, 20-22]. The European Union being the third largest producers of biofuels in the world is set to increase its share of production from five percent to ten percent by 2020. Meanwhile, in the "renewable energy directive" (2009/28/EU) a set of criteria have been put in place by the EU to consolidate the consumption and production of biofuels so as to make it a sustainable industry [14, 23]. Baka et al. [24] in an evaluation study, estimated that approximately 26% of fossil fuels currently used in Europe could be replaced by biofuels. Series of studies have also been published by

the European Environment Agency (EEA) stating the EU capacity to produce enough biomass for the generation of biofuels [25].

According to the type of feedstock and route of conversion, biofuels can be broadly classified as first, second, third and fourth generation biofuels [26, 27].

## 2.2. Generations of biofuels

Recent publications generally classify biofuels into first, second, third and fourth generation biofuels [26, 27]. First generation biofuels which consist of bioethanol, biodiesel and biogas are usually produced from sugar containing plants, grains or seeds with a fairly easy route to obtain the finished product of fuels. Today 1$^{st}$ generation biofuels have gone commercial with almost 50 billion litres produced every year, this type of fuel has the capacity to be combusted in existing internal combustion engines, mixed with gasoline based fuels and applied in existing natural gas or alternative technology. High proportion bioethanol blend commonly called E85 (85% ethanol and 15% petrol) is used in flexible fuel vehicles (FFVs) and can be purchased in several petrol stations in the UK [28], but it has been reported by Balat et al. [29] that this bioethanol is hygroscopic making its use quite discouraging as transport fuel. It has been documented that in cold weather fuel filter plugging occurs with biodiesel blends as the presence of wax and water can cause precipitation coupled with the problem of faster solution drop out of glycerin and sterol glycosides particulates [30]. 1$^{st}$ generation biofuels could as well offer some benefits in cutting $CO_2$ emissions and help in supporting energy security on a domestic level [3, 14]. But in spite of some of the promises offered by fuels of this type, there seems to be grievous concerns by scientist which are centred on the argument of food against fuel, attributing hikes in food prices being mainly due to increased manufacturing of these fuels. Rolz et al. [30] studied ethanol production

from sugarcane at different maturity levels and it was discovered that better ethanol yield could only be obtained after 300 – 325 days of planting. Nabi and Co-workers [32] synthesized 77% biodiesel yield with 20% methanol in the presence of 0.5% NaOH from cottonseed oil, they discovered that the biodiesel mixtures contained particulate matters with exhaust smoke and a slight increase in $NO_x$ emission. Recently, Yusuf et al. [33] reported that 95% of 1st generation biodiesel is produced from edible oil which means food resources are being used as transportation fuels. Meanwhile, it has been suggested that biodiesel is not technologically cost efficient in tackling $CO_2$ emission. Hence, it is proposed that a more reliable and sustained alternative which depends on both renewable and conventional technologies be invented for the reduction of greenhouse gases [3, 21].

Second generation biofuels which are produced from non-food produce such as farm residues, wood and waste from organic and food crops have been developed to mitigate the limitations of first generation biofuels [2]. Detailed discussion on this type of biofuel will be presented in subsequent section. Third generation biofuels which are derived from microbes, microalgae and also free from the problems associated with 1st generation biofuels have been recommended as an alternative source to generate energy [14, 27, 34]. Microalgae biofuels made up mainly of bio-methane, bio-oil as well as bio-diesel and bioethanol have the prospect of bringing about diversification of the global sector of renewable energy. Besides, microalgae are a unique feedstock for producing bioethanol. Huang et al. [35] reported the production of microbial oil from sulphuric acid-treated waste rice straw but it was reported that due to the presence of toxicants, the lipid yield from the as treated rice straw was quite poor. Zhu et al. [36] worked on production of microbial biofuel from waste molasses and found out that lipids produced in this microbial biomass can be used for biodiesel production. Widjaja et al. [37] showed that starving algae of a suitable source of nitrogen, produces mainly oil which are useful for conversion to biodiesel. Svetlana et al. [38] emphasized that

biofuels made from algae are the next big thing on the alternative energy agenda but questioned if this group of biofuel can liberate man from the addiction to petroleum. Although, this category of biofuels looks prospective, research has shown that their conversion routes are excessively expensive and challenging and there are very little industries set up to produce biofuel from microalgae [27, 39, 40]. Fourth generation biofuels comprise mainly capturing and storing $CO_2$. This technology makes generated fuels not only carbon neutral but also carbon negative [41, 42], but it has been reported that the route employed in confiscating the $CO_2$ is still very much at its early stage, it is quite cost intensive and its environmental impacts are still uncertain [43-45]. De Coninck et al. [46] reported that even after some successful research and development in this technology, public funds seem to be on the decrease while private stakeholders consider it too expensive and risky to implement in the short run. It was documented by Van Alphen et al [47] that the capture process is one of the most challenging issues regarding this innovation of carbon capture, storage and re-use. Moreover, carbon capture and storage to generate biofuels has not received sufficient commercial scale testing so as to demonstrate how the cost of running it could be lowered. Recently, in one of the report by European Biofuels technology platform [48], it states that the use of carbon capture and storage (CCS) for the production of bio-methane still faces the challenges of seasonal feedstock variability with a relatively small amount of $CO_2$ stream.

## 2.3. Second generation biofuels

Advanced biofuels, also referred to as 2$^{nd}$ generation biofuels, which comprise broadly of lignocellulosic ethanol and FT biodiesel, bio-dimethyl ether (bio-DME) and bio-synthetic natural gas (bio-SNG) have been attracting continued research interest for over three decades

[2, 14]. They are generated through innovative processes using lignocellulosic materials such as grasses, cereal straw, forest residues etc. which consists mainly of affordable and abundant non-edible matters from plants. Second generation biofuels have the capacity to drive down $CO_2$ production, they do not compete with food crops while some of the fuel produced via this technology could offer better engine performance. When advanced biofuel is produced in large scale, it is potentially comparable with standard petrol and diesel and it is obviously a more effective route to generate low carbon and renewable energy to power vehicles. Zabaniotou et al. [49] studied the utilisation of rapeseed residues for the production of $2^{nd}$ generation biofuels. The obtained result showed that high temperature pyrolysis could produce higher yield of syngas compared to air fixed bed gasification. Fast pyrolysis of waste fish oil was performed by Wiggers et al. [50], a bio-oil yield of 73% was obtained and it was also found that this advanced biofuel had similar characteristics to petroleum fuel. Kalbande et al. [51] reported that the biodiesel produced from raw Jatropha was capable of generating power in a 7.5KVA diesel engine generator. Kasakura et al. [52] carried out gasification study of sludge in a pilot plant and obtained gas constituents yield of 5.5 vol% of $H_2$, 3.65 vol% of CO, 1.48 vol% of $CH_4$ as well as other light hydrocarbons in lower concentrations. At the moment, several oil companies such as British Petroleum (BP), Shell, Exxon and Chevron are investing heavily in second generation biofuels and it has been predicted based on current funding that the production of this category of fuels would commercially get to full scale sooner than expected [53]. In a recent publication by Zang [54], it was reported that a biomass to dimethyl ether (DME) plant which utilises wood chips via gasification based in Buluo of China has an annual DME production capacity of 1000 tons with total efficiency of 38%. Bubbling fluidized bed pyrolysis reactor was used by Nowakowski et al. [55] to convert a wheat straw – derived Organosolv lignin in the presence of commercial catalysts and 80% of bio-oil was obtained.

Lignocellulosic materials used for the production of second generation biofuels consist of a variety of feedstocks. Hence, the next section will briefly discuss the composition of these feedstocks as well as their relevance and recent utilisation to manufacture advanced biofuels.

## 2.4. Lignocellulosic biomass as feedstocks for second generation biofuels

Lignocellulosic materials which are the most available renewable resource on the earth have no interference with food, and their use for the production of 2$^{nd}$ generation biofuels has been receiving research attention for more than two decades; as they are relatively not expensive and they have the capacity to reduce $CO_2$ emissions [51, 56-58]. Lignocellulose consists primarily of 25% lignin and 85% of cellulose and hemicellulose. Lignin which binds the plants cells, is an amorphous polymer made up of propane structural units. Cellulose and hemicellulose can be hydrolysed and they form the main sources of sugar fermentation [59]. This feedstock can be categorised into forest residues, agricultural residues and dedicated energy crops. Forest residues such as saw dust, wood chips and logging residues have been reported as feedstocks for the production of second generation biofuels [60, 61]. These feedstocks are flexible to harvest with short periods of storage. Moreover, it has been documented that feedstock from forest residues contains more lignin and less amount of ash than agricultural residues [17]. In a recent study by Franco et al. [62] it was reported that steam explosive treatment of pine wood at 240°C generated almost 11g of cellulosic ethanol using 100g of the dry feedstock which contained 32g of cellulose. Agricultural residues which mostly consist of sugarcane bagasse, corn stover, rice and wheat straws due to their renewable abundance, have been proposed as one of the most promising feedstock for the production of lignocellulosic bio-ethanol [63]. It has also been reported that these types of residues contain more hemicellulose materials than woody feedstocks; this minimises the

problem of deforestation and they are readily available [64-66]. Coffee and rice husks were recently used by Cuthbert [67] to study their performance as feedstocks to generate advanced biofuel, it was found that Coffee husks were more viable than rice husks. Energy crops such as switch grass, poplar and willow have also received a reasonable amount of research attention as feedstocks for 2nd generation biofuels [17, 68-70]. The thermochemical conversion characteristics of straws and switch grass were studied by Greenhalf et al. [71] and it was found that switch grass was a better feedstock with a high volatile yield content of 82.23%, a heating value of 19.64 MJ/Kg as well as relatively low inorganic contents. Bermuda grass is another type of energy crop which has been researched as feedstock for cellulosic ethanol [72]. Anderson et al. [76] used 1.75% (w/v) sulphuric acid to treat Coastal and Tifton Bermuda grass at 121°C for 1hr and found that the acid pretreatment resulted in an ethanol yield of 140mg/g raw biomass.

The conversion of these feedstocks to produce 2nd generation biofuels can generally be achieved through the biochemical process which involves transformation of cellulose and hemicellulose to sugars in the presence of enzymes followed by fermentation to bioethanol while the thermochemical route consists of liquefaction, gasification which entails drying, pyrolysis or devolatilization, reduction and direct combustion. However, most synthetic transportation biofuels are produced through gasification followed by Syngas cleaning and conditioning then through Fischer-Tropsch Synthesis (FTS). Meanwhile, as the aim of this work is based on the Fischer-Tropsch synthesis technology, a great deal of attention will subsequently be given to its review [2].

## 2.5. Thermochemical conversion processes for 2nd generation biofuels

### 2.5.1. Gasification

Gasification entails reacting feedstocks with controlled amount of air, oxygen or steam at high temperature to produce gaseous mixture of CO, $CO_2$, $H_2$, $CH_4$, $C_2H_4$ as well as other impurities such as $N_2$, sulphur, alkali compounds and tars. Gasification reactors are usually operated at temperature as high as 1000°C while their sequence of operation consists of drying, pyrolysis or devolatilization, reduction and combustion. At the point of drying, the feedstock is stripped of its moisture content which is usually high for most lignocellulosic materials while the devolatilization or pyrolysis segment deals with the removal of volatiles in the form of light hydrocarbons, CO, $CO_2$ and the formation of liquid long-chain hydrocarbons known as tar. The nature of the formed tar strongly depends on the type of feedstock as well as the gasifying agent and operating conditions of the reactor [74]. The reduction region acts as the main process where the raw materials are completely gasified in the presence of oxygen or steam to produce syngas through various endothermic reactions. The combustion segment comprises of burning the residual char to generate more gaseous products and the amount of heat required for reactions in the reduction region to proceed. Based on the different kinds of lignocellulosic feedstocks, gasification reactors can be classified as fluidised bed, fixed bed and entrained flow reactors. The fluidised bed gasifier operates by fluidising a bed of granny porous material which offers the advantage of a uniform temperature distribution and better solid gas contact as well as heat transfer rates. In a fixed bed gasifier, gas is passed through the feedstock while the gasifier zones are in fixed position for the reaction to occur. Entrained flow reactors mostly operates at a much higher temperature of over 1500°C and pressure of 80 bar which requires a rather uniform particle size distribution for the feedstock [74, 75].

Wang et al. [76] gasified pine saw dust using a fluidized bed gasifier and obtained an ideal syngas product of 1.4 $H_2$/CO with 15mg/$Nm^3$ of tar. A model fixed bed gasifier was designed by Li et al. [77] where syngas with relatively low tar content was produced. Yan Cao et al. [81] proposed a tar free lab scale fluidised bed gasification process using sawdust under autothermic conditions. It was found that this gasifier had a gas fuel production capacity of 3$Nm^3$/kg lignocellulosic biomass with heating value of 5J/$Nm^3$ while the formation of tar was efficiently controlled below 10mg/$Nm^3$.

### 2.5.2. Synthetic gas cleaning and conditioning

The formation of tar during gasification is usually not desirable as syngas production for use as synthetic fuel is the main focus of the gasification process. Tar is quite viscous and tends to condense at low temperature and could also cause equipment blockage and fouling leading to failure in operation. The reduction of tar can be obtained through optimisation selection of the operating parameters such as the use of catalysts that can inhibit its formation as well as process modification. Cleaning of tar from syngas can be carried out by using cyclones, filters or tar cracking procedures [74, 79]. Cleaning of impurities such as alkali and sulphur from syngas used as liquid biofuels is also a crucial step because these unwanted substances could cause damage to automobiles. Alkali and sulphur compounds are usually removed from these gases using sorbents at temperatures of around 300°C and above.

## 2.6. Fischer-Tropsch Synthesis

### 2.6.1. Brief History

Fischer-Tropsch Synthesis (FTS) is basically a polymerisation reaction whereby hydrogen triggers the formation of carbon bonds from carbon atoms of carbon monoxide in the presence of a metal catalyst. This reaction can lead to a range of products depending on the type of catalyst used and the reaction condition considered [80, 81].

FTS goes back to the start of the $20^{th}$ century. In 1902, Sabatier et al. [82] hydrogenated CO to $CH_4$ over a nickel catalyst and, between 1913 and 1914 Badische et al. [83-85], who were working for BASF at the time, got a patents award for the production of hydrocarbon from syngas over bimetallic osmium and cobalt catalysts at high pressure, these hydrocarbons contained mainly oxygenated synthol. In 1920, Fischer and Tropsch [86] reported the formation of a product over alkalised iron shavings at 400°C using 100 bar, which had similar features to what was previously produced by Badische and Co-worker. Fischer and Tropsch also prepared small quantity of ethane and higher hydrocarbons over $Fe_3O_4$.ZnO catalysts under atmospheric pressure at 370°C. Meanwhile, due to the problem of deactivation associated with iron-based catalyst, the use of cobalt and nickel were proposed. In a period of seven years beginning from 1923, Fischer and Tropsch synthesized hydrocarbons from syngas using Co catalyst and also developed $ThO_2$-Kieselguhr supported Co and Ni catalysts [87, 88]. However, as nickel yields too much unwanted amount of methane, most studies were geared towards cobalt [89].

In 1936, the first commercial cobalt based plant for FTS began in Germany and within a space of two years nine plants which employed the use of cobalt catalyst at medium pressure were in operation with a combined production of about 660 x $10^3$ tons per year. Within this period, research into the use of iron as an FT catalyst resumed because Fischer et al. [80]

discovered that at low pressure between 5 – 30 bar, iron showed improved lifetime and product yield. Pichler et al. [89] in 1938 reported the formation of high boiling waxes over ruthenium based catalyst. Although, the nine plants in Germany ceased operation after World War II, the shortage of petroleum based fuel sustained the need for the FT process. In 1955 an FT coal – to – liquid (CTL) plant, which utilises an iron catalyst named SASOL and based in Sasolburg was built in South Africa. The oil embargo in the mid-70s led to the construction of two more FT plants, all producing a capacity of 6 x $10^6$ tons per year [90]. Modern day FT plants based on gas to liquid (GTL) techniques began in 1993, with Shell wax-cracking plant in Bintulu based in Malaysia using cobalt catalyst generates over 9,000 billion barrels litres per day (bbl/day) and PetroSA in Mossel Bay of South Africa with a production capacity of 25,000 bbl/day using Fe based FT catalyst. The continuous fluctuation in prices of oil generated from fossil fuels and the escalating demand for energy coupled with its detrimental effect to the environment during production, has made FTS highly sort after even at this moment in time [91, 92].

### 2.6.2. Chemistry of Fischer-Tropsch Synthesis

Fischer-Tropsch products consist of complex mixture of oxygenated, linear and branched hydrocarbons but the main products are α – olefins and linear paraffins. These hydrocarbons are catalysed by either one or more of cobalt, nickel, iron and ruthenium. The following set of reactions in Table 2.1 can be used to describe the process of FTS [89]. The proposed catalyst for FTS coupled with the reaction conditions have different capacity to favour certain reaction products, for instance Ni catalyst is more selective towards methane at high temperature above 180°C and pressure of 5 bar using 2:1 $H_2$/CO when compared to Co.

Table 2. 1. Overall reactions of Fischer-Tropsch Synthesis [89].

| | | |
|---|---|---|
| Main reactions | | |
| 1. Paraffins | $(2n + 1)\ H_2 + nCO \rightarrow C_nH_{2n+2} + nH_2O$ | 2.1 |
| 2. Olefins | $2nH_2 + nCO \rightarrow C_nH_{2n} + nH_2O$ | 2.2 |
| 3. Water gas shift (WGS) | $CO + H_2O \leftrightarrow CO_2 + H_2$ | 2.3 |
| Side reactions | | |
| 4. Alcohols | $2nH_2 + nCO \rightarrow CnH_{2n+2}O + (n-1)\ H_2O$ | 2.4 |
| 5. Boudouard reaction | $2CO \rightarrow C + CO_2$ | 2.5 |

Fe and Ru catalysts tend to promote the yield of paraffins and olefins as products. Fe has more selectivity for alcohols and it is renowned for catalysing WGS. Hence, it is usually operated using lower ratio of $H_2$/CO in FTS.

The mechanism of how reactions are carried out by FT based catalyst have been reported in numerous publications [89, 93-98], in general products formation in FTS is a polymerisation reaction which involves reactant adsorption, chain initiation, growth and termination, product desorption, readsorption and further reaction [99].

Fischer and Tropsch as well as Elvins et al. [100, 101] originally proposed the metal carbide mechanism which states that the absorbed CO dissociates to bulk metal carbide as intermediates which then hydrogenates to form hydrocarbon and oxygenate products. But it was soon discovered that this mechanism was inconsistent with thermodynamic data in relation to the reaction temperature employed [102, 103]. In a subsequent work by Kummer

et al. [104], it was shown that the formation of bulk metal carbide as intermediates in FTS was not the case as earlier proposed.

The oxygenate (enol) mechanism which has gained widespread acceptance was later proposed by Eidus et al. [105], it involves the chemisorption of CO which reacts with absorbed hydrogen to form M-CHOH species. This enol group grows by a combination of condensation and water elimination steps via the adjacent groups as shown in Fig. 2.1.

This mechanism was strongly supported by Emmett and Co-workers [104], where it was found that the addition of alkenes or alcohol to synthesis gas served as initiator for chain growth. The last mechanism was proposed by Pichler et al. [106], it involves insertion of CO into metal methylene carbon bond which is hydrogenated to produce alcohol or alkene with the possibility of oxygen being eliminated by the alcohol precursor to form alkene.

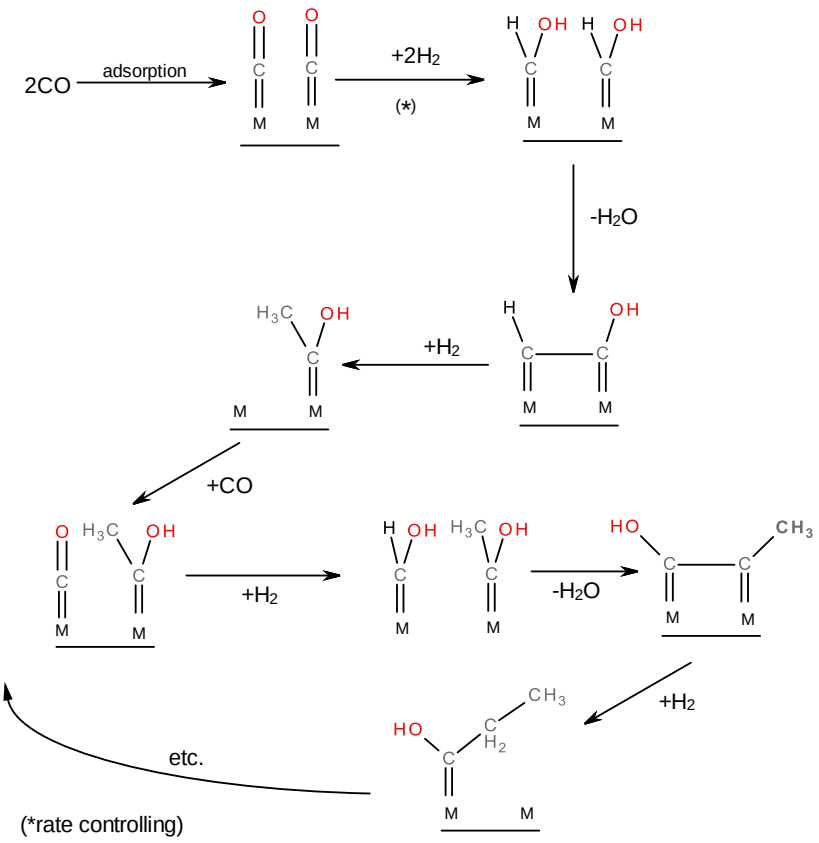


Figure 2.1. Enol condensation and water elimination steps in FTS reaction [107].

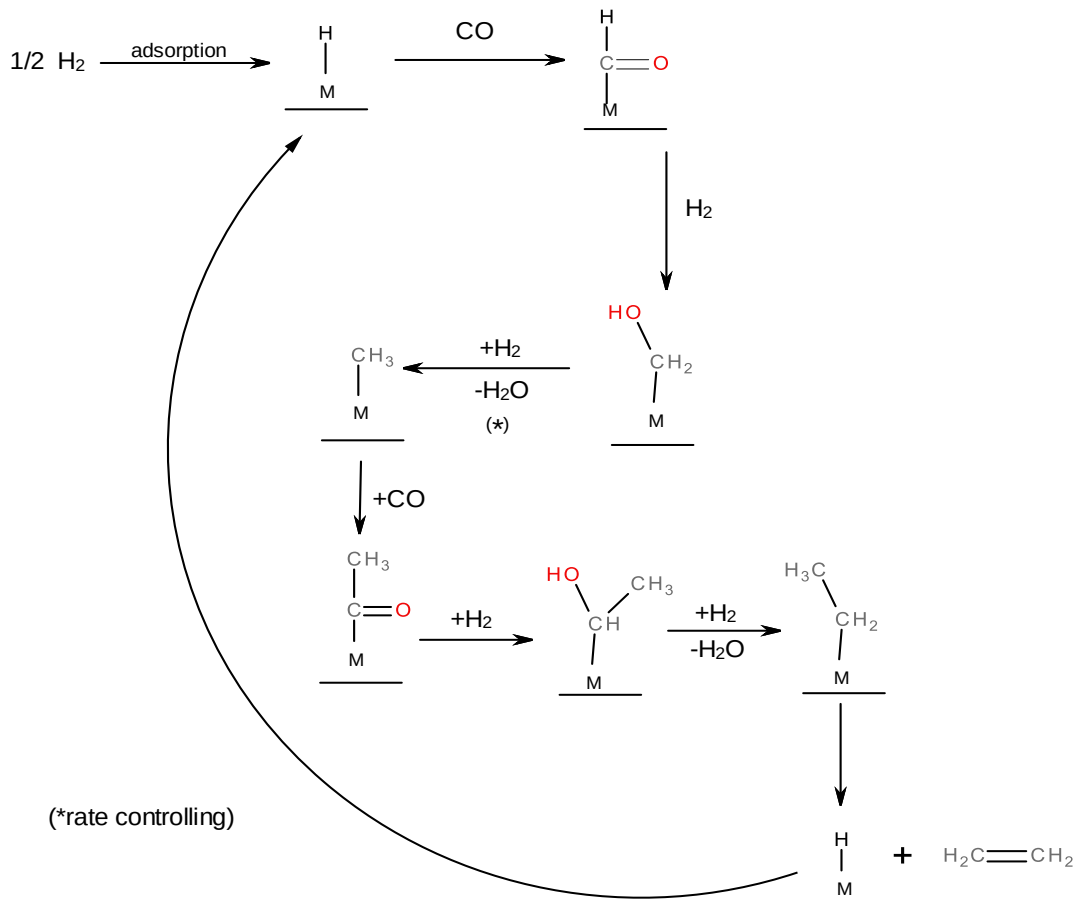


Figure 2.2. CO insertion reaction mechanism for FTS [107].

Figure 2.2 shows one form of the insertion mechanism where hydrogenation and water elimination of the $COH_2^*$ surface species are assumed to be the rate limiting step. Based on this mechanism, it was discovered by the use of surface science techniques that CO adsorbs on single crystal metal surface to produce a surface covered with carbon and few oxygen due to CO chemisorption and dissociation to absorbed C and O which is followed by rapid hydrogenation of O to form $H_2O$ while C hydrogenates to produce $CH_2$ which occurred at a much slower rate [108]. This discovering revived the metal carbide mechanism save that the formed metal carbide is limited to the surface and not bulk formation.

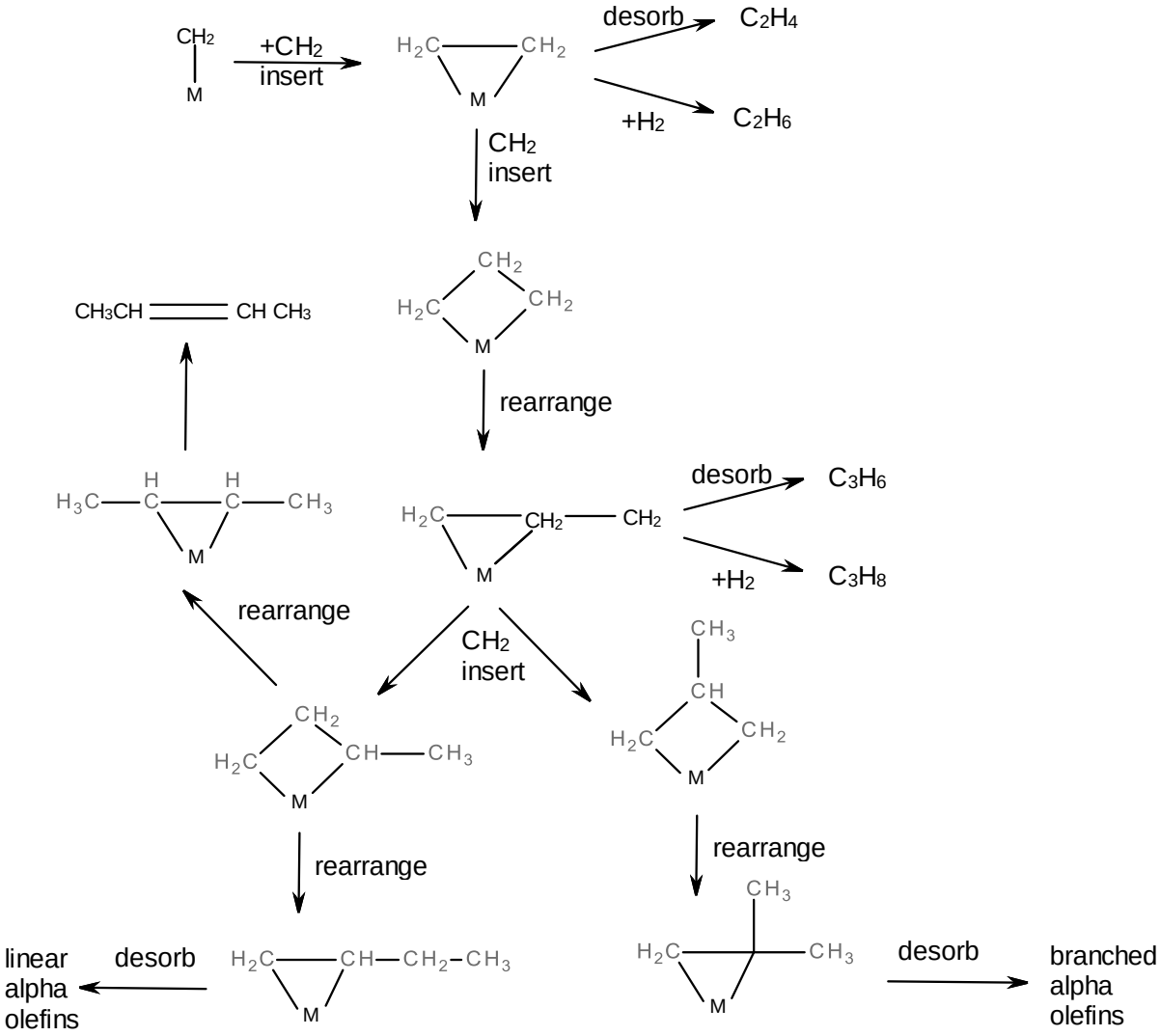


Figure 2.3. Current version of CO insertion reaction mechanism for FTS [107].

Dry [109] went on to elaborate the metal carbide mechanism where the hydrogenated surface carbon was considered to be the rate limiting step while the rest of the reactions are assumed to be at equilibrium. Dry subsequently proposed a current version of the carbide (carbene) theory as shown in Fig. 2.3 which has been adopted and is being currently reported by many [110-116].

2.6.3. Catalysts and modes of operation

All group 8 metals have been reported as active for FTS but only Co, Fe, Ni and Ru are the only metals that have the required FT activity for large scale production [90, 117, 118]. Ni has been reported to produce too much methane while Ru is too expensive and its World availability is not sufficient for commercial application [119, 120]. Therefore, Co and Fe are the most recommended catalysts for FTS. Cobalt catalyst is more expensive than Fe but research shows [12] that cobalt catalyst is more resistant to deactivation and its catalytic activity is more significant at higher conversion, water to gas shift (WGS) reaction is more obvious in Fe than Co catalyst while the amount of water produced in FTS which tends to slow the rate of reaction is more prevalent in iron than cobalt catalyst. Moreover, Fe catalyst is more selective towards olefins. Henrik et al. [121] prepared a series of Co and Fe catalysts and found that the Co-based catalyst was more active for FTS. Mono and bimetallic Co and Fe catalysts were used for FTS by Ahmad et al. [10], and it was reported that the monometallic Fe catalyst had lower FT activity and selectivity towards $C_{5+}$ hydrocarbons compared to Co which had better catalytic performance. While the iron catalyst showed maximum rate for WGS reaction, it was also demonstrated that as the percentage of iron increases in the bimetallic Co-Fe catalysts, the ratio of olefin to paraffins increased. Xiangdong Ma et al. [122] studied what the effect of varying the amount of Fe/CO would have on the catalytic performance of Fe-Co catalysts and found out that higher iron content inhibited catalytic activity while cobalt enhanced the activity.

There are currently two FT operating modes as shown in Fig. 2.4 which are High Temperature Fischer-Tropsch (HTFT) and Low Temperature Fischer-Tropsch (LTFT). Fe catalyst is more suitable for HTFT as Co catalyst results to very high selectivity towards $CH_4$ [95]. Cobalt and iron catalysts can be employed in the LTFT but cobalt is preferred as it possesses high activity and selectivity for heavy waxy products and lower WGS reaction

compared to Fe catalyst [4, 123]. The currently most renowned commercial FT based HTFT plants are run by Sasol in Sasolburg, South Africa while Co based LTFT plant is operated by Shell in Bintulu, Malaysia [92].

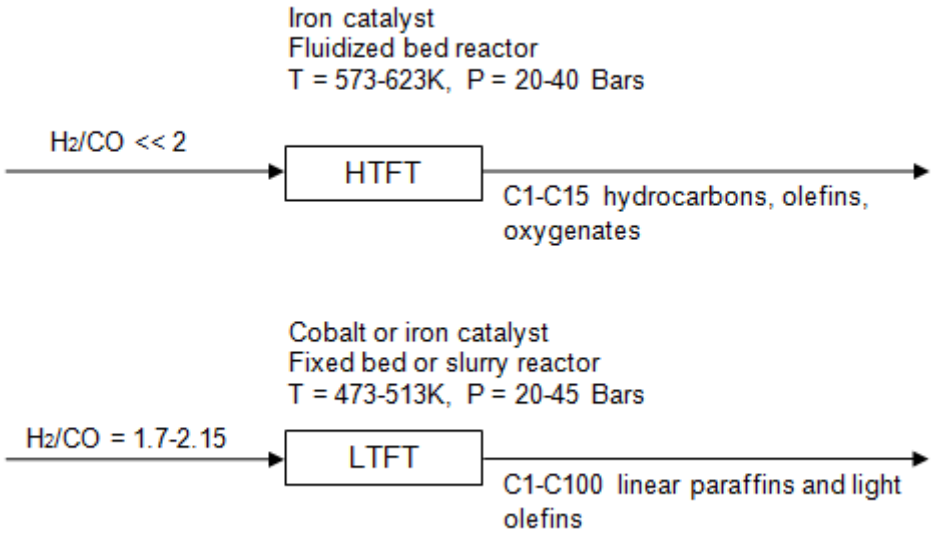


Figure 2.4. High and Low temperature Fischer-Tropsch processes [12].

2.6.4. Active sites and catalyst reduction

The active sites of Co-based FT catalyst consists of metal atoms on the surface of Co metal crystallites. Co catalysts are prepared and usually calcined to form Co-oxides. These oxides of Co are in most cases reduced insitu under flow of $H_2$ at temperature between 473 and 723K prior to FTS experiment [81, 89, 124]. It has been shown that the reduction of cobalt oxide which is usually present as $Co_3O_4$ spinel phase, involves a two-stage successive reduction of $Co_3O_4$ to CoO then to $Co^o$ [10, 125-127]. The active phase of Fe based FT catalyst is not quite defined because of the rapid inter – conversion of Fe carbides, $Fe_3O_4$ and

Fe metal during FTS [81, 128]. Temperature programmed reduction (TPR) was used by Pirola et al. [129] to study the reduction profile of $Fe/SiO_2$ catalyst for FTS. It was found that iron phase reduction transformation involves two stages starting from hematite ($Fe_2O_3$) to magnetite ($Fe_3O_4$) then to (α-Fe) metallic ion. Asami et al. [130] used X-ray diffraction (XRD) to study the deactivation pattern of spent Fe-based FT catalyst. It was discovered that the catalyst deactivation was due to the transformation of metallic iron to Fe carbides during FTS.

### 2.6.5. Product selectivity and distribution

The formation of a wide variety of products with different chain length and function is usually the case in FTS. The exact product distribution always depends on several reaction parameters such as the reactor system used, reactants temperature and partial pressure, product water as well as design and physical properties of the catalyst. Meanwhile, the main products of FTS are n-olefins and n-paraffins while the side products are branched compounds and oxygenates such as 1-alcohols, aldehydes, carboxylic acids and ketones [81].

Although, FT products are of a large range, their distribution tends to show a strong regularity. The products from FTS generally follow the Anderson – Schulz – Flory (ASF) distribution where the molar fraction M of a certain carbon number of n can be described according to equation 2.6

$$M_n = (1-\alpha)\alpha^{n-1} \qquad \text{Eq. 2.6}$$

Hence, product distribution can be determined by the chain growth probability α value [6]. Fig. 2.5 shows the product distribution of FTS as a function of chain growth probability against molar and mass fraction. It predicts that in an ideal ASF distribution, the maximum

selectivity of $C_5 - C_{11}$ gasoline range hydrocarbons is around 45% while those of $C_{12} - C_{20}$ diesel is 30%.

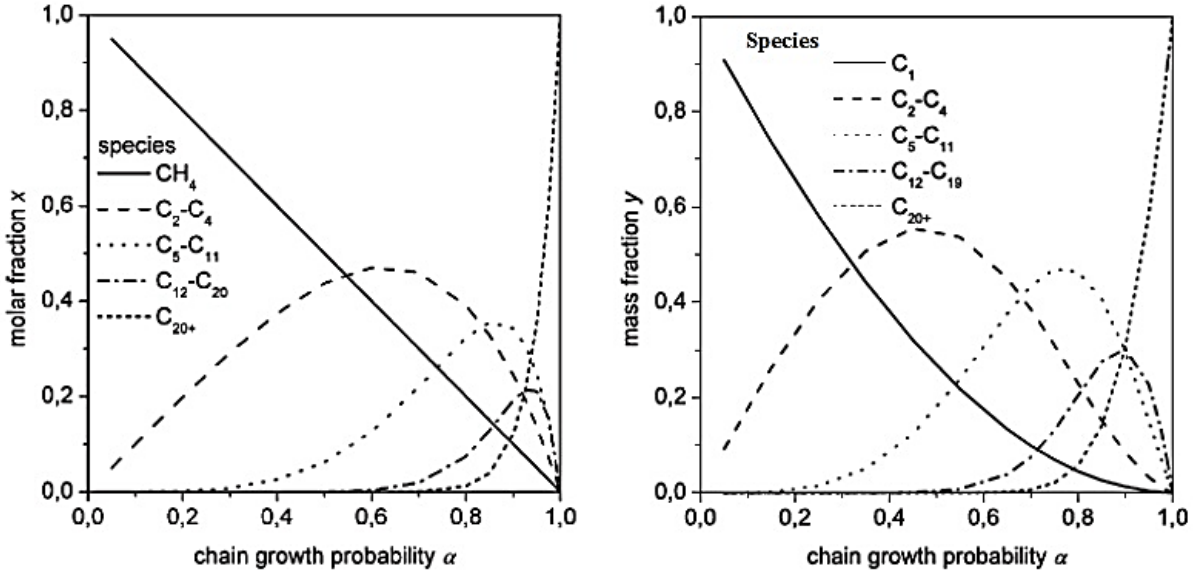


Figure 2.5. FT product distribution as a function of chain growth probability [6].

2.6.6. Enhancement of catalysts performance

The addition of small quantities of promoters during synthesis of FT catalysts tends to enhance an effective reduction of the active phase which is a crucial aspect of optimising the performance of these catalysts. Promoters also help to improve catalyst activity and selectivity by modifying the structural properties and electronic character of the active phase [5]. Moreover, promoters could result to inhibition of FT catalysts deactivation. In most cases metal oxides (MnO and ZnO), certain transition metals (Cu, Pd, Pt, Ru) and alkali metals such as Na, K, Rb and Cs are used as promoters for Co and Fe based FT catalysts. Tsubaki et al.[131, 132] found that the addition of a small amount of Ru to silica-supported cobalt

catalyst significantly enhanced the extent of cobalt reduction. Meanwhile, modification with Pt and Pd did not have any effect on cobalt reducibility but mostly promoted its dispersion. Ru promoted cobalt catalyst showed the highest FT catalytic activity while Pt promoted was the least active catalyst. Moreover, Pt and Pd containing cobalt catalyst had higher methane selectivity than Ru promoted cobalt catalyst [12]. The effect of varying the percentage content of Pd on the catalytic performance of Pd promoted $Co/SiO_2$ catalyst was studied by Osakoo et al.[133], it was discovered that the addition of 0.2wt% Pd enhanced cobalt reducibility, catalytic activity and selectivity towards paraffins but when the amount was increased to 1.0wt%, CO conversion was reduced with increased formation of methane. Yuping et al. [134] studied the outcome of adding between 0.4 – 7.0wt% of Mn on the reducibility and performance of $Co/SiO_2$ catalyst. The results showed that 0.8wt% of Mn increased Co dispersion and weakened Co-Si interaction which resulted to enhanced CO conversion while the addition of 7.0wt% of Mn decreased CO conversion but favoured synthesis of gaseous hydrocarbons. Zhao et al. [135] investigated FTS performance of potassium promoted and un-promoted $Fe/SiO_2$. It was reported that $Fe/K\text{-}SiO_2$ catalyst generated less methane and more $C_{5+}$ products while un-promoted $Fe/SiO_2$ catalyst yielded more methane and less $C_{5+}$ products. Zhang et al. [136] reported that $Fe\text{-}Mn\text{-}K/SiO_2$ catalyst promoted with Cu improved the rate of activation and shortened the reduction period of the catalyst, hydrocarbon selectivity was greatly affected as product distribution shifted to heavy hydrocarbons while the ratio of olefin/paraffin was also enhanced.

### 2.6.7. Catalysts deactivation

Activity and catalyst life time are major concerns in designing catalyst for industrial and economic purposes. Hence, the deactivation mechanism of FT catalysts must be understood

so as to ensure their lifetime can be extended and regeneration of the active phase can be carried out effectively. Some mechanisms such as oxidation, reoxidation, poisoning, sintering, carbon deposition or coking and surface reconstruction have been proposed as causes of Co and Fe catalysts deactivation [5, 6]. Oxidation of metallic Co species could cause deactivation of the catalyst which might reduce rate of reaction during FTS. The formation of cobalt oxide with water as a by-product of FT reaction is also a possible reason for cobalt catalyst deactivation. However, the formation of these oxides can only be due to oxidation of small cobalt crystallites to form oxide shell as bulk formation of cobalt oxide appears not to be thermodynamically feasible [137, 138]. Meanwhile, in recent years research has concluded that the oxidation of bulk or surface metallic cobalt with an average crystallite size of $\geq$ 2nm is not a significant deactivation mechanism of Co based FT catalyst [139, 140]. Deactivation by reoxidation of the active phase of Fe based FT catalyst is mainly caused by high partial pressure of water under LTFT conditions [5, 141]. Studies have shown that metallic iron catalyst formed inactive $Fe_3O_4$ during FTS, while no oxide formation was observed for Co, Ru and Ni catalysts [142-144]. Poisoning refers to strong chemisorption of impurities on the active sites of FT catalysts which retards the catalyst activity. The presence of sulphur acts as poison to FT catalysts [6]. Decrease in CO conversion and formation of $C_{5+}$ hydrocarbons as the amount of sulphur increases has been reported for Co based FT catalyst [145]. Literature has it that sulphur, chlorine, bromine and oxygen are well known poisons for Fe-based FT catalyst with the former having the strongest effect [141, 142, 146]. It has been reported by Baoshan et al. [147] that quantities of sulphur in iron catalyst improved the catalytic activity and selectivity for heavier hydrocarbons while high amounts of sulphide poison the catalyst causing a decrease in CO conversion. Bromfield et al. [146] also revealed that the addition of a small amount of $Na_2S$ in the range of 500 – 5000ppm into a precipitated iron catalyst with a mixture of different iron phases was four times more catalytically active

than a sulphur free Fe catalyst. Sintering is a process by which the growth of small crystallites and loss of support area due to migration phenomena results in reduction to the surface area of catalyst and pore collapse of support [5, 6]. Sintering usually takes place at high reaction temperature and the rate of this process can be increased by the presence of water vapour during FTS. Cobalt crystallite sintering has been identified as the main cause of $Co/SiO_2$ catalyst deactivation [148, 149]. Extended X-ray Absorption Fine Structure (EXAFS) analysis of 20 wt.% of Co-based FT catalyst that had been spent showed a large increase in the degree of Co-Co metal coordination giving rise to substantial growth of Co metal particles relative to a fresh catalyst with uniform particle sizes [150]. Meanwhile, the addition of 0.05wt% of Pt or Ru was found to enhance catalytic activity of supported Co catalyst but led to more deactivation of the catalyst by sintering [151]. Reports have shown that high temperature reaction induced sintering is not the main cause of Fe catalyst deactivation mechanism during FTS [5, 152]. Coking or carbon deposition is the formation of graphitic carbon which deposits on the surface of catalyst during FT reaction while fouling is the deposition of carbon containing materials from feed gas such as tar on catalyst surface all of which results to deactivation [5, 6]. Prolonged period of time on stream could cause cobalt catalyst to form carbides such as $Co_2C$ or $Co_3C$, but the role of carbides in deactivating Co catalyst is small compared to that of Fe as the rate of carbon diffusion into Co to form carbides is negligible. Besides, the probability of cobalt carbide formation is low under typical FTS conditions as all carbon is converted to hydrocarbon products [5]. It has been reported that Co doped with $La_2O_3$ tends to promote formation of Co carbides which leads to the catalyst having very high selectivity towards alcohols [153]. Previous work has shown that catalyst deactivation by carbon deposition could be regenerated by oxidation [139]. In Fe catalyst, coke deposition usually occurs under HTFT conditions (> 280°C) while fouling by amorphous carbon takes place in LTFT at temperature below 280°C. Iron carbide has been

postulated as an active phase for FTS but the inter-conversion of iron carbide species leads to deactivation of the Fe catalyst [143].

Most carbon nanofibre supported cobalt catalysts can be deactivated by surface reconstruction [5]. It has been observed that cobalt surface could experience large scale reconstruction in the presence of synthetic gas [154].

## 2.7. Synthesis and characterisation of silica-supported FT catalyst

The catalytic performance of catalysts used in FTS strongly depends on the method of preparation which involves the choice of catalyst support [12]. To increase activity, obtain higher metal dispersion and to provide high attrition resistance, different oxides with high surface area such as alumina, silica, ceria, zirconia, titania, activated carbon, zeolites have been used as support for Co, Fe and Ni FT catalysts [125, 155-157]. However, in recent years silica has received enormous research attention as support for FT catalyst [122, 126, 158-160].

Venezia et al. [126] studied the modification effect of $TiO_2$ on $Co/SiO_2$ and discovered that the $TiO_2$ modified $Co/SiO_2$ catalyst had lower reducibility due to the strong interaction of CoO with titania which resulted to early deactivation of the catalyst by sintering during FTS. SBA-15 was treated with some amount of titanium and aluminium by M. Lualdi et al. [158] and it was reported that Ti-doped Co/SBA-15 catalyst was 45% lower in space time yield compared to the pure Co/SBA-15 while that of Al modified Co/SBA-15 did not differ significantly in yield from the pure silica-supported cobalt catalyst. Yakubov et al. [159] prepared Co/Multiwalled Carbon Nanutubes (MWCNT) and $Co/SiO_2$ catalysts for FTS. It was found that the catalytic performance of $Co/SiO_2$ was significantly higher than

Co/MWCNT catalyst and the distribution of Co metal on the silica surface was better than that of MWCNT. Xiangdong et al. [122] investigated FT activity of Fe-Co/$SiO_2$, Fe-Co/Activated Carbon and Fe-Co/$Al_2O_3$ bimetallic catalysts. The results showed that the activity of Fe-Co/$SiO_2$ reached maximum while Fe-Co/Activated carbon gave the least activity. The effect of increasing $SiO_2$ content on the catalytic behaviour of Fe/Cu/K/$SiO_2$ catalyst for FTS was studied by Wenjuan et al. [160] and it was observed that the catalyst with more amount of $SiO_2$ had better reaction stability and enhanced selectivity towards light hydrocarbons.

Numerous methods have been reported for the synthesis of silica-supported FT catalysts [12]. But for the sake of this work, silica-supported Co, Fe and Ni based FT catalysts would be the focus of attention. Some of the reported techniques used in preparing these catalysts are impregnation, co-precipitation, solvo-thermal, deposition-precipitation, sol-gel, colloidal, micro-emulsion, solvated metal atom dispersion, chemical vapor deposition, plasma, ion exchange and adsorption methods. However, only the most reported procedures will be discussed in detail.

The impregnation method is the most commonly used route, it involves contacting a dry support with a solution of dissolved salt precursor followed by drying then decomposition of the precursor at elevated temperature, either by thermal oxidation or reduction. It also entails the incipient wetness route whereby a volume of dissolved salt equivalent to the pores volume of the support is contacted with the support and the capillary forces present in the pores gets filled by the solution with no excess moisture left from the solution [12]. Yao et al. [161] used the polyethylene glycol – additive and impregnation methods to prepare Co/ZSM-5 and Co/$SiO_2$ catalysts, it was found that even though PEG-additive procedure showed the capacity to improve CO conversion of Co/ZSM-5 catalyst, Co/$SiO_2$ catalyst had higher turnover frequency (TOF) than Co/ZSM-5 catalyst. Zhang et al. [162] used the incipient

wetness technique to study solvents effects in $Co/SiO_2$ catalyst. It was discovered that silica-supported cobalt catalyst prepared with acetic acid had slightly higher cobalt dispersion but lower TOF compared to the catalyst synthesized with ethanol. A double solvent impregnation method was reported by Chen et al. [127] where it was shown that $Co/SiO_2$ catalyst prepared by this procedure has more CO conversion and $C_{5+}$ selectivity when compared to the catalyst synthesized by wet impregnation method. Surface impregnation combustion was used by L. Shi et al. [163] and it was reported that the prepared $Co/SiO_2$ catalyst was three fold more active than that of the conventional incipient wetness impregnation technique. Zhang et al. [164] prepared a bimodal iron-based FT catalyst using a novel one-step impregnation method, and it was discovered that this catalyst, when compared to the one prepared by the traditional impregnation route, exhibited improved active metal dispersion and quicker diffusion efficiency which led to excellent catalytic performance. Cobalt (ii) nitrate and cobalt (ii) acetate were prepared by Sun et al. [165] using mixed impregnation process and it was shown that the mixed precursors $Co/SiO_2$ catalyst displayed higher activity than the mono counterpart.

The co-precipitation method is the precipitation of metal ion with ions of the support which tends to usually produce an intimate mixture of metal catalyst and the support [12].

The deposition – precipitation method deals with the combination of precipitation with deposition from a liquid medium. This procedure is carried out by exclusively depositing a solvated metal precursor onto the surface of a suspended support by slow and homogenous release of a precipitating agent usually hydroxyl ion so as to avoid nucleation of a solid precursor compound remaining in the bulk solution [12]. The co-precipitation method was used by Azizi et al. [166] to prepare Fe-Ni-Co catalyst and the impact of reduction variables on the catalyst performance was studied. It was reported that the catalyst reduced at 300°C and, compared to the ones that reduced at 450°C, gave higher CO conversion and $CH_4$

selectivity. Tingzhen et al. [167] combined the co-precipitation technique with spray drying procedure to synthesize Fe-Ni bimetallic catalyst where the effect of increasing nickel content during reduction and on the catalytic performance were investigated. It was found that increasing the amount of nickel to iron improves the dispersion of iron-oxides while the rate of reduction was increased and as expected increasing the content of nickel resulted to enhanced methane selectivity but reduced the formation of heavy hydrocarbons. The co-precipitation method was used by Chen et al. [168] to prepare highly loaded 80% by weight of $Co/SiO_2$ catalyst and the effect of surface acid – base properties of the silica support on the catalyst was studied. It was found from Micro-calorimetric adsorption that the surface acidity – basicity of silica had significant effect on the surface properties of $Co/SiO_2$ catalyst which in turn influenced its FTS performance. Bezemer et al. [169] used the homogenous deposition – precipitation route to synthesize low and high pH $Co/SiO_2$ catalyst. It was discovered that the low – pH catalyst had cobalt hydrosilicates formation which resulted in high reduction temperature of 600°C with low cobalt dispersion and FT activity while the high – pH $Co/SiO_2$ catalyst which reduced at lower temperature were highly dispersed and were 2 – 4 times more active. The sol-gel method also called gelation route is a homogenous process which involves repeatable transformation of a solution into hydrated solid hydrogel. The colloidal method deals with wet chemistry technique whereby control of metal particle size, crystallinity, shape and structure via the bottom up approach can be effectively carried out. The adsorption method is a process whereby ionic species from aqueous solutions are electrostatically pulled unto a solid surface by its charged sites. Chemical vapor deposition involves chemical reactions of gaseous reactants on or around the surface of a heated substrate. The plasma technique generally involves generation of ionised gas by electric discharges, glow, microwave or radio frequency [12].

Jae-Sun Jung et al. [155] used the sol-gel method to prepare cobalt based catalyst supported on different mesoporous silica. It was shown that silica hollow sphere (SHS) supported catalyst had better catalytic activity and $C_{5+}$ selectivity and it was proposed here that the activity of the catalyst on the different supports depends on cobalt particle size and structure of the support . The sol-gel technique was employed by Ali et al. [170] to study the effects of FT operating conditions on the performance of 40% Fe/60% Co/15wt.% $SiO_2$/1.5wt.% K catalyst, it was reported that $H_2/CO$ = 2.1 molar ratio at 350°C and 3 bar was the optimum operating conditions and it was also demonstrated that all of the variable operating conditions influenced the structure, morphology and performance of the catalyst. Xie et al. [171] recently synthesized monodispersed colloidal nanoparticles $Co/SiO_2$ catalyst. It was observed that after a period of 240 hours, the catalyst was still quite stable and active with very promising selectivity towards $C_5$ – $C_{18}$ hydrocarbons. Glow discharge plasma – assisted $Co/SiO_2$ catalyst was prepared and studied by Hong et al. [172]. It was found that cobalt dispersion was significantly enhanced by plasma pretreatment and the particle size was directly proportional to the intensity of the glow discharge plasma while the catalytic activity which was quite poor was enhanced by the addition of ruthenium. Fu et al. [173] used the plasma technique to prepare supported cobalt catalyst and reported that this method resulted to Co particles which were highly uniform and well dispersed. Yan et al. [7] proposed a model $Co/SiO_2$ catalyst by vapor – deposition of cobalt from a resistively heated cobalt wire on $SiO_2$ films and it was shown that increasing reaction temperature raised the rate of reaction but shifted catalytic selectivity towards $CH_4$ while the catalyst deactivation was caused by carbon deposition.

Most of these reported approaches seem very promising. However, it cannot be disputed that some of them are extensively time consuming [127, 161-163] while others are still faced with the possible problem of catalyst deactivation via sintering [7, 126, 172].

Hence, we report a novel facile technique called the swelling in method (SIM) for the synthesis of silica-supported Co, Fe and Ni based FT catalysts.

**References**


1. Caspeta, L.; Buijs, N.A.; Nielsen, J. The role of biofuels in the future energy supply. *Energy & Environmental Science*. **2013**, 6, 1077.
2. Damartzis, T.; Zabaniotou, A. Thermochemical conversion of biomass to second generation biofuels through integrated process design—A review. *Renewable and Sustainable Energy Reviews.* **2011,** 15, 366.
3. Naik, S.; Vaibhav, V.G.; Prasant, K.R.; Ajay, K.D. Production of first and second generation biofuels: a comprehensive review. *Renewable and Sustainable Energy Reviews.* **2010**, 14, 578.
4. Schulz, H. Short history and present trends of Fischer–Tropsch synthesis. *Applied Catalysis A: General.* **1999,** 186, 3.
5. Jahangiri, H.; Bennett, J.; Mahjoubi, P.; Wilson, K.; Gu, S. A review of advanced catalyst development for Fischer-Tropsch synthesis of hydrocarbons from biomass derived syn-gas. *Catalysis Science & Technology.* **2014,** 4, 2210.
6. Hu, J.; Yu, F.; Lu, Y. Application of Fischer–Tropsch Synthesis in Biomass to Liquid Conversion. *Catalysts.* **2012,** 2, 303.
7. Yan, Z.; Wang, Z.; Bukur, D.B.; Goodman, D.W. Fischer–Tropsch synthesis on a model $Co/SiO_2$ catalyst. *Journal of Catalysis.* **2009,** 268, 196.
8. Cheng-Hua, Z.; Yong, Y.; Zhi-Chao, T.; Wei-Xiang, H. Structural properties and reduction behavior of Ni promoted $FeMnK/SiO_2$ catalysts for Fischer-Tropsch synthesis. *Journal of Fuel Chemistry and Technology.* **2006,** 34, 695.
9. Surisetty, V.R.; Kozinski, J.; Dalai, A.K. Novel Ni-Co-Mo-K Catalyst Supported on Multiwalled Carbon Nanotubes for Higher Alcohols Synthesis. *Journal of Catalysts.* **2013**, 1, 1.

10. Tavasoli, A.; Trépanier, M.; Malek Abbaslou, R.M.; Dalai, A.K.; Abatzoglou, N. Fischer–Tropsch synthesis on mono-and bimetallic Co and Fe catalysts supported on carbon nanotubes. *Fuel Processing Technology.* **2009**, 90, 1486.

14. Okabe, K.; Li, X.; Wei, M.; Arakawa, H. Fischer–Tropsch synthesis over Co–$SiO_2$ catalysts prepared by the sol–gel method. *Catalysis today.* **2004**, 89, 431.

15. Khodakov, A.Y.; Chu, W.; Fongarland, P. Advances in the development of novel cobalt Fischer-Tropsch catalysts for synthesis of long-chain hydrocarbons and clean fuels. *Chemical Reviews.* **2007**, 107, 1692.

13. Kang, S.H.; Bae, J.W.; Woo, K.J.; Sai Prasad, P.S.; Jun, K.W. ZSM-5 supported iron catalysts for Fischer–Tropsch production of light olefin. *Fuel Processing Technology*. **2010**, 91, 399.

14. Nigam, P.S.; Singh, A. Production of liquid biofuels from renewable resources. *Progress in Energy and Combustion Science*. **2011**, 37, 52.

15. Zhang, L.; Xu, C.C.; Champagne, P. Overview of recent advances in thermo-chemical conversion of biomass. *Energy Conversion and Management*. **2010**, 51, 969.

16. Fernandes, D.L.; Pereira, S. R.; Serafim, L. S.; Evtuguin, D. V.; Xavier, A, M. R. B. Second generation bioethanol from lignocellulosics: processing of hardwood sulphite spent liquor. *INTECH Open Access Publisher*. **2012**, 6, 123.

17. Limayem, A.; Ricke, S.C. Lignocellulosic biomass for bioethanol production: current perspectives, potential issues and future prospects. *Progress in Energy and Combustion Science*. **2012**, 38, 449.

18. Aleklett, K.; Campbell, C.J. The peak and decline of world oil and gas production. *Minerals and Energy-Raw Materials Report*. **2003**, 18, 5.

19. Stevens, C.; Verhe, R. Renewable Bioresources. West Sussex, England: *John Wiley & Sons Ltd*. **2004**.

20. Fulton, L.; Howes, T.; Hardy, J. Biofuels for transport: An international perspective. *GEFSTAP Liquid Biofuels Workshop, August*. **2005**.

21. COUNCIL, P.E.C. The Future Role of Biofuels. *Pacific Food System Outlook*. **2006**.

22. Pickett, J.; Anderson, D.; Bowles, D.; Bridgwater, T.; Jarvis, P.; Mortimer, N.; Polakoff, M.; Woods, J. Sustainable biofuels: prospects and challenges. *The Royal Society, London, UK*. **2008**.

23. Larsen, L.E.; Jepsen, M. R.; Frederiksen, P. Scenarios for biofuel demands, biomass production and land use–The case of Denmark. Biomass and Bioenergy. **2013**, 55, 27.

24. Baka, J.; Roland-Holst, D. Food or fuel? What European farmers can contribute to Europe's transport energy requirements and the Doha Round. *Energy Policy*. **2009**, 37, 2505.

25. Wiesenthal, T.; Mourelatou, A. How much bioenergy can Europe produce without harming the environment? *European Environmental Agency*. **2006**, 7, 10.

26. Dutta, K.; Daverey, A.; Lin, J.-G. Evolution retrospective for alternative fuels: First to fourth generation. *Renewable Energy*. **2014**, 69, 114.

27. Berni, M.D.; Dorileo, I.L.; Prado, J.M.; Foster-Carneiro, T.; Meireles, M.A.A. Advances in Biofuel Production. *John Wiley & Sons, Inc*. **2013**, 11.

28. Luque, R.; Campelo, J.M.; Luna, D.; Marinas, J.M.; Herrero-Davila, L.; Clark, J.H.; Romero, A.A.; Hidalgo, J.M. Biofuels: a technological perspective. *Energy & Environmental Science*. **2008**, 1, 542.

29. Balat, M. Global bio-fuel processing and production trends. *Energy, Exploration & Exploitation*. **2007**, 25, 195.

30. McCormick, R.L.; Alleman, T.; Williams, A.; Coy, Yoshio.; Hudgins, A.; Dafoe, W. Status and Issues for Biodiesel in the United States: A Discussion Paper for Clean

Cities Coalitions and Stakeholders to Develop Strategies for the Future. Draft Report. *National Renewable Energy Laboratory*. **2009**.

31. Rolz, C.; León, R. de. Ethanol fermentation from sugarcane at different maturities. *Industrial Crops and Products*. **2011**, 33, 333.

32. Nabi, M.N.; Rahman, M.M.; Akhter, M. S. Biodiesel from cotton seed oil and its effect on engine performance and exhaust emissions. *Applied Thermal Engineering*. **2009**, 29, 2265.

33. Yusuf, N.; Kamarudin, S.; Yaakub, Z. Overview on the current trends in biodiesel production. *Energy Conversion and Management*. **2011**, 52, 2741.

34. Chen, C.-Y.; Zhao, X.-Q.; Yen, H.-W.; Ho, S.-H.; Cheng, C.-L.; Lee, D.-J.; Bai, F.-W.; Chang, J.-S. Microalgae-based carbohydrates for biofuel production. *Biochemical engineering journal*. **2013**, 78, 1.

35. Huang, C.; Zong, M.-H.; Liu, H.W, Q.-P. Microbial oil production from rice straw hydrolysate by Trichosporon fermentans. *Bioresource Technology*. **2009**, 100, 4535.

36. Zhu, L.Y.; Zong, M.H.; Wu, H. Efficient lipid production with Trichosporon fermentans and its use for biodiesel preparation. *Bioresource Technology*. **2008**, 99, 7881.

37. Widjaja, A.; Chien, C.-C.; Ju, Y.-H. Study of increasing lipid production from fresh water microalgae Chlorella vulgaris. *Journal of the Taiwan Institute of Chemical Engineers*. **2009**, 40, 13.

38. Nikolić, S.; Mojović, L.; Rakin, M.; Pejin, D.; Nedović, V. Effect of different fermentation parameters on bioethanol production from corn meal hydrolyzates by free and immobilized cells of Saccharomyces cerevisiae var. ellipsoideus. *Journal of Chemical Technology & Biotechnology*. **2009**, 84, 497.

39. Jang, Y.-S.; Park, J.M.; Choi, S.; Choi, Y.J.; Seung, D. Y.; Cho, J.H.; Lee, S.Y. Engineering of microorganisms for the production of biofuels and perspectives based on systems metabolic engineering approaches. *Biotechnology Advances*. **2012**, 30**,** 989.

40. Daroch, M.; Geng, S.; Wang, G. Recent advances in liquid biofuel production from algal feedstocks. *Applied Energy*. **2013**, 102, 1371.

41. Gray, D.; White, C.; Tomlinson, G. Increasing security and reducing carbon emissions of the US transportation sector: A transformational role for coal with biomass. *National Energy Technology Laboratory*. **2007**, 1298, 3.

42. Schubert, C. Can biofuels finally take center stage? *Nature biotechnology*. **2006**, 24, 777.

43. Peralta-Yahya, P.P.; Zhang, F.; del Cardayre, S.B.; Keasling, J.D. Microbial engineering for the production of advanced biofuels. *Nature*. **2012**, 488, 320.

44. Anderson, S.; Newell, R. Prospects for carbon capture and storage technologies. *Annu. Rev. Environ. Resources*. **2004**, 29, 109.

45. Haszeldine, R.S. Carbon capture and storage: how green can black be? *Science*. **2009**, 325, 1647.

46. de Coninck, H.; Stephens, J.C.; Metz, B. Global learning on carbon capture and storage: A call for strong international cooperation on CCS demonstration. *Energy Policy*. **2009**, 37, 2161.

47. van Alphen, K.; Hekkert, M. P.; Turkenburg, W. C. Accelerating the deployment of carbon capture and storage technologies by strengthening the innovation system. *International Journal of Greenhouse Gas Control*. **2010**, 4, 396.

48. Gough, C.; Upham, P. Biomass energy with carbon capture and storage (BECCS or Bio-CCS). *Greenhouse Gases: Science and Technology*. **2011**, 1, 324.

49. Zabaniotou, A.; Ioannidou, O.; Skoulou, V. Rapeseed residues utilization for energy and 2nd generation biofuels. *Fuel*. **2008**, 87, 1492.

50. Wiggers, V.R .; Wisniewski Jr, A.; Madureira, L.A.S.; Barros, A.A.C.; Meier, H.F. Biofuels from waste fish oil pyrolysis: Continuous production in a pilot plant. *Fuel*. **2009**, 88, 2135.

51. Kalbande, S.; More, G.; Nadre, R. Biodiesel production from non-edible oils of jatropha and karanj for utilization in electrical generator. *Bioenergy research*. **2008**, 1, 170.

52. Kasakura, T.; Hiraoka, M. Pilot plant study on sewage sludge pyrolysis—I. *Water Research*. **1982**, 16, 1335.

53. Oberling, D.F.; Obermaier, M.; Szklo, A.; Rovere, E, L. Investments of oil majors in liquid biofuels: The role of diversification, integration and technological lock-ins. *Biomass and bioenergy*. **2012**, 46, 270.

54. Zhang, W. Automotive fuels from biomass via gasification. *Fuel Processing Technology*. **2010**, 91, 866.

55. Nowakowski, D.J.; Bridgwater, A.V.; Elliott, D.C.; Meier, D.; de Wild, P. Lignin fast pyrolysis: Results from an international collaboration. *Journal of Analytical and Applied Pyrolysis*. **2010**, 88, 53.

56. Furimsky, E. Hydroprocessing challenges in biofuels production. *Catalysis Today*. **2013**, 217, 13.

57. Sims, R.E.H.; Mabee, W.; Saddler, J.N.; Taylor, M. *From 1st-to 2nd-Generation Biofuel Technologies:* An overview of current industry and RD&D activities. *International Energy Agency*. **2008**, 16.

58. Agbor, V.B.; Cicek, N.; Sparling, R.; Berlin, A.; Levin, D.B. Biomass pretreatment: fundamentals toward application. *Biotechnology advances*. **2011**, 29, 675.

59. Crocker, M. Thermochemical conversion of biomass to liquid fuels and chemicals. *Royal Society of Chemistry*. **2010**, 5, 95.

60. Panwar, N.; Kothari, R.; Tyagi, V. Thermo chemical conversion of biomass–Eco friendly energy routes. *Renewable and Sustainable Energy Reviews*. **2012**, 16, 1801.

61. Perlack, R.D.; Wright, L.L.; Turhollow, A.F.; Graham, R.L.; Stokes, B.J.; Erbach, D.C. Biomass as feedstock for a bioenergy and bioproducts industry: the technical feasibility of a billion-ton annual supply. *DTIC Document*. **2005**.

62. Cotana, F.; Cavalaglio, G.; Gelosia, M.; Nicolini, A.; Coccia, V.; Petrozzi, A. Production of Bioethanol in a Second Generation Prototype from Pine Wood Chips. *Energy Procedia*. **2014**, 45, 42.

63. Balat, M.; Balat, H.; Öz, C. Progress in bioethanol processing. *Progress in energy and combustion science*. **2008**, 34, 551.

64. DEMİRBAŞ, A. Bioethanol from cellulosic materials: a renewable motor fuel from biomass. *Energy sources*. **2005,** 27, 327.

65. Knauf, M.; Moniruzzaman, M. Lignocellulosic biomass processing: A perspective. *International Sugar Journal*. **2004**, 106, 147.

66. Kim, S.; Dale, B.E. Global potential bioethanol production from wasted crops and crop residues. *Biomass and bioenergy*. **2004**, 26, 361.

67. Mhilu, C.F. Analysis of Energy Characteristics of Rice and Coffee Husks Blends. *International Scholarly Research Notices*. **2014**, 196103, 1.

68. Koçar, G.; Civaş, N. An overview of biofuels from energy crops: current status and future prospects. *Renewable and Sustainable Energy Reviews*. **2013**, 28, 900.

69. Gomez, L.D.; Steele-King, C.G.; McQueen-Mason, S.J. Sustainable liquid biofuels from biomass: the writing's on the walls. *New Phytologist*. **2008**, 178, 473.

70. Heaton, E.A.; Flavell, R.B.; Mascia, P.N.; Thomas, S.R.; Dohleman, F.G.; Long, S.P. Herbaceous energy crop development: recent progress and future prospects. *Current opinion in Biotechnology*. **2008**, 19, 202.

71. Greenhalf, C.E.; Nowakowski, D.J.; Bridgwater, A.V.; Titiloye, J.; Yates, N.; Riche, A.; Shield, I. Thermochemical characterisation of straws and high yielding perennial grasses. *Industrial crops and products*. **2012**, 36, 449.

72. Xu, J.; Wang, Z.; Cheng, J.J. Bermuda grass as feedstock for biofuel production: A review. *Bioresource Technology*. **2011**, 102, 7613.

73. Anderson, W.F.; Dien, B.S.; Brandon, S.K.; Peterson, J.D. Assessment of bermudagrass and bunch grasses as feedstock for conversion to ethanol. *Applied Biochem Biotechnology*. **2008**, 145, 13.

74. McKendry, P. Energy production from biomass (part 3): gasification technologies. *Bioresource technology*. **2002**, 83, 55.

75. Collot, A.-G. Matching gasification technologies to coal properties. *International Journal of Coal Geology*. **2006**, 65, 191.

76. Wang, T.; Chang, J.; Cui, X.; Zhang, Q.; Fu, Y. Reforming of raw fuel gas from biomass gasification to syngas over highly stable nickel–magnesium solid solution catalysts. *Fuel processing technology*. **2006**, 87, 421.

77. Li, Y.; Wang, T.; Yin, X.; Wu, C.; Ma, L.; Li, H.; Sun, L. Design and operation of integrated pilot-scale dimethyl ether synthesis system via pyrolysis/gasification of corncob. *Fuel*. **2009**, 88, 2181.

78. Cao, Y.; Wang, Y.; Riley, J.T.; Pan, W-P. A novel biomass air gasification process for producing tar-free higher heating value fuel gas. *Fuel Processing Technology*. **2006**, 87, 343.

79. Han, J.; Kim, H. The reduction and control technology of tar during biomass gasification/pyrolysis: an overview. *Renewable and Sustainable Energy Reviews*. **2008**, 12, 397.

80. Henrici-Olivé, G.; Olivé, S. The Fischer—Tropsch synthesis, in The Metal—Carbon Bond. *John Wiley & Sons, Ltd*. **2010**, 391.

81. Lu, X. Fischer-Tropsch Synthesis: Towards understanding. *PhD Thesis submitted to Faculty of Engineering and Built Environment, University of the Witwatersrand, Johannesburg*. **2011**, 7.

82. Sabatier, P.S. Methanation of CO over nickel catalyst. *J. B. Hebd. Seances Acad. Sci. Paris.* **1902**, 680,134.

83. Badische Anilin, S.F. BASF, *German patent*. **1913**, 293, 787.

84. Badische Anilin, S.F. BASF, German patent. **1914**, 295, 202.

85. Badische Anilin, S.F. BASF, German patent. **1914**, 295, 203.

86. Fischer, F.; Tropsch, H. The preparation of synthetic oil mixtures (synthol) from carbon monoxide and hydrogen. *Brennstoff-Chem*. **1923**, 4, 276.

87. Fischer, F.; Tropsch, H. Process for Production of Paraffin Hydrocarbons from Carbon Monoxide and Hydrogen by Catalytic Paths. *German patent*. **1925**, 484, 337.

88. Fischer, F.T.; Brennstoff, H. *Chem*. **1926**, 7.

89. Anderson, R.B.; Van Norstrand –Reinhold. *New Jersey Catalysis*. **1956**, 4.

90. Dry, M.E. The Sasol Fischer-Tropsch Processes. Applied industrial catalysis. **1983**, 2, 167.

91. Post, M.F.M. Shell International Research. *European Patent*. **1985**, 174.

92. Dry, M.E. The Fischer–Tropsch process: 1950–2000. *Catalysis today*. **2002**, 71, 227.

93. Bartholomew, C.H.; Farrauto, R.J. Fundamentals of industrial catalytic processes. *John Wiley & Sons*. **2011**.

94. Ponec, V. Some aspects of the mechanism of methanation and Fischer-Tropsch synthesis. *Catalysis Reviews Science and Engineering*. **1978**, 18**,** 151.

95. Dry, M. The Fischer-Tropsch Synthesis. *Catalysis science and technology*. **1981**, 1, 159.

96. Bell, A.T. Catalytic synthesis of hydrocarbons over group VIII metals. A discussion of the reaction mechanism. *Catalysis Reviews—Science and Engineering*. **1981**, 23, 203.

97. Hindermann, J.; Hutchings, G.; Kiennemann, A. Mechanistic aspects of the formation of hydrocarbons and alcohols from CO hydrogenation. *Catalysis Reviews—Science and Engineering*. **1993**, 35, 1.

98. Maitlis, P.M.; Quyoum, R.; Long, H.C.; Turner, M.L. Towards a chemical understanding of the Fischer–Tropsch reaction: alkene formation. *Applied Catalysis A: General*. **1999**, 186, 363.

99. Adesina, A.A. Hydrocarbon synthesis via Fischer-Tropsch reaction: travails and triumphs. *Applied Catalysis A: General*. **1996**, 138, 345.

100. Fischer, F.; Tropsch, H. Direct synthesis of petroleum hydrocarbons at ordinary pressure. *Berichte*. **1926**, 59B, 830.

101. Elvins, O.C.; Nash, A.W. The Reduction of Carbon Monoxide. *Nature*. **1926**, 118, 154.

102. Emmett, P.H. Catalytic Processes utilizing CO and $H_2$. *Lecture No.4. Oak Ridge National Laboratory*. **1974**.

103. Browning, L.C.; Emmett, P.H. Equilibrium Measurements in the $Ni_3C$-Ni-$CH_4$-$H_2$ and $Co_2C$-Co-$CH_4$-$H_2$ Systems. *Journal of American Chemical Society*. **1952**, 74. 1680.

104. Kummer, J. T.; Evans, O.; Nash, A. *Journal of American Chemical Society*. *Nature*. **1948** and **1926**, 7, 118.

105. Eidus, Y. Mechanism of the synthesis of hydrocarbons from carbon monoxide and hydrogen. *US Dept. of the Interior, Bureau of Mines*. **1958**, 7821, 13.

106. Pichler, H.; Schulz, H. Recent results in synthesis of hydrocarbons from CO and $H_2$. *Chemie Ingenieur Technik*. **1970**, 42, 1162.

107. Davis, B.H. Fischer–Tropsch synthesis: current mechanism and futuristic needs. *Fuel processing technology*. **2001**, 71, 157.

108. Wender, I.; Friedman, S.; Steiner, W. A.; Anderson, R.B. *Chem. Ind*. **1958**. 1694.

109. Dry, M.E. Practical and theoretical aspects of the catalytic Fischer-Tropsch process. *Applied Catalysis A: General*. **1996**, 138, 319.

110. Van Dijk, H.; Hoebink, J.; Schouten, J. A mechanistic study of the Fischer–Tropsch synthesis using transient isotopic tracing. Part-1: Model identification and discrimination. *Topics in catalysis*. **2003**, 26, 111.

111. Van Dijk, H.; Hoebink, J.; Schouten, J. A mechanistic study of the Fischer–Tropsch synthesis using transient isotopic tracing. Part 2: Model quantification. *Topics in catalysis*. **2003**, 26, 163.

112. Biloen, P.; Helle, J.; Sachtler, W.M. Incorporation of surface carbon into hydrocarbons during Fischer-Tropsch synthesis: mechanistic implications. *Journal of Catalysis*. **1979**, 58, 95.

113. Brady III, R.C.; Pettit, R. Mechanism of the Fischer-Tropsch reaction. The chain propagation step. *Journal of the American Chemical Society*. **1981**, 103, 1287.

114. Iglesia, E.; Reyes, S.C.; Madon, R.J. Transport-enhanced α-olefin readsorption pathways in Ru-catalyzed hydrocarbon synthesis. *Journal of catalysis*. **1991**, 129, 238.

115. Iglesia, E.; Reyes, S.C.; Madon, R.J.; Soled, S.L. Selectivity control and catalyst design in the Fischer-Tropsch synthesis: sites, pellets, and reactors. *Advances in Catalysis*. **1993**, 39, 221.

116. Madon, R.J.; Iglesia, E. The Importance of Olefin Readsorption and $H_2$/CO Reactant Ratio for Hydrocarbon Chain Growth on Ruthenium Catalysts. *Journal of catalysis*. **1993**, 139, 576.

117. Hexana, W.M. A systematic study of the effect of chemical promoters on the precipitated Fe-based Fischer-Tropsch Synthesis catalyst. *PhD Thesis submitted to the Faculty of Science, University of the Witwatersrand*. **2009**.

118. Vannice, M. The catalytic synthesis of hydrocarbons from $H_2$/CO mixtures over the group VIII metals: I. The specific activities and product distributions of supported metals. *Journal of Catalysis*. **1975**, 37, 449.

119. Chai, G.-Y.; Falconer, J.L. Alkali promoters on supported nickel: Effect of support, preparation, and alkali concentration. *Journal of Catalysis*. **1985**, 93, 152.

120. Vannice, M.A. The catalytic synthesis of hydrocarbons from $H_2$/CO mixtures over the Group VIII metals: V. The catalytic behavior of silica-supported metals. *Journal of Catalysis*. **1977**, 50, 228.

121. Romar, H.; Lahti, R.; Tynjälä, P.; Lassi, U. Co and Fe catalysed Fischer–Tropsch synthesis in biofuel production. *Topics in Catalysis*. **2011**, 54, 1302.

122. Ma, X.; Fang, D.; Ying, W.; Sun, Q. Effects of the ratio of Fe to Co over Fe-Co/$SiO_2$ bimetallic catalysts on their catalytic performance for Fischer-Tropsch synthesis. *Journal of Natural Gas Chemistry*. **2009**, 18, 232.

123. Janardanarao, M. Direct catalytic conversion of synthesis gas to lower olefins. *Industrial & engineering chemistry research*. **1990**, 29, 1735.

124. Johnson, B.G.; Bartholomew, C.H.; Goodman, D.W. The role of surface structure and dispersion in CO hydrogenation on cobalt. *Journal of Catalysis*. **1991**, 128, 231.

125. Li, J.; Coville, N.J. The effect of boron on the catalyst reducibility and activity of $Co/TiO_2$ Fischer–Tropsch catalysts. *Applied Catalysis A: General*. **1999**, 181, 201.

126. Venezia, A.M.; La Parola, V.; Liotta, L.; Pantaleo, G.; Lauldi, M.; Boutonnet, M. $Co/SiO_2$ catalysts for Fischer–Tropsch synthesis; effect of Co loading and support modification by $TiO_2$. *Catalysis Today*. **2012**, 197, 18.

127. Chen, S.; Li, J.; Zhang, Y.; Zhang, D.; Zhu, J. Effect of preparation method on halloysite supported cobalt catalysts for Fischer-Tropsch synthesis. *Journal of Natural Gas Chemistry*. **2012**, 21, 426.

128. Li, S.; Ding, W.; Meitzner, G.D.; Iglesia, E. Spectroscopic and transient kinetic studies of site requirements in iron-catalyzed Fischer-Tropsch synthesis. *The Journal of Physical Chemistry B*. **2002**, 106, 85.

129. Pirola, C.; Bianchi, C.L.; Di Michele, A.; Diodati, P.; Boffito, D.; Ragaini, V. Ultrasound and microwave assisted synthesis of high loading Fe-supported Fischer–Tropsch catalysts. *Ultrasonics Sonochemistry*. **2010**, 17, 610.

130. Asami, K.; Iwasa, A.; Igarashi, N.; Takemiya, S.; Yamamoto, K.; Fujimoto, K. Fischer–Tropsch synthesis over precipitated iron catalysts supported on carbon. *Catalysis Today*. **2013**, 215, 80.

131. Tsubaki, N.; Sun, S.; Fujimoto, K. Different functions of the noble metals added to cobalt catalysts for Fischer–Tropsch synthesis. *Journal of Catalysis*. **2001**, 199, 236.

132. Qiu, X.; Tsubaki, N.; Sun, S.; Fujimoto, K. Influence of noble metals on the performance of $Co/SiO_2$ catalyst for 1-hexene hydroformylation. *Fuel*. **2002**, 81, 1625.

133. Osakoo, N.; Henkel, R.; Loiha, S.; Roessner, F.; Wittayakun, J. Palladium-promoted cobalt catalysts supported on silica prepared by impregnation and reverse micelle for Fischer–Tropsch synthesis. *Applied Catalysis A: General*. **2013**, 464, 269.

134. Li, Y.; Qin, X.; Wang, T.; Ma, L.; Chen, L.; Tsubaki, N. Fischer-Tropsch synthesis from $H_2$-deficient biosyngas over Mn added $Co/SiO_2$ catalysts. *Fuel*. **2014**, 136, 130.

135. Zhao, G.; Zhang, C.; Qin, S.; Xiang, H.; Li, Y. Effect of interaction between potassium and structural promoters on Fischer–Tropsch performance in iron-based catalysts. *Journal of Molecular Catalysis A: Chemical*. **2008**, 286, 137.

136. Zhang, C.-H.; Yang, Y.; Teng, B.-T.; Li, T-Z.; Zheng, H.-Y.; Xiang, H.-W.; Li, Y.-W. Study of an iron-manganese Fischer–Tropsch synthesis catalyst promoted with copper. *Journal of Catalysis*. **2006**, 237, 405.

137. Van de Loosdrecht, J.; Balzhinimaev, B.; Dalmon, J.-A.; Niemantsverdriet, J.W.; Tsybulya, S.V.; Saib, A.M.; van Berge, P.J.; Visagie, J.L. Cobalt Fischer-Tropsch synthesis: deactivation by oxidation? *Catalysis today*. **2007**, 123, 293.

138. van Steen, E.; Claeys, M.; Dry, M.E.; van de Loosdrecht, J.; Viljoen, E. L.; Visagie, J. L. Stability of nanocrystals: thermodynamic analysis of oxidation and re-reduction of cobalt in water/hydrogen mixtures. *The Journal of Physical Chemistry B*. **2005**, 109, 3575.

139. Saib, A.M.; Moodley, D.J.; Ciobîcã, I.M.; Hauman, M.M.; Sigwebela, B.H.; Weststrate, C.J.; Niemantsverdriet, J.W.; van de Loosdrecht, J. Fundamental understanding of deactivation and regeneration of cobalt Fischer–Tropsch synthesis catalysts. *Catalysis Today*. **2010**, 154, 271.

140. Moodley, D.J.; Saib, A.M.; van de Loosdrecht, J.; Welker-Nieuwoudt, C.; Sigwebela, B.H.; Niemantsverdriet, J.W. The impact of cobalt aluminate formation on the

deactivation of cobalt-based Fischer–Tropsch synthesis catalysts. *Catalysis Today*. **2011**, 171, 192.

141. Espinoza, R.L.; Steynberg, A.P.; Jager, B.; Vosloo, A.C. Low temperature Fischer–Tropsch synthesis from a Sasol perspective. *Applied Catalysis A: General*. **1999**, 186, 13.

142. de Smit, E.; Weckhuysen, B.M. The renaissance of iron-based Fischer–Tropsch synthesis: on the multifaceted catalyst deactivation behaviour. *Chemical Society Reviews*. **2008**, 37, 2758.

143. Eliason, S.; Bartholomew, C. Reaction and deactivation kinetics for Fischer–Tropsch synthesis on unpromoted and potassium-promoted iron catalysts. *Applied Catalysis A: General*. **1999**, 186, 229.

144. Li, S.; O'Brien, R.J.; Meitzner, G.D.; Hamdeh, H.; Davis, B.H.; Iglesia, E. Structural analysis of unpromoted Fe-based Fischer–Tropsch catalysts using X-ray absorption spectroscopy. *Applied Catalysis A: General*. **2001**, 219, 215.

145. Visconti, C.G.; Lietti, L.; Tronconi, E.; Forzatti, P.; Zennaro, R.; Rossini, S. Detailed kinetics of the Fischer–Tropsch synthesis over Co-based catalysts containing sulphur. *Catalysis Today*. **2010**, 154, 202.

146. Bromfield, T.C.; Coville, N.J. The effect of sulfide ions on a precipitated iron Fischer–Tropsch catalyst. *Applied Catalysis A: General*. **1999**, 186, 297.

147. Wu, B.; Bai, L.; Xiang, H.; Li, Y.-W.; Zhang, Z.; Zhong, B. An active iron catalyst containing sulfur for Fischer–Tropsch synthesis. *Fuel*. **2004**, 83, 205.

148. Kiss, G.; Kliewer, C.E.; DeMartin, G.J.; Culross, C.C.; Baumgartner, J.E. Hydrothermal deactivation of silica-supported cobalt catalysts in Fischer–Tropsch synthesis. *Journal of Catalysis*. **2003**, 217, 127.

149. Huber, G.W.; Clint, G.G.; Conrad, T.L.; Stephenson, B, C.; Bartholomew, C.H. Hydrothermal stability of $Co/SiO_2$ fischer-tropsch synthesis catalysts. *Studies in surface science and catalysis*. **2001**, 139, 423.

150. Jacobs, G.; Patterson, P.M.; Zhang, Y.; Das, T.K.; Li, J.; Davis, B.H. Fischer–Tropsch synthesis: deactivation of noble metal-promoted $Co/Al_2O_3$ catalysts. *Applied Catalysis A: General*. **2002**, 233, 215.

151. Jacobs, G.; Patterson, P.M.; Zhang, Y.; Das, T.K.; Li, J.; Sanchez, L.; Davis, B.H. Fischer–Tropsch synthesis XAFS: XAFS studies of the effect of water on a Pt-promoted $Co/Al_2O_3$ catalyst. *Applied Catalysis A: General*. **2003**, 247, 335.

152. Duvenhage, D.J.; Coville, N.J. Deactivation of a precipitated iron Fischer–Tropsch catalyst—a pilot plant study. *Applied Catalysis A: General*. **2006**, 298, 211.

153. Jiao, G.; Ding, Y.; Zhu, H.; Li, X.; Li, J.; Lin, R.; Wenda, D.; Gong, L.; Pei, Y.; Lu, Y. Effect of $La_2O_3$ doping on syntheses of $C_1$–$C_{18}$ mixed linear α-alcohols from syngas over the Co/AC catalysts. *Applied Catalysis A: General*. **2009**, 364, 137.

154. Wilson, J.; de Groot, C. Atomic-scale restructuring in high-pressure catalysis. *The Journal of Physical Chemistry*. **1995**, 99, 7860.

155. Jung, J.-S.; Kim, S.W.; Moon, D.J. Fischer–Tropsch Synthesis over cobalt based catalyst supported on different mesoporous silica. *Catalysis Today*. **2012**, 185, 168.

156. Khodakov, A.Y.; Griboval-Constant, A.; Bechara, R.; Villain, F. Pore-size control of cobalt dispersion and reducibility in mesoporous silicas. *The Journal of Physical Chemistry B*. **2001**, 105, 9805.

157. Jothimurugesan, K.; Gangwal, S. Titania-supported bimetallic catalysts combined with HZSM-5 for Fischer-Tropsch synthesis. *Industrial & engineering chemistry research*. **1998**, 37, 1181.

158. Lualdi, M.; Di Carlo, G.; Lögdberg, S.; Järås, S.; Boutonnet, M.; La Parola, V.; Liotta, L.F.; Ingo, G.M.; Venezia, A.M. Effect of Ti and Al addition via direct synthesis to SBA-15 as support for cobalt based Fischer-Tropsch catalysts. *Applied Catalysis A: General*. **2012**, 443, 76.

159. Yakubov, A.; Shahrun, M.S.; Perak, T.; Kutty, M.G.; Hamid, S.B.A.; Piven, V. Comparison of Cobalt based catalysts supported on MWCNT and SBA-15 supporters for Fischer-Tropsch Synthesis by using autoclave type reactor. *Advanced Materials Research*. **2012**, 364, 70.

160. Hou, W.; Wu, B.; Yang, Y.; Hao, Q.; Tian, L.; Xiang, H.; Li, Y. Effect of $SiO_2$ content on iron-based catalysts for slurry Fischer–Tropsch synthesis. *Fuel Processing Technology*. **2008**, 89, 284.

161. Yao, M.; Yao, N.; Shao, Y.; Han, Q.; Ma, C.; Yuan, C.; Li, C.; Li, X. New insight into the activity of ZSM-5 supported Co and CoRu bifunctional Fischer–Tropsch synthesis catalyst. *Chemical Engineering Journal*. **2014**, 239, 408.

162. Zhang, Y.; Liu, Y.; Yang, G.; Endo, Y.; Tsubaki, N. The solvent effects during preparation of Fischer–Tropsch synthesis catalysts: Improvement of reducibility, dispersion of supported cobalt and stability of catalyst. *Catalysis Today*. **2009**, 142, 85.

163. Shi, L.; Jin, Y.; Xing, C.; Zeng, C.; Kawabata, K.; Imai, K.; Matsuda, K.; Tan, Y.; Tsubaki, N. Studies on surface impregnation combustion method to prepare supported $Co/SiO_2$ catalysts and its application for Fischer–Tropsch synthesis. *Applied Catalysis A: General*. **2012**, 435, 217.

164. Zhang, Y.; Bao, J.; Nagamori, S.; Tsubaki, N. A new and direct preparation method of iron-based bimodal catalyst and its application in Fischer–Tropsch synthesis. *Applied Catalysis A: General*. **2009**, 352, 277.

165. Sun, S.; Tsubaki, N.; Fujimoto, K. The reaction performances and characterization of Fischer–Tropsch synthesis $Co/SiO_2$ catalysts prepared from mixed cobalt salts. *Applied Catalysis A: General*. **2000**, 202, 121.

166. Azizi, H.R.; Mirzaei, A.K.; Kaykhaii, M.; Mansouri, M. Fischer–Tropsch synthesis: Studies effect of reduction variables on the performance of Fe–Ni–Co catalyst. *Journal of Natural Gas Science and Engineering*. **2014**, 18, 484.

167. Li, T.; Wang, H.; Yang, Y.; Xiang, H.; Li, Y. Study on an iron–nickel bimetallic Fischer–Tropsch synthesis catalyst. *Fuel Processing Technology*. **2014**, 118, 117.

168. Chen, L.; Tian, X.; Fu, Y.; Shen, J. The effect of surface acidic and basic properties of highly loaded Co catalysts on the Fischer–Tropsch synthesis. *Catalysis Communications*. **2012**, 28, 155.

169. Bezemer, G.L.; Radstake, P.B.; Koot, V.; van Dillen, A.J.; Geus, J.W.; de Jong, K.P. Preparation of Fischer–Tropsch cobalt catalysts supported on carbon nanofibers and silica using homogeneous deposition-precipitation. *Journal of Catalysis*. **2006**, 237, 291.

170. Mirzaei, A.A.; Galavy, M.; Youssefi, A. A silica-supportedFe–Co bimetallic catalyst prepared by the sol/gel technique: Operating conditions, catalytic properties and characterization. *Fuel Processing Technology*. **2010**, 91, 335.

171. Xie, R.; Wang, C.; Xia, L.; Wang, H.; Zhao, T.; Sun, Y. Controlled Preparation of $Co_3O_4$@ porous-$SiO_2$ Nanocomposites for Fischer–Tropsch Synthesis. *Catalysis Letters*. **2014**, 144, 516.

172. Hong, J.; Chu, W.; Chernavskii, P.A.; Khodakov, A.Y. Cobalt species and cobalt-support interaction in glow discharge plasma-assisted Fischer–Tropsch catalysts. *Journal of Catalysis*. **2010**, 273, 9.

173. Fu, T.; Huang, C.; Lv, J.; Li, Z. Fuel production through Fischer–Tropsch synthesis on carbon nanotubes supported Co catalyst prepared by plasma. *Fuel*. **2014**, 121, 225.

# CHAPTER 3

# Techniques and Experimental

This chapter discusses background theory of the analytical techniques used in this thesis. The experimental as well as practical applications of the discussed techniques were also covered.

## 3.1. Background Theory

The materials investigated in this thesis were characterised using a variety of analytical techniques. Thermogravimetry (TG) was used to study thermal degradations. Chemical information was obtained with Fourier Transform Infrared – Attenuated Total Reflectance (FTIR-ATR) Spectroscopy. Powder X-ray diffraction (p-XRD) was employed to examine structural properties of powdered silica and catalyst. Nitrogen adsorption was carried out to measure surface area and pore size distribution while Mass Spectrometry (MS) was used for catalytic activity testing.

### 3.1.1. Thermogravimetry (TG)

TG is an analytical technique used to quantitatively determine the decomposition and thermal stability of a material and its portion of volatile constituents by measuring its change in mass as a function of increase in temperature or time in the presence of air or inert atmosphere [1]. The change in mass of a material strongly depends on the experimental parameters such as the type of atmosphere, the form and mass of sample, rate of scanning as well as the nature and shape of the sample holder. To slow down the rate of oxidation, the experiment can be carried out under lean amount of oxygen in $N_2$ or Helium. Curves in TG are normally plotted with change in mass ($\Delta m$) expressed in percentage on the primary vertical axis while the corresponding $1^{st}$ derivative of the TG which is referred to as Differential Thermogravimetry (DTG) curve is expressed in (% °C), and is usually plotted on the secondary vertical axis with both plots (TG and DTG plots) against temperature (T) or time (t) on the horizontal axis. Figure 3.1 is a typical TG/DTG curve of the oxidative thermal degradation of polydimethylsiloxane (PDMS) to synthesize fumed silica as support for catalysts studied in this thesis. The DTG curve gives detailed decomposition information such as the different

temperatures at which each reaction steps initiates or terminates and depending on the rate of heating, it can also be used to identify the exact number of degradation steps a material undergoes. [2].

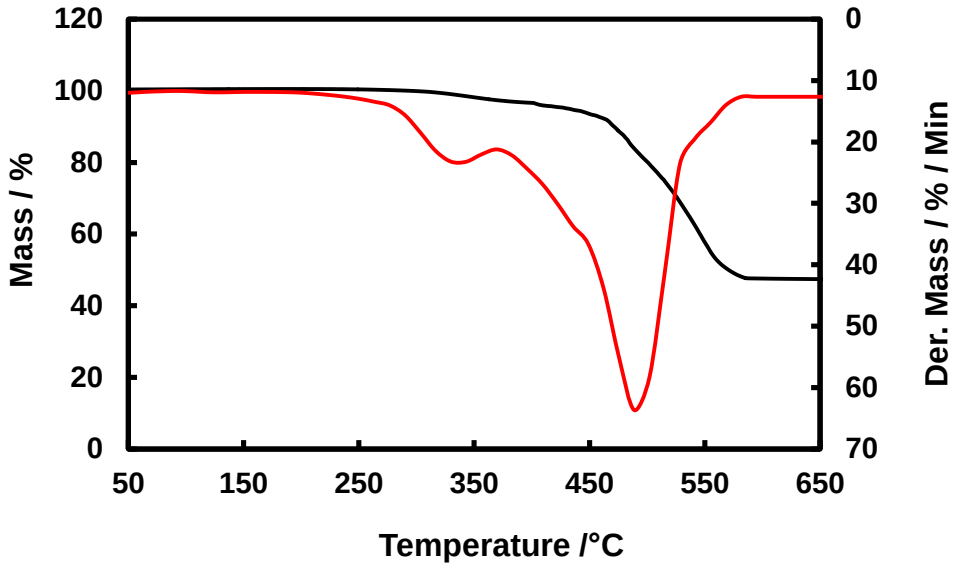


Figure 3. 1. TG/DTG mass loss curve of PDMS to $SiO_2$ heated in air at 5°C $min^{-1}$ to 650°C

3.1.2. Fourier Transform Infrared – Attenuated Total Reflectance (FTIR-ATR) Spectroscopy

FTIR-ATR Spectroscopy was used in this thesis to qualitatively study the spectroscopic behaviour of the chemical constituents of the prepared catalysts. It is a surface sensitive technique which causes the interaction of electromagnetic radiation with solids, liquids or gaseous molecules within 4000 – 400$cm^{-1}$ region of the electromagnetic spectrum. Infrared spectra can be reported as wavelength (μ) but wavenumber ($cm^{-1}$) is usually preferred because the energy of light varies directly with wavenumber [3, 4]. The spectrum generated by this procedure is made possible by the help of a mathematical algorithm called Fourier Transform. The process of interaction excites the molecules making its covalent bonds to vibrate by stretching or bending [3].

The basic principle of operation in a typical FTIR-ATR technique is described according to Fig. 3.2 and equation 3.1.

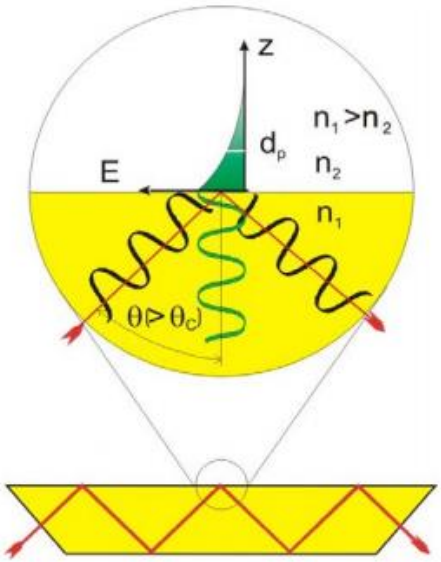


Figure 3.2. Schematic of (IR-ATR) Infrared – Attenuated Total Reflection Spectroscopy [4]

$$n_1 \, \mathrm{Sin}\theta_1 = n_2 \, \mathrm{Sin}\theta_2 \qquad \text{Eq. 3.1}$$

Where $n_1$ is the refractive index of the crystal, $n_2$ is the refractive index of the sample; $\theta_1$ is the angle of incident light while $\theta_2$ is the refracted angle. Here, an infrared light at a certain angle of incidence is directed through a sample that is placed in close contact with a crystal (for example, ZnSe) which has a relatively high refractive index, this light then reflects from the internal surface of the crystal and penetrates into a less dense medium (which is the sample) with small refractive index to form a process called total internal reflection (TIR), which suggest that the angle of incidence exceeds the critical angle. This process eventually generates an evanescent wave which produces some energy that gets absorbed by the sample

and reflected beam which then attenuates and goes to the detector as interferograms and converts to infrared spectrum by the Fourier Transform [5].

### 3.1.3. Powder X-ray diffraction (p-XRD)

This analytical technique uses X-rays to determine the crystal structure, sizes and chemical composition of materials that are usually crystalline in nature [6]. Here, a beam of monochromatic (same wavelength) X-rays hit a single crystal which get diffracted in a particular direction (in phase with one another) known as constructive interference so as to satisfy Bragg's condition as shown in Figure 3.3 and equation 3.2.

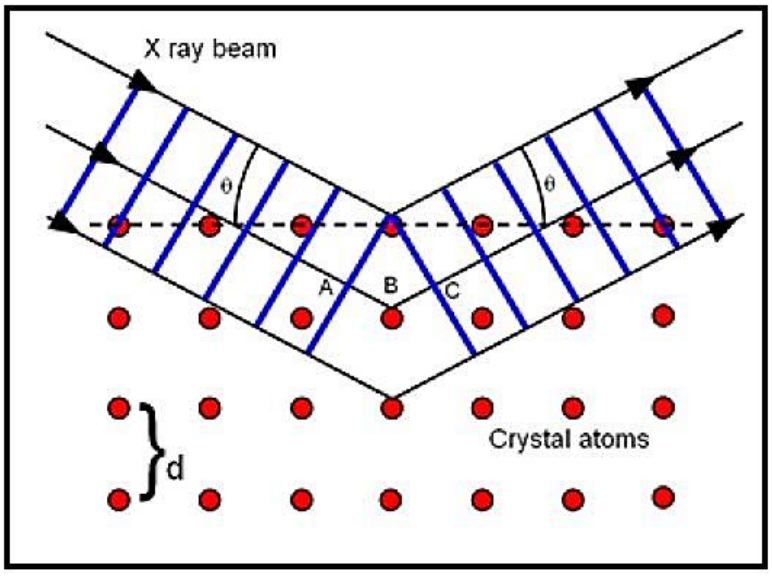


Figure 3. 3. Lattice planes of powder X-ray [7].

$$n\lambda = 2d_{hkl} \sin\theta \qquad \text{Eq. 3.2}$$

Where (d) is the spacing between the crystal planes ($d_{hkl}$), θ is the angle between incident and reflected beams from the planes and n is an integral number which is the order of reflection while λ is the wavelength of the X-rays. Diffraction from a crystalline substance is usually

made possible by the presence of many sets of atomic planes and each set of planes is defined by Miller indices h, k and l which explain how planes intersect three axes x, y and z in relation to the dimensions of the crystal unit cell.

The Scherrer equation as shown in equation 3.3 can sometimes be used to evaluate particle sizes of crystallites especially when the sizes are in the range of 6 – 25nm but when the crystallites are very small or large, the accuracy becomes significantly reduced [8, 9].

$$d = \frac{K\lambda}{B\,Cos\theta} \qquad \text{Eq. 3.3}$$

Where d is the average crystallite diameter, λ is the wavelength, K is a constant which is normally equal to one, B is the full width at half maximum (FWHM) of the peak in degree while θ is the Bragg's angle.

### 3.1.4. Nitrogen Adsorption

The adsorption of an inert gas onto the surface of a solid material via physisorption can be used to calculate the surface area of the solid. In most cases nitrogen is used as adsorbate for adsorbents with large surface area where an absorption isotherm is produced by measuring the quantity of nitrogen absorbed by the solid against the pressure of nitrogen in equilibrium with the solid. This pressure is traditionally expressed as $P/P_o$ where P is the gas pressure and $P_o$ is the saturated vapour of the test temperature. Nitrogen adsorption isotherms are usually collected at 77K, saturated vapour pressure ($P_o$) and 1bar. The values of $P/P_o$ are usually reported in the range of 0 to 1.0 [11].

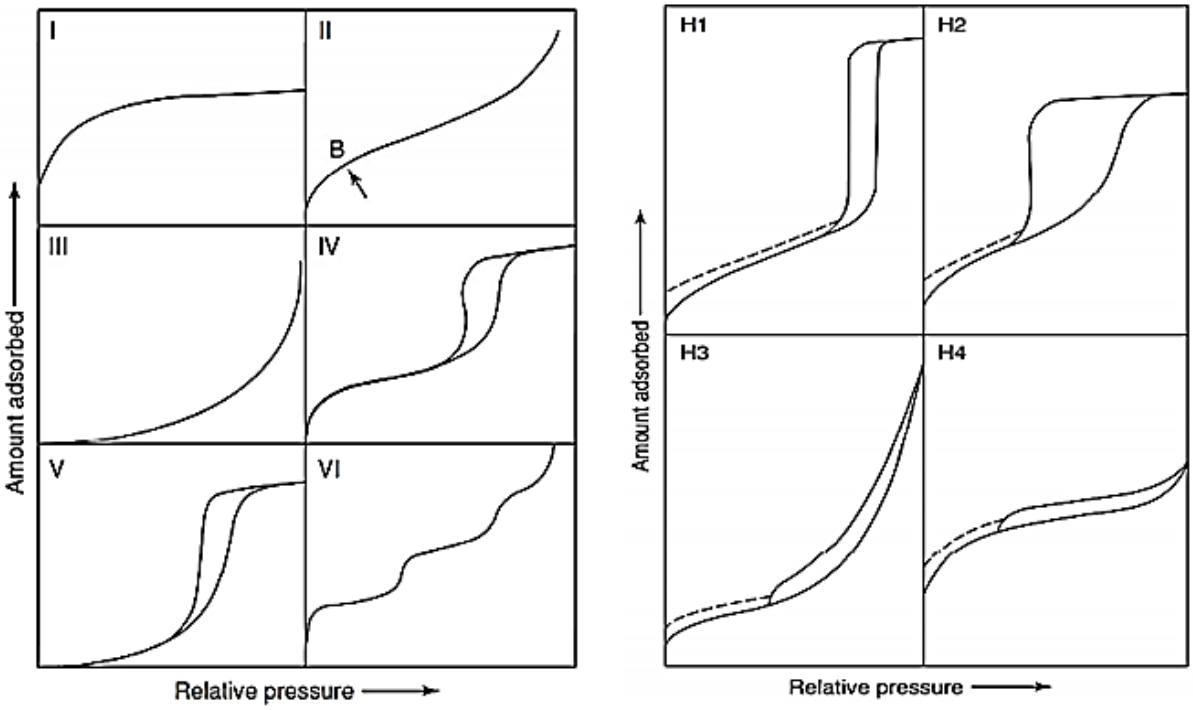


Figure 3. 4. Types of physisorption isotherms and hysteresis loops [10].

In view of the nature of adsorbent, adsorption can generally be classified into six categories as shown in Figure 3.4. Type I isotherms are due to formation of monolayer usually on the surface of microporous solid materials such as silica gel with pore widths ≤ 2nm. The formed monolayer is caused by adsorption of the adsorbate at a relatively low pressure which makes the isotherm to remain flat at low $P/P_o$ but rises as $P/P_o$ approaches 1.0 with condensation taking place. Type II isotherms are usually common with non-porous and macroporous solids (like fumed silica powder) due to formation of multilayer adsorption. Type III isotherm is not very common, it takes place when the heat of liquefaction is greater than that of adsorption with no monolayer formed. Mesoporous solids characteristic of having pore widths between 2nm – 50nm usually produce the type IV isotherm. This type of isotherm has a hysteresis loop because pores filling by adsorbate takes place at higher pressure during adsorption but at a lower pressure during desorption. Minimal interaction between the gas and solid material

results to the uncommon type V isotherm. The last type of isotherm which is also not common is the type VI. It contains steps as a result of sites present in adsorbent that are different in sizes and energy. The pore structures of specific adsorbent are often used to identify the shapes of hysteresis loops. Hence, type H1 is often associated with porous materials known to have narrow distribution of relatively uniform pores. The probability of network effects could result to type H2 loop, this type of hysteresis is synonymous with complex pore structures. The type H3 loop is characteristic of non-rigid aggregates of plate – like particles while the type H4 is observed with complex materials containing both micropores and mesopores [10, 12].

3.1.4.1. Adsorption Isotherm Models

The Langmuir model which is one of the basic methods of isotherm for the process of gas adsorption onto the surface of an adsorbent is based on the following assumptions [12].

1. All sites on the adsorption surface are equivalent
2. Only one molecule of adsorbate can be accommodated on the adsorption site
3. There is no adsorbate – adsorbate interaction
4. Adsorption can only form monolayer on the surface
5. The process of adsorption is dynamic as the rate at which adsorbate adsorb and desorb leads to equilibrium.

In view of these assumptions, the Langmuir isotherm equation as shown below was obtained.

$$\theta = \frac{bP}{1 + bP} \qquad \text{Eq. 3.4}$$

Where $\theta = V/V_m$, with V as the volume of gas at STP and $V_m$ is the volume of gas required to complete a monolayer adsorption on the surface of the adsorbent, b is the Langmuir constant while P is the pressure of adsorbate which means the equation could be written as,

$$\frac{V}{V_m} = \frac{bP}{1 + bP} \qquad \text{Eq. 3.5}$$

The above equation could then be re-arranged as shown in equation 3.6.

$$\frac{P}{V} = \frac{1}{bV_m} + \frac{P}{V_m} \qquad \text{Eq. 3.6}$$

Hence, in obedience to Langmuir isotherm model, a plot of P/V against P should give a straight line graph from which $V_m$ can be obtained. $V_m$ is the reciprocal of the gradient. This value at STP according to equation 3.7 can be used to determine the surface area of the solid sample [13].

$$S = V_m\,(STP) \times N_A \times A_m \qquad \text{Eq. 3.7}$$

Where $N_A$ is the Avogadro's constant and $A_m$ is the cross – sectional area of one molecule of adsorbent which for $N_2$ is 0.162nm.

Meanwhile, as this model is not appropriate to calculate the surface area of several porous materials, there was need for an all embracing model. The BET (Braunauer, Emmett and Teller) which was an enhanced version of the Langmuir model was developed [14]. Equation

3.8 known as the BET equation was used to calculate the surface area of the catalysts studied in this thesis and this equation was based on the following additional assumptions.

1. The adsorbate forms multilayer on the surface
2. The vapour and surface interaction only corresponds to adsorption and desorption
3. Movement of adsorbed molecules from one layer to another are restricted
4. A specific value is assigned to the initial monolayer heat of adsorption while the heat of adsorption gas molecules for subsequent layers is equivalent to the heat of condensation of the gas

$$\frac{P}{V(P_o - P)} = \frac{1}{V_m C} + \frac{(C-1)}{V_m C} \times \frac{P}{P_o} \qquad \text{Eq. 3.8}$$

Where P is the adsorbate pressure at equilibrium, $P_o$ is the saturated vapour pressure while V is the volume of adsorbed gas at $P/P_o$. $V_m$ is the gas volume required for monolayer formation and C is the net heat of adsorption. A plot of $P/V(P_o - P)$ versus $P/P_o$ should give a straight line of $P/P_o$ values between 0.05 – 0.35.

$$V_m = \frac{1}{\text{Slope} + \text{intercept}} \qquad \text{Eq. 3.9}$$

By using the slope, $(C-1)/V_mC$ and the intercept $1/V_mC$ in equation 3.9, $V_m$ can be calculated and the obtained value can then be used to determine the surface area of a solid material.

3.1.4.2. Adsorption in pores

The BJH (Barett, Joyner and Halenda) method was used to calculate the pore size distribution of the catalysts studied in this thesis [14]. This method which is conventionally employed in analysing mesoporous materials is based on the Kelvin equation as shown below.

$$\ln \frac{P}{Po} = \frac{-2.\gamma.Vmolar}{rp.R.T}.\ Cos\ \theta \qquad \text{Eq. 3.10}$$

Where $\gamma$ is the surface tension of liquid nitrogen, $V_{molar}$ is the molar volume, rp is the pore radius, R is the universal gas constant, and T is the temperature while $\theta$ is the contact angle which would be assumed to be zero for the size ranges of pores studied in this report. This equation was based on the following assumptions.

1. The pores are uniform in shape
2. All pores widths are between 2nm and 50nm which is the mesoporous range

The shape of an adsorption or desorption can be influenced by the presence of pores in an adsorbent solid because the equilibrium vapour pressure above condensed liquid in a cylindrical pore with a curved surface is lower than that above a liquid with a flat surface. Hence, vapour condenses at lower $P/P_o$ values in curved surface with wide pores than on a flat surface which has narrow pores fillings at lower pressure. The Kelvin equation is related to equilibrium vapour pressure of a liquid in a small cylindrical pore where the surface of the liquid takes up a regular curvature. It also describes how the equilibrium vapour pressure of a liquid in the pore depends on the pore radius rp, and the contact angle $\theta$. In view of the pressure at which condensation occurs, the radius of the pores can be calculated. The BJH

method involves correction of the pore radius as given by the Kelvin equation. Therefore, the pore diameter data shown in this thesis is BJH corrected.

### 3.1.4.3. Estimation of micropore volume

The t-plot, Micropore analysis (MP), Alpha-S, Dubinin-Radushkevich (DR), Horvath-Kawazoe (HK), Saito-Foley and Dubinin-Astakhov methods have been used to estimate the volume of microporous materials [15]. However, as the t-plot method is one of the most commonly used to determine the volume of microporous materials [16], the pore volume of the material studied in this thesis were reported using the t-plot method, this technique will be discussed further below.

### 3.1.4.4. The t-plot method

This technique which is based on the assumptions that the film thickness on pore walls is uniform and that the film structure is close packed hexagonal was proposed by Lippens and de Boer [17] whereby the statistical thickness with the adsorbed volume of gas expressed in liquid volume is obtained as shown in equation 3.11.

$$T = V_{liq} / S \times 10^4 \text{ (Å)} \qquad \text{Eq. 3.11}$$

Where S is the total surface area, Å = 3.54 (monolayer depth) and $V_{liq} = V_{ads}$ (STP) × 15.47 in the case of nitrogen adsorption at 77K. The layer thickness (t) is calculated as a function of increase in relative pressure ($P/P_o$) of gas molecules covering the surface site. Thereafter, the experimental volume of gas adsorbed by a standard type II isotherm is plotted against statistical thickness for each experimental $P/P_o$ value. [15].

3.1.5. Mass Spectrometry (MS)

In this report mass spectrometry was used to screen all the prepared catalysts for catalytic activity. This instrumental technique is used to identify unknowns and to study molecular structure of applicable compounds. MS typically involves the generation of gas phase molecular ions via a particular ionisation process (for instance electron ionization); these ions get separated according to their mass-to-charge ratio which then undergo fragmentation followed by measurement of their abundance. Equation 3.12 shows the basic process of electron ionization to form molecular ions which are odd – electron radical cations [18, 19].

$$M + e^- = M^{\cdot +} + 2e^- \qquad \text{Eq. 3.12}$$

This molecular radical cation with odd number of electrons could undergo fragmentation to give both a neutral radical and an ion with an even number of electrons as shown below.

$$M^{\cdot +} \rightarrow A^+ + B^{\cdot} \qquad \text{Eq. 3.13}$$

Its fragmentation could also give a molecule and a radical cation as shown in equation 3.14.

$$M^{\cdot +} \rightarrow C^{\cdot +} + D \qquad \text{Eq. 3.14}$$

The mass-to-charge ratio is the physical property measured in MS with the mass expressed in atomic mass units (μ) or Dalton (Da), the charge is in the unit (e) which means the mass-to-charge ratio has dimension of μ/e or Da/e. However, atomic mass units (μ) and (Da) are used

in different contexts. Da is preferred for stoichiometric calculation of mean isotopic masses while masses related to the main isotope of each element are expressed in μ.

All mass spectrometers usually operate under high vacuum (this enables ions to reach the detector without colliding with other gaseous molecules) and contain the following components as shown in Figure 3.5, a sample inlet to introduce relevant compound to be analysed, an ionization source that generates ions from the sample, single or multiple analysers to carry out ions separation and to analyse fragmented ions, a detector for counting ions emitted from the neighbouring analyser and a data processor to produce the mass spectrum.

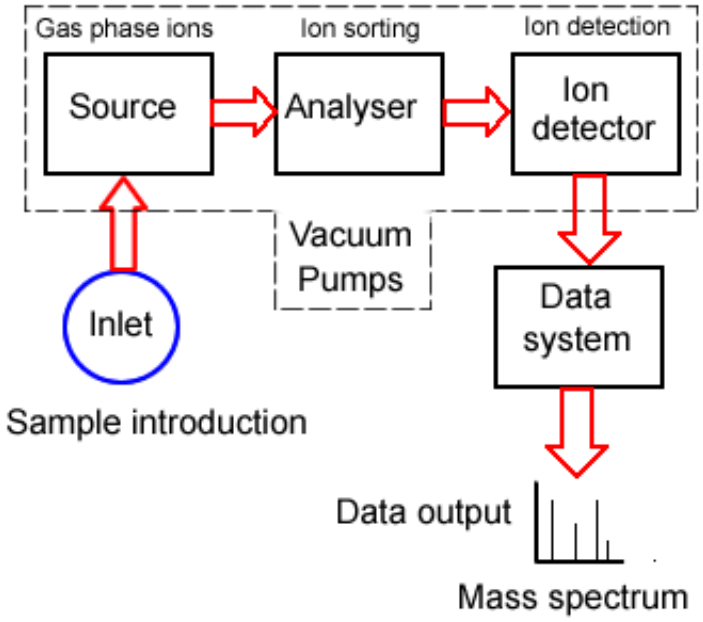


Figure 3. 5. Schematic of a Mass Spectrometry [19]

3.1.5.1. Electron Ionization (EI)

The choice of ionization technique depends on the nature of the sample to be analysed as well as the type of information required from the analysis. Electron ionization (EI), chemical ionization (CI) and field ionization are used for gas-phase ionization. Electrospray ionization (ESI), atmospheric pressure chemical ionization (APCI) and atmospheric pressure photoionization (APPI) are utilised for liquid-phase ion source. While matrix – assisted laser desorption ionization (MALDI), secondary ion mass spectrometry (SIMS), plasma desorption ionization (PDI) and field desorption ionization (FDI) are availed for solid-phase ionization. Meanwhile, fast atom bombardment (FAB) is employed for involatile liquid matrix [17].

However, only EI process would be discussed further as it is the ionization technique used in this thesis. Figure 3.6 shows a typical EI source, it consist of a heated filament that releases electrons which accelerates towards an anode and collides with gaseous molecular samples of high vapour pressure that gets injected directly into the ionization space .

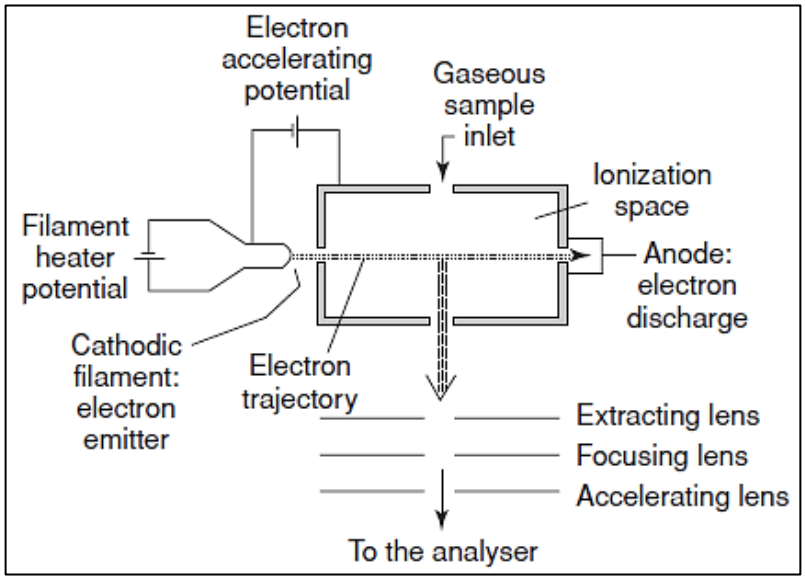


Figure 3. 6. Diagram of an electron ionization source [20]

Every electron generated is related to a wave with wavelength (λ) as shown below

$$\lambda = \frac{h}{mv} \qquad \text{Eq. 3.15}$$

Where h is Planck's constant, m is its mass and v is the velocity. Quantitative measurement could sometimes be carried out in EI technique by using equation 3.16 where number of ion (I) generated per unit time in a volume (V) is linked to the pressure (p), the electron current (*i*) and N as the constant proportionality coefficient [20].

$$I = N\ p\ i\ V \qquad \text{Eq. 3.16}$$

It can be seen in this equation that the pressure is directly correlated with the resulting ionic current.

## 3.2. Experimental

### 3.2.1. Materials

Cobalt (II) acetate tetrahydrate [$(CH_3COO)_2$ Co. $4H_2O$, (AR Grade, 97%)], cobalt (II) nitrate hexahydrate [$Co(NO_3)_2$. $6H_2O$, (AR Grade, 97%)], iron (III) nitrate nonahydrate [$Fe(NO_3)_3$. $9H_2O$, (98%, A.C.S Reagent)], methanol (99.8+% purity, A.C.S Reagent) and sodium borohydride [$NaBH_4$, (Lab. Reagent)] were purchased from Fischer Scientific. Ruthenium (III) nitrosyl nitrate solution [$Ru(NO)(NO_3)_3$] in dilute $HNO_3$ (Lab. Reagent), cobalt (II) acetylacetonate [$Co(C_5H_7O_2)_2$, (A.C.S 97%)], nickel (II) nitrate hexahydrate [$Ni(NO_3)_2$. $6H_2O$, (99%, A.C.S Reagent)] and cobalt (II) chloride hexahydrate [$CoCl_2$. $6H_2O$, (98%, A.C.S Reagent)] were obtained from Sigma Aldrich. Vinyl – terminated

polydimethylsiloxane (PDMS)] elastomer with repeating monomer unit of $(CH_3)_2SiO]n$ (Slygard 184 silicone elastomer, Dow Corning), this polymer kit contains both PDMS elastomer and the curing agent. Deionised water was supplied by the University of Huddersfield.

### 3.2.2. Preparation and curing of polydimethylsiloxane

A mixture of the Slygard 184 Prepolymer and the curing agent was prepared in a 10:1 mix ratio. Approximately 22g was prepared and vigorously mixed in an inert vessel for several minutes until the entire mixture had formed a large number of bubbles which was degassed approximately 20 – 25 mins in a dessicator under vacuum. This degassed PDMS mixture was poured into a petri dish and placed in an oven set to 65°C for 3 hours to cure. Another sample of PDMS was prepared using the same method but without degassing the mixture. Both samples were labelled as degassed and gassed PDMS.

### 3.2.3. Thermal synthesis and characterisation of porous silica powder

Porous silica powder was synthesized by oxidative thermal degradation of PDMS by TG using a TGA 1 Star System (Mettler Toledo, Switzerland). PDMS samples were heated in the range of 25°C – 650°C at a rate of 5°C $min^{-1}$ in air. Attenuated Total Reflectance Fourier Transform infrared (ATR-FTIR) spectra were obtained at resolution $4cm^{-1}$ in the range of 4000 – $400cm^{-1}$ using NICOLET 380 ATR-FTIR Spectroscopy (Thermo Electron Corporation, USA). X-ray diffraction (XRD) measurements were carried out with Bruker D2 phaser (Bruker AXS, D2 Phaser, Germany) at room temperature operated at 40kV using Cu Kα radiation (λ = 1.54060Å). The scan step size was $0.02^o$ and a step time of 5sec over a 2θ

range of 10° – 100° was used. Specific surface areas and porosity of silica powders were determined by $N_2$ physisorption (BET) at 77 K using Micromeritics ASAP 2020 instrument (Micromeritics Instruments Corp. USA).

### 3.2.4. Preparation and characterisation of catalyst support

Fumed silica powder ($S_{BET}$ = 182$m^2$ $g^{-1}$, PV = 0.09$cm^3$ $g^{-1}$) as catalyst support was synthesized by thermal degradation of PDMS [21]. The required amount in grams of a 10:1 mixture of PDMS and curing agent (Slygard 184 silicone elastomer, Dow Corning) was degassed under vacuum to remove trapped air bubbles. The degassed mixture was cured at 65°C for 3 hours and the as-cured PDMS film was heated under air in a furnace (Carbolite 3216, UK) at 500°C for 1 hour to obtain silica powder. Specific surface areas and porosity of the powder were determined by $N_2$ physisorption (BET) at 77 K using Micromeritics ASAP 2020 instrument (Micromeritics Instruments Corp. USA).

### 3.2.5. Swelling in method (SIM) of catalysts preparation

This swelling in technique was used to prepare different percentage by weight content of cobalt, iron and nickel based FT catalysts. Hence, for ease of understanding, preparation using each metal would be explained.

**Cobalt based catalysts:** Approximately 10wt.% (worked example of cobalt content calculation is shown in appendix 1) of silica-supported cobalt catalysts were prepared, by respectively mixing 5 ml each (3.1 mol $dm^{-3}$) solution of cobalt acetate, cobalt nitrate and cobalt acetylacetonate in methanol into three different portions of 8g PDMS. These mixtures of cobalt precursor and PDMS were then degassed under vacuum to remove entrapped air

bubbles followed by solvent evaporation at 65°C for 3 hours. 0.8g each of curing agent were added to the evaporated mixtures and cured at 65°C for 3 hours. The prepared as-cured composites of cobalt precursors and PDMS catalysts were divided into two batches. The first batch of catalyst was calcined in vacuum under the flow of nitrogen at 500°C for 1hr and was labelled as 10% (Co-A/PDMS, Co-AA/PDMS and Co-N/PDMS). To obtain 10% $Co/SiO_2$ catalysts, the second batch was calcined under air at 500°C for 1 hour. To prepare 5wt.% and 2.5wt.% of $Co/SiO_2$ catalysts, 5 ml (1.5 mol $dm^{-3}$) and 2 ml (2 mol $dm^{-3}$) each of the respective solutions of cobalt precursors (acetate, nitrate and acetylacetonate) were mixed into three portions each of 8g and 9g PDMS then the above procedure for degassing and curing (by adding one-tenth of curing agent to each PDMS sample) was repeated followed by calcination in air at 500°C for 1 hr. The prepared catalysts were labelled Co-A/$SiO_{2(SIM)}$, Co-AA/$SiO_{2(SIM)}$ and Co-N/$SiO_{2(SIM)}$ in respect to their cobalt percent content by weight, where Anion (A = acetate, AA = acetylacetonate, N = nitrate) designates the cobalt salt while SIM stands for the preparation procedure used. Another set of 2.5wt%, 5wt% and 10wt% $Co/SiO_2$ catalysts using cobalt nitrate precursor were prepared and promoted with 0.5wt% of ruthenium. These catalysts were named as 2.5wt% Co-N/Ru/$SiO_{2(SIM)}$, 5wt% Co-N/Ru/$SiO_{2(SIM)}$ and 10wt% Co-N/Ru/$SiO_{2(SIM)}$.

**Iron and nickel based catalysts:** 2.5wt.%, 5wt% and 10wt.% (worked example of cobalt content calculation is shown in appendix 1) of $Fe/SiO_2$ catalysts were synthesized by mixing 3 ml (1.4 mol $dm^{-3}$), 6 ml of 1.5 mol $dm^{-3}$ and 3 mol $dm^{-3}$ each of iron nitrate solution into three different portions of 9g PDMS. The degassing and curing step as already explained was followed and the catalyst was calcined under the same oxidative condition as used for cobalt based silica-supported catalyst.

To prepare 2.5wt.%, 5wt.% and 10wt.% of $Ni/SiO_2$ catalyst, 2 ml (2 mol $dm^{-3}$), 5ml (1.5 mol $dm^{-3}$) and 4 ml (3.4 mol $dm^{-3}$) each of nickel nitrate solution were mixed respectively into 9g,

8g and 7g PDMS. The degassing, curing and oxidative calcination processes as above were followed to obtain the final catalyst product.

### 3.2.6. Cobalt deposition by incipient wetness impregnation method

Cobalt based catalyst was also prepared by the incipient wetness impregnation technique so as to compare their catalytic activity with the ones synthesized by the swelling in method. To synthesize 10wt.% $Co/SiO_2$ catalyst, 0.521g of as prepared fumed silica ($S_{BET}$ = 182$m^2$ $g^{-1}$, PV = 0.1$cm^3$ $g^{-1}$) was contacted with 1 ml each (1 mol $dm^{-3}$) solution of cobalt precursors (acetate, nitrate and acetylacetonate) in methanol respectively then dried at 110°C for 24 hrs followed by calcination under air at 350°C for 2hrs. The catalyst was labelled as Co-A/$SiO_{2(IWIM)}$, Co-AA/$SiO_{2(IWIM)}$ and Co-N/$SiO_{2(IWIM)}$ where IWIM stands for the technique. 5wt.% and 2.5wt.% $Co/SiO_2$ catalyst was prepared by respectively mixing 1ml each of 0.5 mol $dm^{-3}$ and 0.4 mol $dm^{-3}$ solutions of cobalt acetate, nitrate and acetylacetonate into 0.551g and 0.912g of as-prepared fumed silica powder. The same process of drying and calcination was followed to complete the preparation of the catalyst. Their labelling was also the same save for the percentage content of cobalt.

### 3.2.7. Catalyst preparation by the colloidal route coupled with the swelling in method

10ml (1 mol $dm^{-3}$) solution of cobalt chloride in methanol was reduced with 2ml (1.89 mol $dm^{-3}$) aqueous solution of sodium borohydride. To obtain 2.5wt.%, 5wt.% and 10wt.% of silica-supported nanoparticle cobalt catalyst, 2ml, 3ml and 4ml of the colloidal cobalt were respectively mixed into 4.5g, 3.3g and 2.1g of PDMS. The degassing and curing procedures as previously discussed were followed and the as-cured composite of colloidal cobalt

precursor and PDMS was calcined under air at 500°C for 1hr. The catalyst was labelled as 2.5wt.% Co-NP/$SiO_2$, 5wt.% Co-NP/$SiO_2$ and 10wt.% Co-NP/$SiO_2$.

## 3.3. Practical Application of Methods

### 3.3.1. Thermogravimetric Analysis (TGA)

Thermal degradation profile of prepared catalyst was studied by TG using a TGA 1 Star System (Mettler Toledo, Switzerland). Approximately 10g of sample was heated from 25°C – 625°C at a rate of 10°C $min^{-1}$ under a mixture of 80% $O_2$ in 20% $N_2$ atmospheric condition.

### 3.3.2. Fourier Transform Infrared - Attenuated Total Reflectance (FTIR- ATR) Spectroscopy

Spectra information of catalysts was collected at resolution 4$cm^{-1}$ in the range of 4000 – 400$cm^{-1}$ using NICOLET 380 FTIR-ATR Spectroscopy (Thermo Electron Corporation, USA). Background spectrum was initially collected to correct for noise, then approximately 10mg of catalyst sample was used to perform spectrum scan, this was followed by correcting for ATR and baseline of the obtained spectrum.

### 3.3.3. Powder X-ray Diffraction

Powder X-ray diffraction (p-XRD) measurements for all synthesized catalyst was carried out with Bruker D2 phaser (Bruker AXS, D2 Phaser, Germany) at room temperature operated at 40kV using Cu Kα radiation (λ = 1.54060Å). The scan step size was $0.02^o$ and a step time of 5sec over a 2θ range of 10° – $100^o$ was used. The catalyst average particle sizes in diameter was calculated using the Scherrer equation [8] which has been discussed previously.

### 3.3.4. Nitrogen Adsorption

Surface area by $N_2$ physisorption (BET method), pore volume by t-plot method for all catalysts as well as their support were determined at 77 K after degassing at 150°C for almost 8 hours using Micromeritics ASAP 2020 instrument (Micromeritics Instruments Corp. USA).

### 3.3.5. Mass Spectrometry (MS)

The catalysts were tested for catalytic activity in Fischer-Tropsch (FT) synthesis reaction using HPR 20 QMS sampling system Mass Spectrometry (Hiden Analytical, England. UK). FT synthesis reaction was carried out in an upward flow glass tube fixed bed reactor ($d_{int}$ = 3.4mm) inserted into the furnace with a catalyst loading of 50mg. The process was operated at atmospheric pressure, at temperature of 350°C, 450°C and 550°C held for 60mins respectively using constant ramp rate of 10°C $min^{-1}$ with molar ratio of $H_2/CO = 4$. Before the reaction, almost all the catalysts were reduced insitu in 8% hydrogen/helium at 500°C for 5hrs at 10°C $min^{-1}$ with a flow rate of 30ml $min^{-1}$ regulated by a mass flow controller (5850S Brooks Instruments. UK). Silica-supported nickel catalyst was reduced at 600°C for 60mins at 10°C $min^{-1}$ under the same atmospheric condition as above, in reactor controlled by Eurotherm temperature controller (Eurotherm. UK). The thermocouple of the Eurotherm was in direct contact with the catalyst to ensure an accurate temperature measurement. A schematic of the catalyst testing reaction set-up is shown in Figure 3.7. After reduction, the catalyst was cooled down to 30°C while being flushed with helium before the temperature was increased to the desired condition to carry out FT synthesis. The MS was set to a pressure of $1.3 \times 10^{-6}$ torr and the ionic current of CO measured (in terms of the level of CO) before and after reaction was taken. A typical mass spectrometry plot of ionic current of CO and methane against temperature and time is shown in appendix 2.

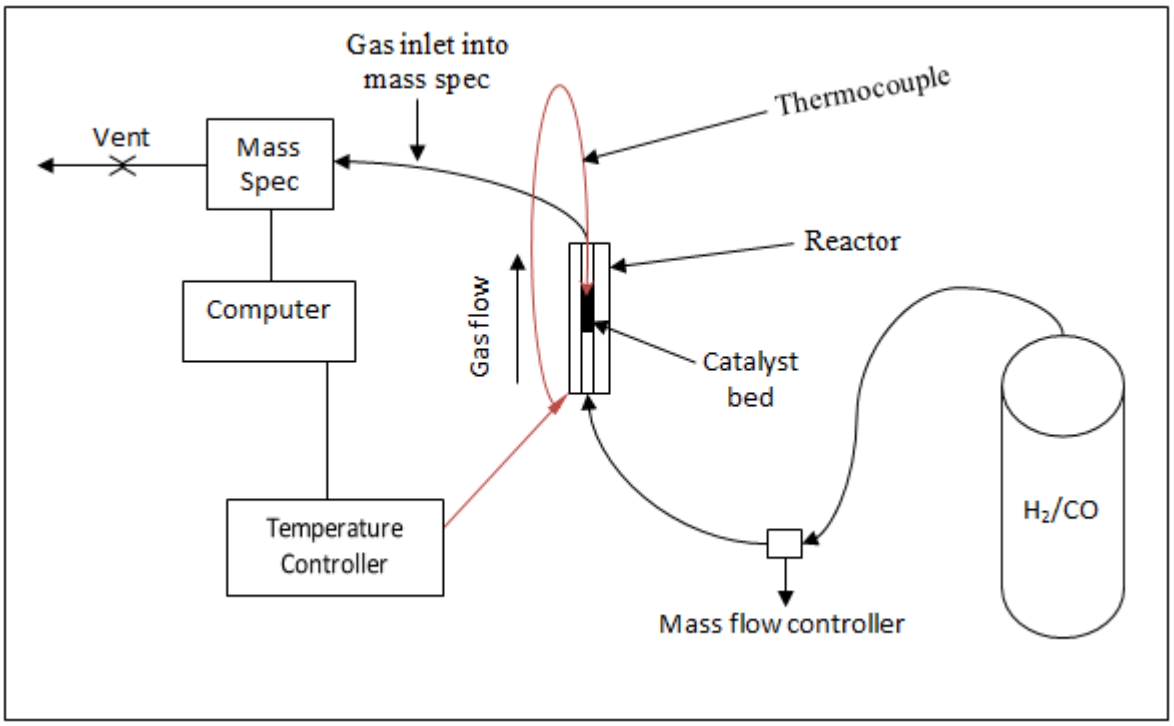


Figure 3. 7. Schematic of catalyst testing reaction set up

$$\text{CO conversion / \%} = \text{normalised ion current}\ \frac{\text{CO}\left(\text{before reaction - after reaction}\right)}{\text{CO (before reaction)}} \times 100 \qquad \text{Eq.3.16}$$

The amount of CO conversion (%) based on the level of its measured ion current which was normalised by the relative sensitivity of CO was calculated using equation 3.16. The worked example of calculation using equation 3.16 is shown in appendix 3

$$CH_4 \text{ formation / \%} = \text{normalised ion current}\ \frac{(CH_4 \text{ formed})}{(\ CH_4 \text{ formed + converted CO})} \times 100 \qquad \text{Eq.3.17}$$

The amount of methane formed (%) based on the level of its measured ion current that was normalised by the relative sensitivity of methane was calculated according to equation 3.17. The worked example using equation 3.17 is shown in appendix 4.

The ratio of methane formed to CO conversion was calculated according to equation 3.18

$$\text{Ratio of } CH_4 \text{ formation to CO conversion} = \frac{CH_4 \text{ formation / \%}}{\text{CO conversion / \%}} \qquad \text{Eq. 3.18}$$

Worked example of calculation using equation 3.18 is shown in appendix 5.

**References**


1. Polymer Science and Technology. Thermogravimetric Analysis. Institute of Science and Technology. *Lecture manual 522 Chapter 12*. **2012**, 84.
2. Calleja Aguado, R. Catalytic conversion of biomass. Norwegian University of Science and Technology. Department of Chemical Engineering. *Master Thesis*. **2013**, 27.
3. Joe Van Gompel, P. The Fundamentals of Infrared Spectroscopy. Midac Corporation. *FTIR Notes and Research*. **2013**, 1.
4. Harrick, N. J. Internal reflection spectroscopy; *Interscience Publishers: New York*. **1967**.
5. Yugay, D. Attenuated Total Reflectance Fourier Transform Infrared Spectroscopy. *Analytical Spectroscopy*. **2011**, 1.
6. Smart, L.E.; Moore, E.A. Solid state chemistry: an introduction. 2012: CRC press.
7. Teaching Advanced Physics. Episode 530: X-ray diffraction. *Institute of Physics*, **2011**.
8. Khodakov, A.Y.; Chu, W.; Fongarland, P. Advances in the development of novel cobalt Fischer-Tropsch catalysts for synthesis of long-chain hydrocarbons and clean fuels. *Chemical Reviews*. **2007**, 107, 1692.
9. Barbara, L.D.; Christine, M. Clark. Louisiana State University. Eastern Michigan University. X-ray Powder Diffraction (XRD). *Geochemical Instrumentation and Analysis*. December **2013**.
10. Neimark, A. V.; Sing, K. S. W.; Thommes, M. Surface Area and Porosity. *Handbook of Heterogeneous Catalysis*. **2008**, 721.

11. Sing, K.S. Reporting physisorption data for gas/solid systems with special reference to the determination of surface area and porosity (Recommendations 1984). *Pure and applied chemistry*. **1985**, 57, 603.

12. Langmuir, I. The adsorption of gases on plane surfaces of glass, mica and platinum. *Journal of the American Chemical society*. **1918**, 40, 1361.

13. The Porous Materials, Inc. BET-202A. *BET Sorptometer for Surface Area and Pore Size Analysis Brochure*. **2008**.

14. Brunauer, S.; Emmett, P.H.; Teller, E. Adsorption of gases in multimolecular layers. *Journal of the American Chemical Society*. **1938**, 60, 309.

15. Lowell, S. Characterization of porous solids and powders: surface area, pore size and density. Springer. **2004**, 16.

16. Micromeritics, Gas Sorption Analysis Brochure. *Microporosity*. January **2001**.

17. Lippens, B.C.; De Boer, J. Studies on pore systems in catalysts: V. The t method. *Journal of Catalysis*. **1965**, 4, 319.

18. Galen, P.M.V. *Mass Spectrometry (A guide for novel users).* **2005**.

19. Waters/Micromass Marketing. Principles of Mass Spectrometry. *LC-MS booklet*. **2000**.

20. de Hoffmann, E.; Stroobant, V. *Mass Spectrometry: Principles and Applications, 3rd Edition.* **2007**.

21. Camino, G.; Lomakin, S.; Lageard, M. Thermal polydimethylsiloxane degradation. Part 2. The degradation mechanisms. *Polymer*. **2002**, 43, 2011.

# CHAPTER 4

# Thermal synthesis of porous silica with different surface area and pore volume

This chapter discusses the influence of changes in isothermal time and temperature on the mass loss of PDMS samples which was used for thermal synthesis of porous silica powder, the effect of time and temperature on the surface area and pore volume of the synthesized silica and its characterisation using XRD, FTIR and nitrogen adsorption techniques were also covered.

## 4.0. Introduction

Silica powders have enormous relevance over a wide range of application such as catalyst support, in construction of light weight building materials, adsorbents and as sensors for humidity [1-3].

Numerous methods have been reported for the synthesis of silica powders which involve chemical vapour deposition [4], plasma methods [5], co-condensation [6], sol-gel processing [7, 8], micro-emulsion [9], combustion and hydrothermal techniques [10-12]. Silica powders prepared by these methods have unique properties such as large surface area, fine particle size and good dispersion. However, the optimum temperature (1027°C) of synthesis is often high and the experimental set up can be complex or multi-stage [5, 12]. Hence, an alternative and easier route of producing porous silica powders could have numerous commercial benefits.

Thermal degradation of polydimethylsiloxane (PDMS) has been extensively studied for over 6 decades and it is well known that the oxidative decomposition of PDMS produces white silica powder [13-22]. It has been shown that, as the rate at which PDMS is heated increases, evaporation of oligomers (dimethylsiloxanes) and other gaseous waste produced by decomposition also increases [18]. Camino et al. [19] proposed that thermal degradation process of PDMS occurs through at least two steps and two of these steps could overlap at a higher rate of heating. This degradation process involves formation of cyclic oligomers through a molecular mechanism of Si-O bond cleavage and a radical mechanism which occurs through homolytic Si-$CH_3$ bond scission at high temperature to produce methane by hydrogen abstraction. Zhou et al [20] found that at low temperature, polysiloxanes with phenyl side groups have higher thermal stability than those with only methyl group. It has

been reported recently [22] that PDMS crosslinked with polymethylmethoxysiloxane (PMMOS) reduces the oxidative degradation of carbon portion in PDMS.

Although, a large amount of work has been carried out on this polymer, most of these studies were based on the kinetics, mechanisms and stability of the thermal degradation of polydimethylsiloxane with emphasis on the gaseous products [18 – 22]. While very little attention has been paid to silica powder as the product.

## 4.1. Results and discussion

### 4.1.1. Thermal synthesis of porous silica powder

Fumed silica powder was synthesized through thermal oxidative degradation of both degassed and gassed PDMS sample but as both samples gave similar oxidative behaviour. Fig. 4.1 shows a typical TG/DTG mass loss curve for PDMS to $SiO_2$ using degassed sample heated in air up to 650°C at a set rate of 5°C $min^{-1}$. Here, we observe an experimental mass loss of 47.5% while Camino et al [18] reported an experimental mass loss of 47% with a deviation of ±15% for the decomposition of PDMS to silica.

The peak A (at around 350°C) indicates partial degradation of PDMS to $SiO_2$ while peak B at 500°C shows complete degradation of PDMS to $SiO_2$ [18]. In the process of PDMS decomposing to silica powder, this mass loss could be due to oxidative thermal breakdown of the methyl functional groups to form water vapour, carbon dioxide and the possible loss of volatiles present in the PDMS which might be plasticizers (such as vinyl – methyl – siloxane which helps in enhancing the polymer's flexibility and to improve its flow properties) from the slygard 184 [23, 24]. This mass loss can also be assigned to evaporation of gaseous silicon based oligomers from the PDMS as Camino et al. [19] showed that the

major degradation products of PDMS are a mixture of oligomers(dimethylsiloxanes), $CO_2$ and water vapour.

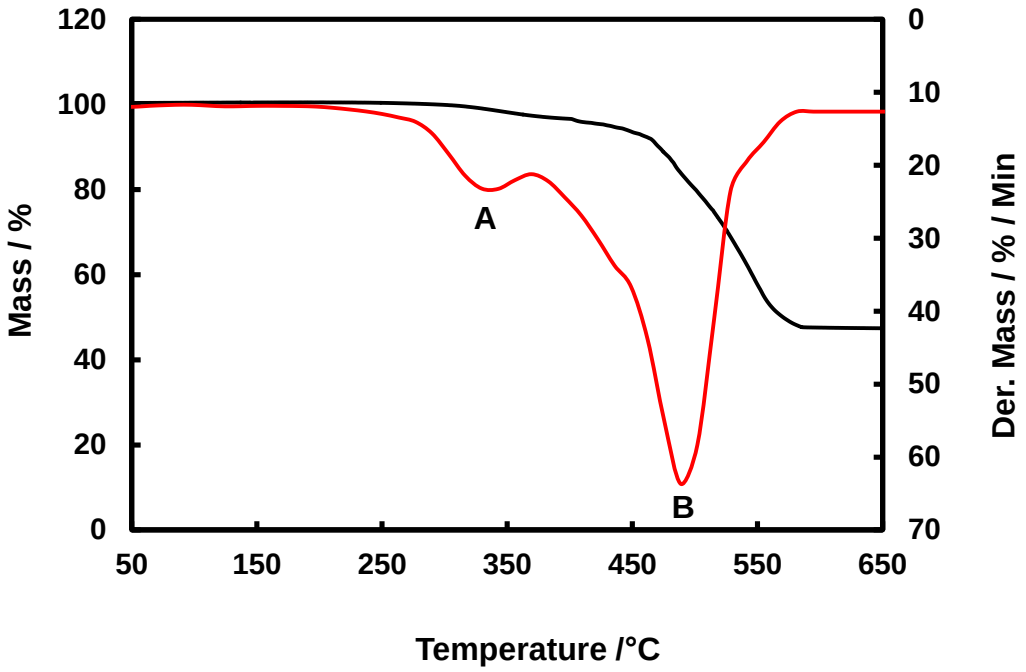


Figure 4. 1. TG/DTG mass loss of PDMS to $SiO_2$ using degassed sample heated in air at 5°C $min^{-1}$ to 650°C

4.1.2. FTIR and XRD analysis of synthesized silica powder

To investigate if the powder obtained from oxidative thermal degradation of PDMS was actually silica powder and also to show that there was no conversion of PDMS to $SiO_2$ when heat treated at 300°C, the spectra of untreated PDMS, sample heat treated at 300, 450 and 650°C were considered. Figs. 4.2 (a) – (b) showed spectra with sharp absorption bands at 1260$cm^{-1}$, 787$cm^{-1}$ and weak bands at 1412$cm^{-1}$, 843$cm^{-1}$ and 688$cm^{-1}$ which indicate C-H and Si-C stretching vibrations of $CH_3$ and Si-$CH_3$ due to the presence of carbon.

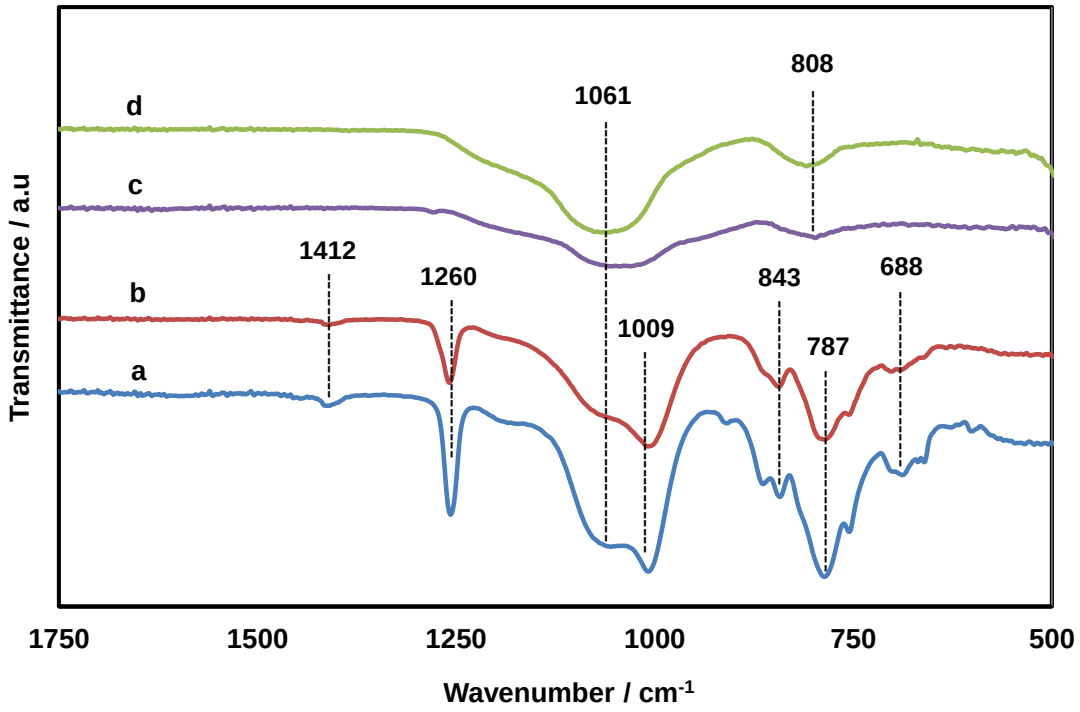


Figure 4. 2. IR spectra of (a) untreated degassed PDMS, (b) degassed PDMS sample heated to 300°C at 5°C $min^{-1}$ in air while (c) – (d) is synthesized porous $SiO_2$ powder from PDMS heated in air at 5°C $min^{-1}$ to 450 and 650°C.

The two shouldered bands at 1061$cm^{-1}$ and 1009$cm^{-1}$ are indicative of Si-O-Si vibration. These peaks are all reflective of the presence of PDMS. It is worth to note that the spectrum of degassed PDMS sample heat treated at 300°C has the same absorption peaks as that of untreated PDMS which suggest that PDMS did no convert to $SiO_2$ at this temperature.

In Figs. 4.2 (c) – (d), the Si-O-Si vibration peaks still remained but change from shouldered bands to one broad peak at 1061$cm^{-1}$ which indicates cleavage of the Si-O bond in the long polymer chains. The broad band at 808$cm^{-1}$ points to Si-O-Si symmetric stretching vibrations. These bands strongly suggest the presence of porous silica powder and it is in agreement with those reported by Han et al [22]. An XRD analysis was also carried out to confirm that heat treated PDMS at 300°C remained as PDMS while sample heated at 450

and 650°C resulted to silica powder. Figs. 4.3 (a) – (b) did not give any peak which confirms that treated PDMS at 300°C retained PDMS properties. While Figs. 4.3 (c) – (d) showed broad peaks at $2\theta = 22.5^{o}$ indicating the presence of amorphous silica structure which supports the FT-IR data.

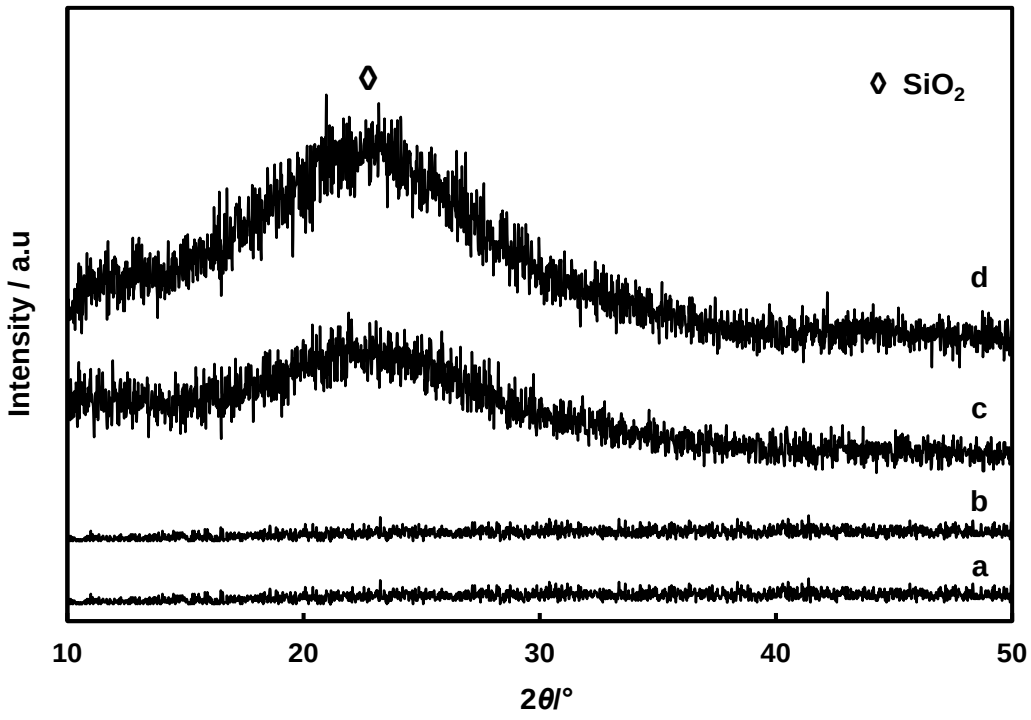


Figure 4. 3. XRD patterns of (a) untreated degassed PDMS sample, (b) PDMS heated in air at 5°C $min^{-1}$ to 300°C and (c) – (d) synthesized porous $SiO_2$ powder from PDMS heated in air at 5°C $min^{-1}$ to 450 and 650°C. (◊) – XRD peak intensity of amorphous $SiO_2$ at $2\theta = 22.5$

A visual inspection of untreated PDMS and its heated samples at 300, 450 and 650°C was also carried out to further support the results shown by FT-IR and XRD. It can be seen in Figs. 4.4 (a) – (b) that PDMS heated at 300°C only goes from flexible to brittle (loss of plasticizers), the silica synthesized at 450°C as shown in Fig. 4.4(c) appears to be quite

granulated while silica which was thermally prepared at the highest temperature seems to be a fine powder.


Figure 4. 4. Images of (a) untreated degassed PDMS, (b) brittle form of PDMS and (c) – (d) synthesized porous $SiO_2$ powder from PDMS heated in air at 5°C $min^{-1}$ to 450 and 650°C

4.1.3. Isothermal time and temperature effect on mass loss of decomposed PDMS samples

The influence of changes in isothermal time at a set temperature and changes in temperature at a set isothermal time on the mass loss of decomposed PDMS (degassed and gassed) samples was studied as shown in Table 4.1. The mass loss recorded by degassed and gassed PDMS samples heated in air to 300°C for 20hrs could be attributed to removal of plasticizers from the PDMS.

Table 4. 1. Isothermal time and temperature effect on mass loss of PDMS samples

| Temperature / °C | Dwell time, hr | Mass loss of degassed PDMS to silica, % ± SD | Mass loss of gassed PDMS to silica, % ± SD |
|---|---|---|---|
| 300 | 20 | 10.3 ± 0.2 | 10.7 ± 0.4 |
| 350 | 14 | 24.8 ± 0.3 | 26.1 ± 0.4 |
| 450 | 1 | 41.9 ± 0.6 | 42.2 ± 1.0 |
| | 3 | 40.9 ± 0.2 | 40.2 ± 0.5 |
| | 7 | 41.1 ± 0.2 | 40.7 ± 1.0 |
| | 15 | 42.7 ± 0.5 | 40.6 ± 0.6 |
| 500 | 1 | 43.1 ± 0.4 | 46.9 ± 0.7 |
| | 5 | 44.6 ± 0.4 | 48.8 ± 1.2 |
| 550 | 3.5 | 47.6 ± 0.7 | 46.4 ± 0.5 |

The mass loss obtained when temperature increased to 350°C after 14 hours indicates an initial conversion of PDMS to silica as shown by thermal analysis data. Samples heated at 450°C held for 1 and 7 hrs showed similar mass losses while degassed samples heated to the same temperature but held for 3 and 15 hrs resulted in increases in mass losses when compared to gassed PDMS samples. It is expected that gassed samples should record higher mass loss than degassed samples due to the presence of excess oxygen but this was not the

case. This anomaly could be due to sudden loss of mass in the gassed PDMS samples due to possible vigorous reaction, scattering part of the sample from the crucible during oxidation. When the temperature was increased to 500°C for 1hr, an increase in mass loss of 1.2% for degassed and 4.7% for gassed samples relative to those heated at 450°C for 1hr was observed. Meanwhile, an increased mass loss of 3.8% for gassed PDMS in relation to the degassed samples, both heated to 500$^{o}$C for 1hr was obtained. When the time at constant temperature of 500°C was increased to 5hrs, an increased mass loss of 4.2% was observed for gassed samples compared to the degassed. The relative increase in mass losses (1.2% and 4.7%) is most certainly due to higher temperature which enhances the rate of oxidation giving rise to increased mass loss. The marked increase in mass losses of 3.8% and 4.2% seen at 500°C for 1 and 5 hrs could be due to the presence of excess oxygen in gassed PDMS samples and could also be attributed to random variation as shown by their SD values when compared to their degassed counterparts. The impact of increase in temperature can also be seen in mass loss of PDMS heated to 550°C for 3.5 hrs especially the degassed samples. Overall, it has been shown that higher temperature at a set time results to more mass loss in both samples while no significant difference in mass was observed between degassed and gassed PDMS samples.

### 4.1.4. Influence of isothermal time and temperature on structural properties of silica

The structural properties of the synthesized silica powder were examined as a function of its route of preparation as well as temperature and isothermal time dependence. Table 4.2 shows the effect of changes in isothermal time at constant temperature and that of increase in temperature with time on the BET surface area, micropore and total pore volume of silica

Table 4. 2. Influence of isothermal time and temperature on BET surface area, micropore volume and total pore volume of porous silica from PDMS samples

| Temp / °C | Time, hr | Mean $S.A_{BET}$, $m^2 g^{-1}$ ± SD [a] | MPV, $cm^3 g^{-1}$ [a] | TPV, $cm^3 g^{-1}$ [a] | Mean $S.A_{BET}$, $m^2 g^{-1}$ ± SD [b] | MPV, $cm^3 g^{-1}$ [b] | TPV, $cm^3 g^{-1}$ [b] |
|---|---|---|---|---|---|---|---|
| 450 | 1 | 153 ± 2.9 | 0.06 | 0.07 | 115 ± 3.2 | 0.05 | 0.06 |
| | 3 | 95 ± 3.2 | 0.04 | 0.05 | 86 ± 1.3 | 0.03 | 0.04 |
| | 7 | 93 ± 1.8 | 0.04 | 0.05 | 85 ± 3.5 | 0.03 | 0.04 |
| | 15 | 53 ± 2.0 | 0.02 | 0.03 | 43 ± 0.6 | 0.02 | 0.03 |
| 500 | 1 | 114 ± 0.6 | 0.05 | 0.06 | 109 ± 3.8 | 0.05 | 0.06 |
| | 5 | 91 ± 0.9 | 0.04 | 0.05 | 80 ± 2.5 | 0.03 | 0.04 |
| 550 | 3.5 | 89 ± 2.6 | 0.04 | 0.05 | 88 ± 4.2 | 0.03 | 0.04 |

[a] Surface area and pore volume of porous silica prepared from degassed PDMS samples

[b] Surface area and pore volume of porous silica prepared from gassed PDMS samples

prepared using degassed and gassed PDMS. It can be seen in both samples that as isothermal time at 450°C increases from 1 to 15 hrs, there is a steady decrease in surface area and as temperature increases to 500°C at 1hr, the surface area also reduced relatively compared to the surface area of silica prepared at 450°C for 1 hr. A decrease in surface area can also be noticed as isothermal time increases to 5 hrs at 500°C. The trend displayed by the textural properties of silica powder at 450°C is most likely due to increase in isothermal time which could bring about possible destructive oxidative transformation taking place during thermal treatment resulting in the collapse of the $SiO_2$ external surface [25]. This structural breakdown would further make the surface of the $SiO_2$ powder less accessible to nitrogen gas molecules during physisorption. The decrease in surface area at 500°C for 1hr when compared to that at 450°C for 1hr is likely due to increase in temperature while the

reduced surface area at 500°C for 5 hrs is again due to increase in isothermal time. It can also be seen that there is decrease in micropore and total pore volume of the synthesized silica as a function of increase in isothermal time at constant temperature as well as increase in temperature at constant isothermal time, save at 450°C for 3 and 7 hrs. This decline in pore volume as a result of increase in time and temperature is likely attributed to the collapse of the pores and shrinkage of the silica frameworks. The similar pore volume for silica at 450°C for 3 and 7 hrs suggests slight impact of increase in time at this temperature which seems quite reasonable, because the related surface area recorded at these times were 95 and 93 $m^2 g^{-1}$ for degassed and 86 and 85 $m^2 g^{-1}$ for gassed PDMS samples.

It is worth noting that the micropore volume data shown in this work are in agreement with those recently reported by Bo Sun et al [26]. Moreover, the standard deviation for the pore volume was not reported as the values were close to zero.

In general it can be seen that increase in isothermal time at constant temperature and increase in temperature at constant time has deleterious effects on BET surface area and pore volume of porous silica powder prepared from degassed and gassed PDMS samples. Synthesized silica powder from degassed PDMS samples had enhanced surface area and pore volume. Overall silica powder at 450°C for 1hr has the most improved surface area and pore volume, followed by those at 500°C for 1hr while silica heated at 450°C for 15 hrs recorded the least surface area, micropore and total pore volume.

## 4.2. Conclusions

It has been shown that PDMS treated at 300°C for 20 hrs goes from flexible to brittle PDMS due to loss of plasticizers without conversion to $SiO_2$, powder residue obtained at 450°C during oxidative thermal degradation of PDMS samples heated to 650°C is confirmed to be silica as shown by FT-IR and XRD data and also by visual inspection. Isothermal studies indicated that increase in isothermal time at constant temperature and increase in temperature at constant time has deleterious effect on the textural properties of synthesized porous silica. Silica powder from degassed and gassed PDMS samples heated at 450°C and 500°C held at 1hr respectively recorded the most reasonable BET surface area and pore volume. A typical t-plot of the porous synthesized silica powder as shown in appendix 6 suggests that the material is microporous. Hence, the t-plot method was used to report micropore volume of obtained silica powder.

Meanwhile, it was considered that this reported technique could have potential application for the synthesis of silica-supported catalyst for Fischer-Tropsch synthesis.

**References**

1. Sadasivan, S.; Rasmussen, D.H.; Chen, F.P.; Kannabiran, R.K. Preparation and characterization of ultrafine silica. Colloids and Surfaces A: *Physicochemical and Engineering Aspects*. **1998**, 132, 45.

2. Suciu, C.V.; Iwatsubo, T.; Deki, S. Investigation of a colloidal damper. *Journal of Colloid and Interface Science*. **2003**, 259, 62.

3. Flikkema, E.; Bromley, S.T. A new interatomic potential for nanoscale silica. *Chemical Physics Letters*. **2003**, 378, 622.

4. Awaji, N.; Ohkubo, S.; Nakanishi, T.; Aoyama, T.; Sugita, Y.; Takasaki, K. Thermal oxide growth at chemical vapor deposited SiO2/Si interface during annealing evaluated by difference X-ray reflectivity. *Applied physics letters.* **1997**, 71, 1954.

5. Hong, R.; Ding, J.; Li, H. Thermodynamic analysis and experimental verification for synthesizing silicon nitride nanoparticles using RF plasma CVD. *China Particuology*. **2003**, 1, 162.

6. Doyle, A. M.; Hodnett, B. K. "Adjusting the porous and structural properties of mesoporous silica by the addition of organic modifiers." *Journal of non-crystalline solids*. **2006**, 352, 2193.

7. Pinto, P.R.; Mendes, L.C.; Dias, M.L.; Azuma, C. Synthesis of acrylic-modified sol–gel silica. *Colloid and Polymer Science*. **2006**, 284, 529.

8. Martínez, J.R.; Palomares-Sánchez, S.; Ortega-Zarzosa, G.; Ruiz, F.; Chumakov, Y. Rietveld refinement of amorphous $SiO_2$ prepared via sol–gel method. *Materials Letters*. **2006**, 60, 3526.

9. Wang, W.; Fu, X.a.; Tang, J.; Jiang, L. Preparation of submicron spherical particles of silica by the water-in-oil microemulsion method. *Colloids and Surfaces A: Physicochemical and Engineering Aspects*. **1993**, 81, 177.

10. Jang, H.D. Experimental study of synthesis of silica nanoparticles by a bench-scale diffusion flame reactor. *Powder Technology*. **2001**, 119, 102.

11. Hong, R.Y.; Feng, B.; Ren, Z.Q.; Xu, B.; Li, H.Z.; Zheng, Y.; Ding, J.; Wei, D.G. Thermodynamic, hydrodynamic, particle dynamic, and experimental analyses of silica nanoparticles synthesis in diffusion flame. *The Canadian Journal of Chemical Engineering*. **2009**, 87, 143.

12. Mitra, A.; Kirby, C.W.; Wang, Z.; Huang, L.; Wang, H.; Huang, Y.; Yan, Y. Synthesis of pure-silica MTW powder and supported films. *Microporous and Mesoporous Materials*. **2002**, 54, 175.

13. Clarson, S.J.; Semlyen, J.A. Cyclic polysiloxanes: 1. Preparation and characterization of poly(phenylmethylsiloxane). *Polymer*. **1986**, 27, 1633.

14. Doskočilová, D.; Schneider, B.; Jakeš, J. NMR spectra of systems with restricted motion: Cross-linked polymer gels. *Journal of Magnetic Resonance*. **1978**, 29, 79.

15. Thomas, T.H.; Kendrick, T. Thermal analysis of polydimethylsiloxanes. I. Thermal degradation in controlled atmospheres. *Journal of Polymer Science Part A-2: Polymer Physics*. **1969**, 7, 537.

16. Grassie, N.; Macfarlane, I.; Francey, K. The thermal degradation of polysiloxanes—II. Poly (methylphenylsiloxane). *European Polymer Journal*. **1979**, 15, 415.

17. Kissinger, H.E. Reaction kinetics in differential thermal analysis. *Analytical chemistry*. **1957**, 29, 1702.

18. Camino, G.; Lomakin, S.; Lazzari, M. Polydimethylsiloxane thermal degradation Part 1. Kinetic aspects. *Polymer*. **2001**, 42, 2395.

19. Camino, G.; Lomakin, S.; Lageard, M. Thermal polydimethylsiloxane degradation. Part 2. The degradation mechanisms. *Polymer*. **2002**, 43, 2011.

20. Zhou, W.; Yang, H.; Guo, X.; Lu, J. Thermal degradation behaviors of some branched and linear polysiloxanes. *Polymer degradation and stability*. **2006**, 91, 1471.

21. Deshpande, G.; Rezac, M.E. The effect of phenyl content on the degradation of poly (dimethyl diphenyl) siloxane copolymers. *Polymer degradation and stability*. **2001**, 74, 363.

22. Han, Y.; Zhang, J.; Shi, L.; Qi, S.; Cheng, J.; Jin, R. Improvement of thermal resistance of polydimethylsiloxanes with polymethylmethoxysiloxane as crosslinker. *Polymer degradation and stability*. **2008**, 93, 242.

23. Corning, D. Sylgard 184 Silicone Elastomer. *Technical Data Sheet*. **2008**.

24. Wypych, G. Plasticizers use and selection for specific polymers. *ChemTec Publishing: Toronto, Canada*. **2004**, 273.

25. Li, Z.; Shen, X.; Yao, H.; Li, J. Preparation of ultrafine silica powders. *Journal of Materials Science Letters*. **2002**, 21, 995.

26. Sun, B.; Guo, C.; Yao, Y.; Che, S. Functional group-template integrated ABC copolymer silicone surfactant directing for highly hydrophobic mesoporous silica. *Journal of Materials Chemistry*. **2012**, 22, 19076.

# CHAPTER 5

# Characterisation of Fischer-Tropsch catalyst

This chapter covers results and discussion on TG, XRD, FTIR and nitrogen adsorption characterisation of cobalt based Fischer-Tropsch catalyst prepared by the swelling in method and incipient wetness impregnation technique. It also discusses results on characterisation of iron and nickel based catalysts which were synthesized by the swelling in method.

## 5.1. Results and discussion

### 5.1.1. Characterisation of catalyst calcination

The thermal oxidative behaviour for a range of synthesized catalysts was examined using TG and DTG. This includes catalyst prepared with cobalt, iron, nickel and ruthenium metals, using the swelling-in and colloidal methods with a polymer (PDMS) as the initial support which decomposed to silica as the final support. Specifically, 10% by weight of metal precursor of the as-prepared PDMS supported (Co-A/PDMS, Co-AA/PDMS, Co-N/PDMS, Co-N-Ru/PDMS, Fe/PDMS and Ni/PDMS) catalysts, which were all synthesized by the novel method (SIM); were investigated by TG-DTG measurement from 25 to 625°C using a rate of 10°C $min^{-1}$ under the flow of a mixture of 80% $O_2$ in 20% $N_2$ atmospheric condition. Fig. 5.1 shows the oxidative degradation of PDMS supported cobalt acetate (10% Co-A/$PDMS_{(SIM)}$) to form 10% Co-A/$SiO_{2(SIM)}$.

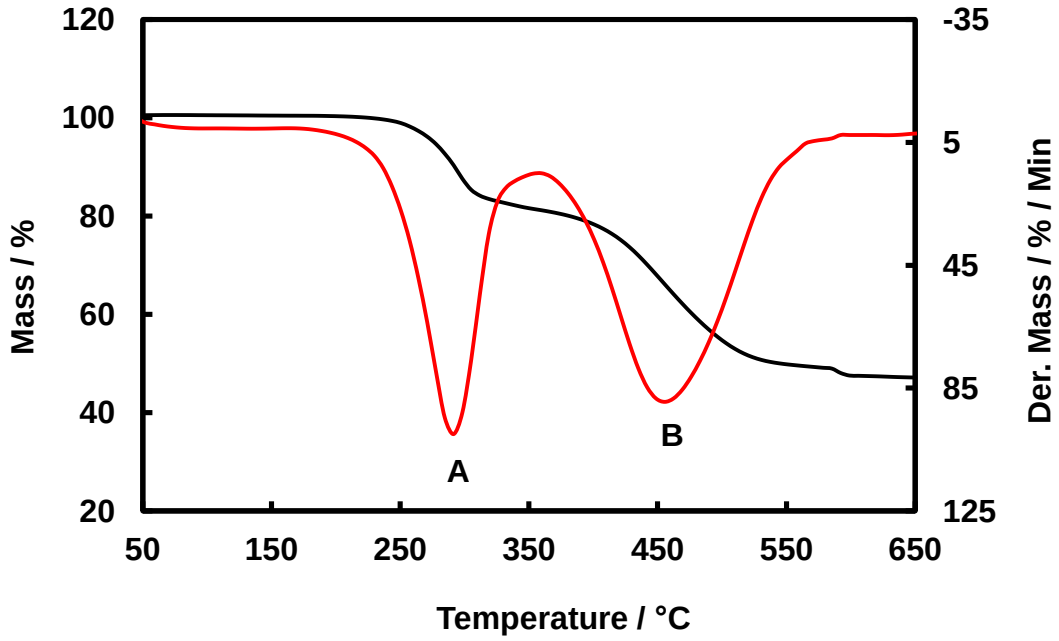


Figure 5. 1. TG/DTG mass loss curve of 10% Co-A/PDMS $_{(SIM)}$ to 10% Co-A/$SiO_{2(SIM)}$ catalyst heated at a rate of 10°C $min^{-1}$ under the flow of a mixture of 80% $O_2$ and 20% $N_2$.

It can be seen that there is a slight mass loss at temperature region beginning from 46°C till around 182°C, with two peaks at A (292°C) and B (450°C) with an experimental mass loss of 52.5%. This mass loss could be contributed by 7.2% for removal of hydrated water (46°C – 182°C). Peak A suggests removal of carbon dioxide (17.7%) via acetate combustion to form cobalt oxide [1, 2]. Peak B indicates degradation of PDMS to silica powder (18.9%) while the remaining 8.7% of the total experimental mass loss could probably be due to loss of polymeric volatiles such as plasticizers and oligomers. In fact, G. Camino et al. [3] has shown that the major degradation products of PDMS are a mixture of oligomers, $CO_2$ and water vapour.

Meanwhile, it is important to mention that previous work has shown that the degradation process of PDMS to silica occurs through two competing steps [3, 4]. Therefore, the presence of cobalt metal could have affected the decomposition behaviour of PDMS to silica as shown by the large peak at point B which could possibly be a combination of two peaks.

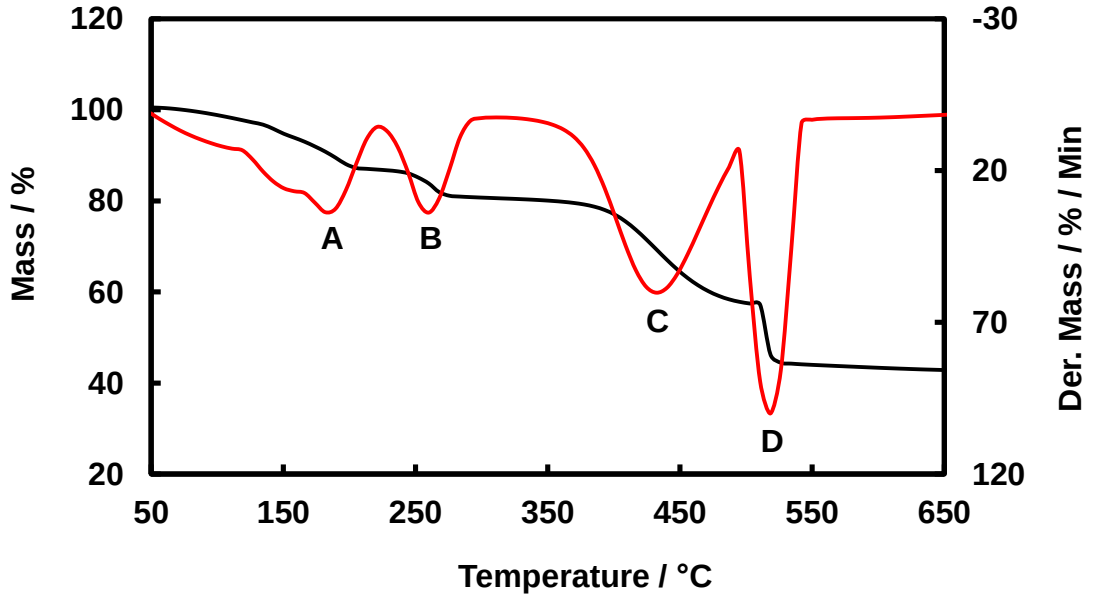


Figure 5. 2. TG/DTG mass loss curve of 10% Co-AA/PDMS $_{(SIM)}$ to 10% Co-AA/$SiO_{2(SIM)}$ catalyst heated at a rate of 10°C $min^{-1}$ under the flow of a mixture of 80% $O_2$ and 20% $N_2$.

Fig. 5.2 is TG/DTG mass loss curve for the degradation of cobalt acetylacetonate supported on PDMS. It shows mass loss at temperature range of 49 – 119°C, and four peaks at A (182°C), B (260°C), C (432°C) and D (518°C). The measured mass loss was 56.8% and it could be due to loss of 7% for removal of absorbed water, while the peaks at A and B might be due to loss of carbon dioxide (17.1%) to form cobalt oxide. The peaks at C and D could contribute to the rest mass loss (32.7%) due to partial and complete conversion of PDMS to silica as well as loss of other volatiles present in the polymer [3, 4].

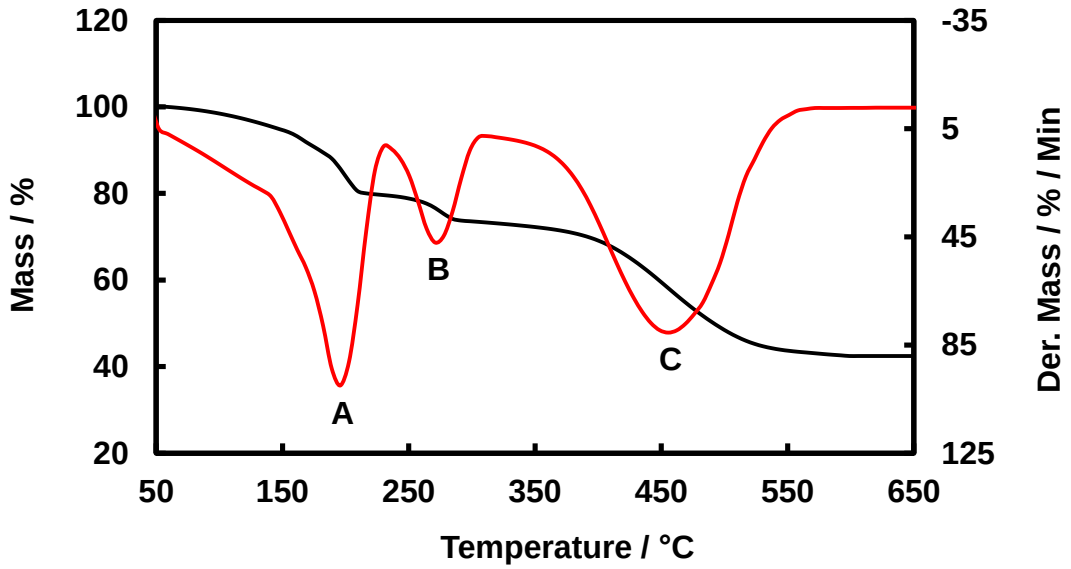


Figure 5. 3. TG/DTG mass loss curve of 10% Co-N/PDMS$_{(SIM)}$ to 10% Co-N/SiO$_{2(SIM)}$ catalyst heated at a rate of 10°C min$^{-1}$ under the flow of a mixture of 80% $O_2$ and 20% $N_2$.

Fig. 5.3 which is the decomposition of PDMS supported cobalt nitrate to Co/SiO$_2$ catalyst shows a steady mass loss at temperature between 46 – 134°C and three peaks at A (189°C), B (271°C) and C (456°C) with an experimental mass loss of 57.6%. It has been reported that the degradation of cobalt nitrate proceeds with the release of nitrogen dioxide, water and oxygen [5]. Hence, the measured mass loss could be due to loss of water (6.2%) at 134°C,

oxygen (5.5%) at peak A while peak B represents nitrates decomposition to lose nitrogen dioxide (15.8%). The rest mass loss (30.1%) is likely due to conversion of PDMS to silica as shown at peak C and also from possible removal of silicon based waste gases [6].

The decomposition behaviour of ruthenium promoted cobalt nitrate supported on PDMS as shown in Fig. 5.4 was also studied.

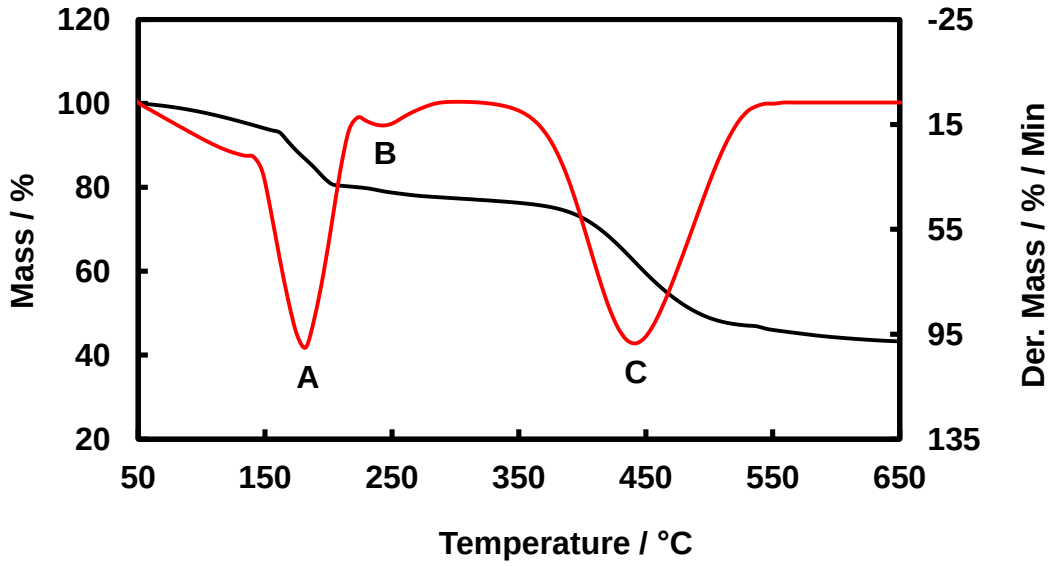


Figure 5. 4. TG/DTG mass loss curve of 10% Co-N-Ru/PDMS$_{(SIM)}$ to 10% Co-N-Ru/SiO$_{2(SIM)}$ catalyst heated at a rate of 10°C min$^{-1}$ under the flow of a mixture of 80% $O_2$ and 20% $N_2$.

It shows a similar degradation pattern as the un-promoted Co/SiO$_2$ catalyst prepared from cobalt nitrate (Fig. 5.3) except a reduced decomposition shown by the flattened DTG peak at point B which could be due to the presence of ruthenium modifying the thermal behaviour of cobalt. Hence, slowing down its rate of decomposition [7]. The experimental mass loss (56.1%) again could be due to loss of water, oxygen and nitrogen dioxide and the evaporation of dimethylsiloxanes from PDMS.

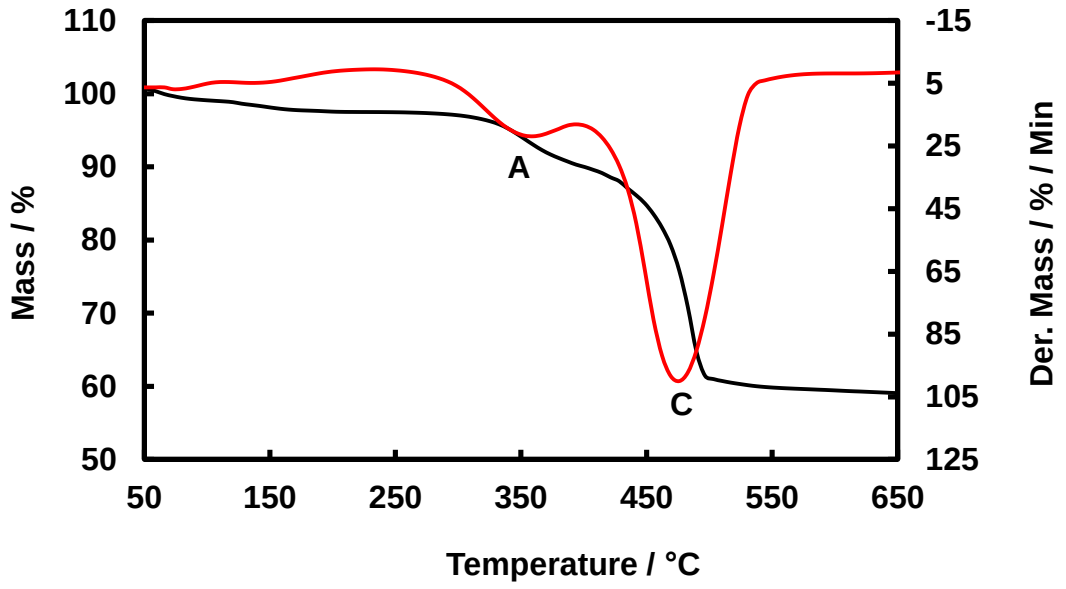


Figure 5. 5. TG/DTG mass loss curve of 10% Co-NP/PDMS$_{(SIM)}$ to 10% Co-NP/SiO$_{2(SIM)}$ catalyst heated at a rate of 10°C min$^{-1}$ under the flow of a mixture of 80% $O_2$ and 20% $N_2$.

The TG/DTG mass loss curve for PDMS supported cobalt nanoparticles is shown in Fig. 5.5, it has a steady mass loss with two peaks at A (340°C) and B (470°C), with a total measured mass loss of 40.1%. This experimental mass loss is mainly from the decomposition activities of PDMS to silica [3, 4] .

Decomposition of PDMS supported iron nitrate composites to silica-supported iron catalyst is shown in Fig. 5.6, it has a total mass loss of 44.7% and it can be seen that there is a steady mass loss at temperature range of 25 – 120°C and two peaks at A (197°C) and 464°C indicated by B. The mass loss could be loss of hydrated water (4.5%), while the combustion of ferric nitrate at peak A could lead to loss of 11.4% (nitrogen dioxide) and 4% for oxygen to produce iron oxide. The rest mass loss (24.8%) could be from oxidative thermal conversion of PDMS to silica as well as loss of other polymeric properties present in the PDMS [5].

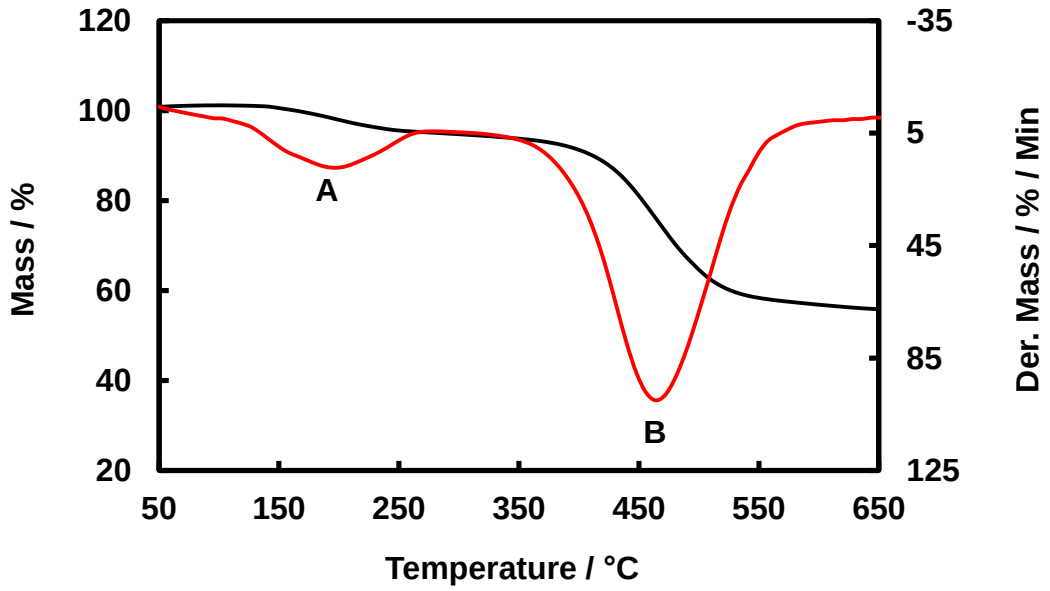


Figure 5. 6. TG/DTG mass loss curve of 10% Fe/PDMS$_{(SIM)}$ to 10% Fe/SiO$_{2(SIM)}$ catalyst heated at a rate of 10°C min$^{-1}$ under the flow of a mixture of 80% $O_2$ and 20% $N_2$.

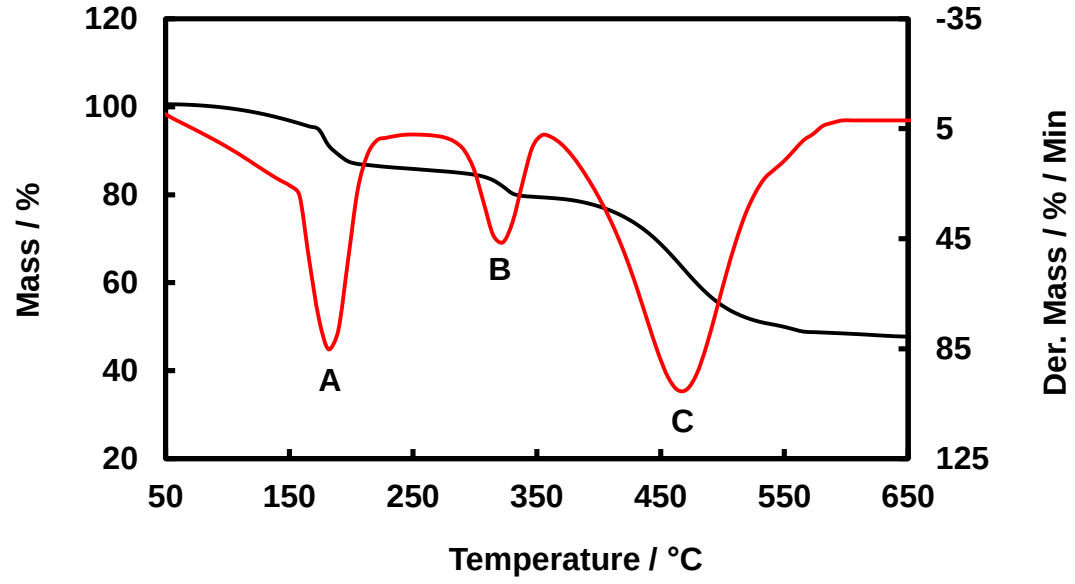


Figure 5. 7. TG/DTG mass loss curve of 10% Ni/PDMS$_{(SIM)}$ to 10% Ni/SiO$_{2(SIM)}$ catalyst heated at a rate of 10°C min$^{-1}$ under the flow of a mixture of 80% $O_2$ and 20% $N_2$.

TG/DTG mass loss curve for nickel supported on PDMS is shown in Fig. 5.7, it shows a steady mass loss at temperature region of 40 – 150°C, three peaks designated as A (181°C), B (322°C) and C (464°C) with an experimental mass loss of 55.1%. The steady mass loss could refer to 6.2% for removal of hydrated water, peaks and A and B could be attributed to loss of nitrogen dioxide (15.8%) and oxygen (5.5%) due to oxidative thermal breakdown of nickel nitrate to form nickel oxide. Decomposition of PDMS to silica which is designated as peak C as well as other evaporated polymeric volatiles in the course of the whole decomposition process could have contributed to the rest mass loss of 27.6% [3].

### 5.1.2. Catalysts characterisation by FTIR-ATR, XRD and Nitrogen adsorption

The physicochemical properties of calcined catalysts, which were prepared using both the swelling in and incipient wetness impregnation methods, were investigated using FTIR, XRD and nitrogen adsorption. FTIR analysis allowed the surface chemical properties to be examined, whilst XRD and nitrogen adsorption allowed characterisation of the internal structure and surface area. Figs. 5.8 (a) – (d) show a typical FTIR spectra of silica-supported cobalt based catalyst using cobalt precursor of acetate, acetylacetonate and nitrate and also ruthenium promoted cobalt nitrate synthesized by the swelling in method. It can be seen that all the spectra display similar spectroscopic behaviour except Fig. 5.8 (d) which has an intense and broad peak at 1090$cm^{-1}$. The absorption bands at 1090, 1016 and 798$cm^{-1}$ all agree with the formation of $SiO_2$ bond structure with peaks at 1090$cm^{-1}$ and 1016$cm^{-1}$ corresponding to asymmetric stretching vibration of Si-O-Si bond while that of 798$cm^{-1}$ indicates Si-O-Si bond symmetric vibration [8]. The narrow peaks at 663 and 565$cm^{-1}$ indicate vibration of Co(III)-O bond in $Co_3O_4$. These peaks could also be attributed to Co-O stretching.

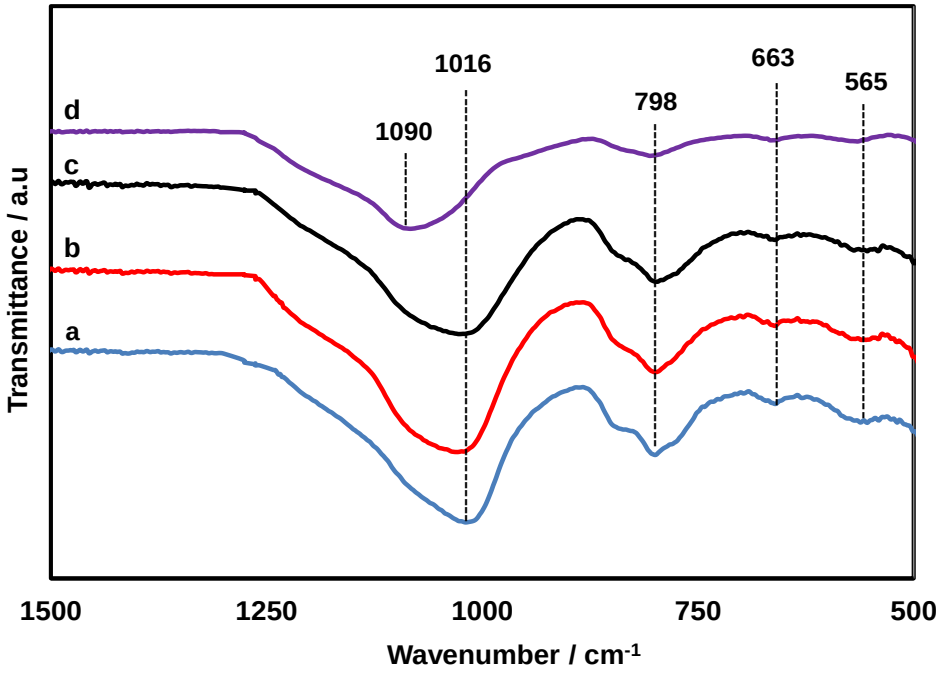


Figure 5. 8. FTIR spectra of (a) 10% Co-A/$SiO_{2(SIM)}$, (b) 10% Co-AA/$SiO_{2(SIM)}$, (c) 10% Co-N/$SiO_{2(SIM)}$ and (d) 10% Co-N-Ru/$SiO_{2(SIM)}$ catalysts prepared by the swelling in method

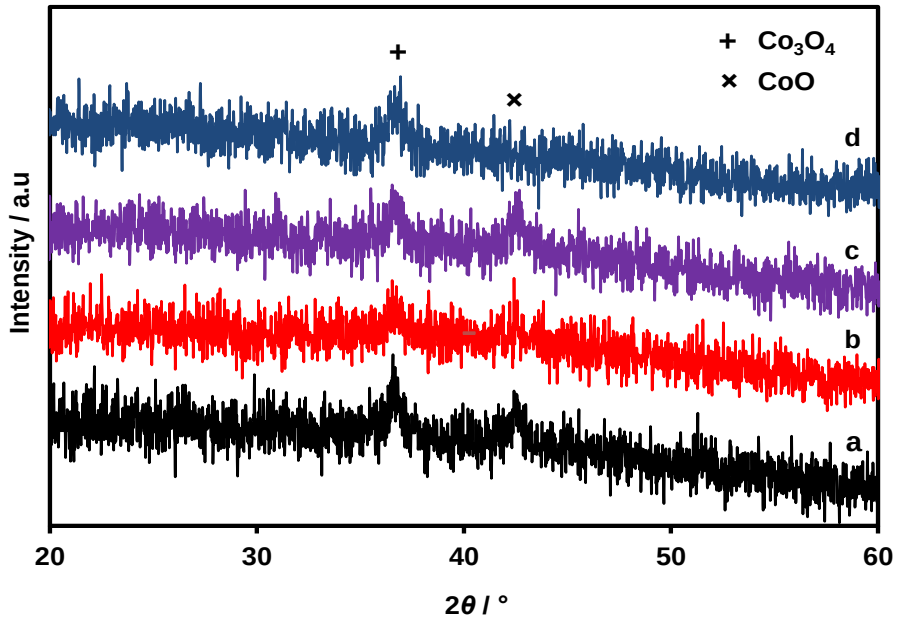


Figure 5. 9. XRD peaks patterns of (a) 10% Co-A/$SiO_{2(SIM)}$, (b) 10% Co-AA/$SiO_{2(SIM)}$, (c) 10% Co-N/$SiO_{2(SIM)}$ and (d) 10% Co-N-Ru/$SiO_{2(SIM)}$ catalysts prepared by the swelling in method. (+) – $Co_3O_4$ peak intensity at $2\theta = 36.9^{o}$. (×) – CoO peak intensity at $2\theta = 42.8^{o}$

This result confirms the thermal characterisation data and it is in agreement with those reported by Fouad et al [9].

XRD peaks patterns of the catalyst as shown in Figs. 5.9(a) – (d) was also examined to verify FTIR data. The peaks indexed at $2\theta = 36.9°$ and 42.8° relate to $Co_3O_4$ and CoO respectively. This XRD data is in agreement with FTIR results and it suggests that most of the cobalt oxides are present on the silica surface [9-11]. Table 5.1 shows XRD derived particle sizes, BET surface area, t-plot micropore volume, total pore volume and average pore width of silica-supported cobalt based catalyst prepared by the swelling in method.

Table 5. 1. XRD and $N_2$ adsorption results for cobalt catalyst prepared by the SIM

| Catalyst designation | Co content, wt.% | XRD derived crystallite diameter, nm | | S.A $_{BET}$, $m^2\ g^{-1}$ | MPV, $cm^3\ g^{-1}$ | TPV, $cm^3\ g^{-1}$ | $P_w$, Å |
|---|---|---|---|---|---|---|---|
| | | $Co_3O_4$ [a] | $Co^o$ [b] | | | | |
| Co-A/$SiO_{2(SIM)}$ | 2.5 | 13.0 | 9.8 | 462 | 0.11 | 0.25 | 21.6 |
| | 5 | 13.0 | 9.8 | 445 | 0.10 | 0.23 | 20.7 |
| | 10 | 22.0 | 16.5 | 407 | 0.09 | 0.21 | 20.5 |
| Co-AA/$SiO_{2(SIM)}$ | 2.5 | 16.8 | 12.6 | 485 | 0.12 | 0.26 | 21.2 |
| | 5 | 13.0 | 9.8 | 402 | 0.09 | 0.20 | 20.3 |
| | 10 | 16.2 | 12.2 | 400 | 0.07 | 0.20 | 20.0 |
| Co-N/$SiO_{2(SIM)}$ | 2.5 | 17.7 | 13.3 | 504 | 0.12 | 0.26 | 20.7 |
| | 5 | 13.0 | 9.8 | 500 | 0.11 | 0.25 | 20.2 |
| | 10 | 13.4 | 10.1 | 438 | 0.09 | 0.22 | 19.8 |
| Co-N-Ru/$SiO_{2(SIM)}$ | 2.5 | 15.0 | 11.3 | 430 | 0.11 | 0.22 | 20.3 |
| | 5 | 16.3 | 12.2 | 399 | 0.10 | 0.20 | 19.9 |
| | 10 | 13.0 | 9.8 | 349 | 0.09 | 0.17 | 19.8 |

[a] calculated using Scherrer equation [12, 13]

[b] calculated using $d(Co^o) = 0.75*d(Co_3O_4)$ [14]

The cobalt crystallite diameter sizes were calculated using the Scherrer equation [12, 13], the expected sizes of metallic cobalt were estimated according to the method reported by Venezia et al. [14] whereby the calculated particle sizes of $Co_3O_4$ is multiplied by 0.75. The proximity of these estimated particle sizes of Co metal to those measured by transmission electron microscopy (TEM) and $H_2$-chemisorption has been well documented [10, 14, 15]. Moreover, previous report has stated that XRD derived cobalt crystallites sizes in the range of 6 – 25nm are relatively quite accurate [16]. This implies that the calculated cobalt particle sizes might be relatively close to experimental values. It can be seen in Table 5.1 that there is a steady decrease in surface area and pore volume as the amount of cobalt increases which could indicate partial blockage of silica pores by species of cobalt oxide [2, 11, 17, 18].

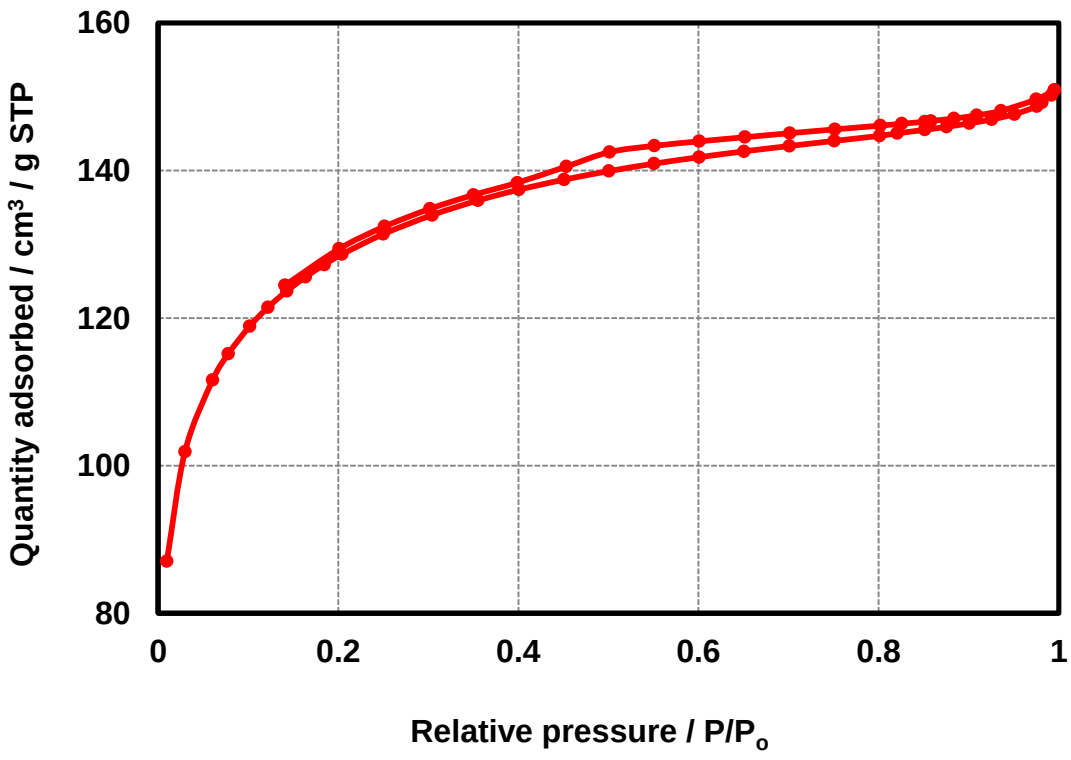


Figure 5. 10. Nitrogen adsorption-desorption isotherm of cobalt based silica-supported catalyst synthesized by the swelling in method.

The t-plot method was used to report the pore volume of the catalyst because of the features demonstrated by its typical nitrogen adsorption – desorption isotherm as shown in Fig. 5.10. It can be seen that it is a pseudo type I isotherm (as the plateau is basically due to micropores filling and not monolayer limit), it indicates that the material is microporous while it also has an H4 hysteresis loop which suggest the presence of some mesopores with particles that are assembled in a coherently loosed manner [19, 20]. The average pore width as shown in Table 5.1 and the typical BJH pore size distribution (as shown in appendix 7) of cobalt based silica-supported catalyst synthesized by the swelling in method, further support the presence of mesopores in the material

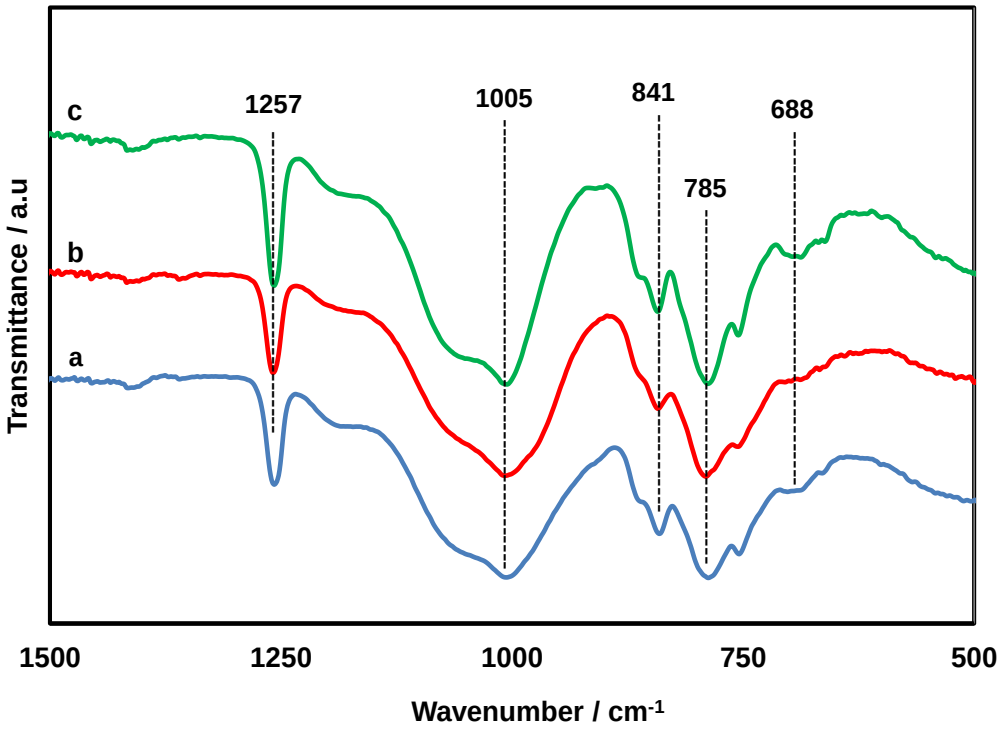


Figure 5. 11. FTIR spectra of (a) 10% Co-A/PDMS$_{(SIM)}$, (b) 10% Co-AA/PDMS$_{(SIM)}$ and (c) 10% Co-N/PDMS$_{(SIM)}$ catalysts prepared by SIM but calcined under $N_2$ in vacuum.

Figs. 5.11 (a) – (c) show spectra of polydimethylsiloxane (PDMS) supported cobalt based catalyst prepared from precursor of acetate, acetylacetonate and nitrate via the proposed method but calcined under the flow of nitrogen in vacuum. Absorption bands at 1257, 841, 785 and 688cm$^{-1}$ indicate C-H and Si-C stretching vibrations of $CH_3$ and Si-$CH_3$. The peak at 1005cm$^{-1}$ relates to Si-O-Si vibration. All these peaks reflect the presence of PDMS [8] which suggest that the polymeric support of cobalt catalyst synthesized by the swelling in method but calcined under the atmospheric condition already described did not decompose to silica but retained its polymeric properties. It is worth to note that the spectra for this catalyst showed no absorption peak for cobalt oxides species which indicates that cobalt oxides are scarcely on the surface of the polymeric support [21]. XRD data for this catalyst could not be obtained as diffraction pattern for cobalt oxides species was not detected probably due to the highly amorphous nature of the support which confirms lack of infrared absorption peak for cobalt. Besides, nitrogen adsorption – desorption measurement could not be carried out as well due to the rubber-like plastic nature of the sample.

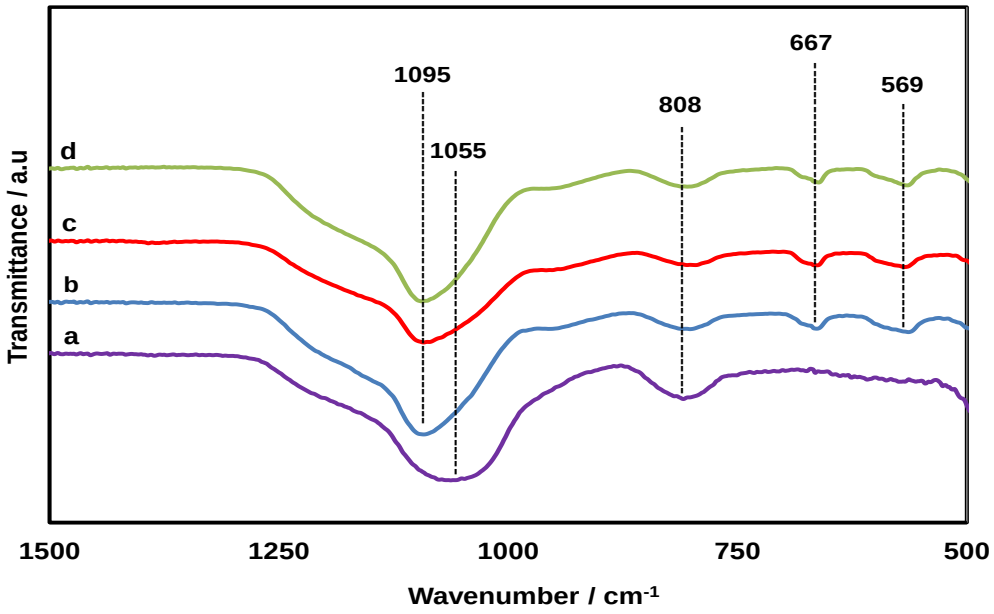


Figure 5. 12. FTIR spectra of (a) $SiO_2$, (b) 10% Co-A/$SiO_{2(IWIM)}$, (c) 10% Co-AA/$SiO_{2(IWIM)}$, (d) 10% Co-N/$SiO_{2(IWIM)}$ catalysts prepared by the incipient wetness impregnation method.

FTIR spectra of silica-supported cobalt based catalyst prepared by incipient wetness impregnation method using precursor of cobalt acetate, acetylacetonate and nitrate as well as the spectrum of porous silica powder is shown in Figs. 5.12 (a) – (d).

It can be seen that the intense bands at 1095 and 1055cm$^{-1}$ and the broad peak at 808cm$^{-1}$ which correspond with the formation of silica are present in all the spectra while the narrow bands at 667 and 569cm$^{-1}$ which indicate the presence of $Co_3O_4$ or CoO are absent in the silica support without cobalt [22-24].

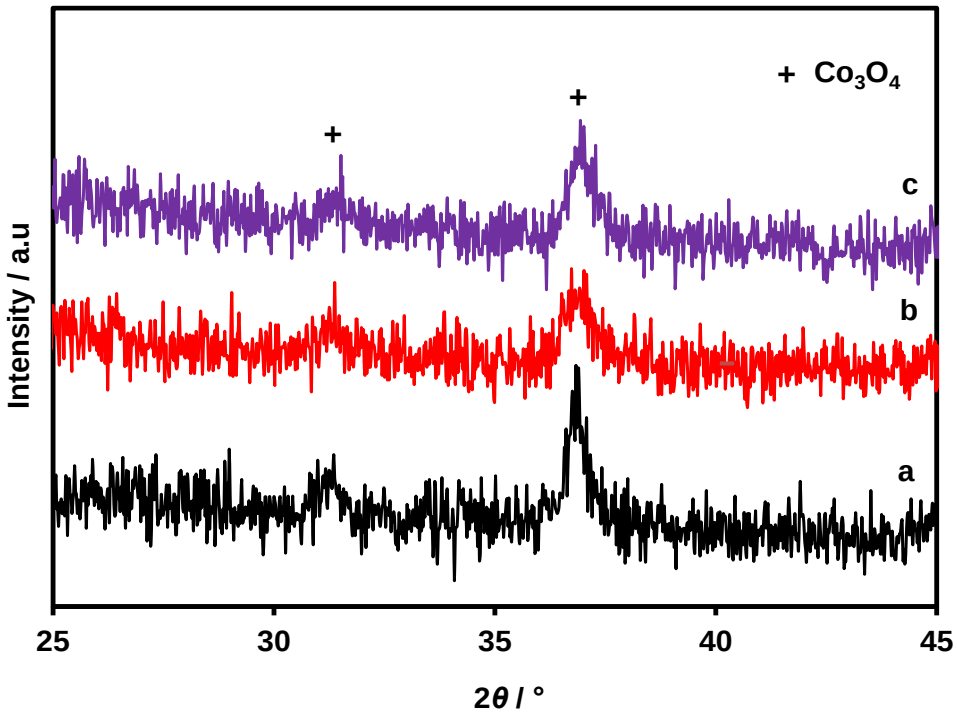


Figure 5. 13. XRD peaks patterns of (a) 10% Co-A/$SiO_{2(IWIM)}$, (b) 10% Co-AA/$SiO_{2(IWIM)}$ and (c) 10% Co-N/$SiO_{2(IWIM)}$ catalysts prepared by the incipient wetness method. (+) – Peak intensity of $Co_3O_4$ at 2θ = 31.6° and 36.8°.

Figs 5.13(a) – (c) show XRD diffraction patterns for the catalyst, the peaks indexed at 2θ = 31.6° and 36.8° indicate $Co_3O_4$ spinel phase as the only oxide of cobalt present [25]. The average $Co_3O_4$ crystallites diameter sizes in and that of metallic cobalt were calculated as

already described [12-14]. These estimated values as well as their related surface area, pore volume and pore width are listed in Table 5.2. It can be seen that the surface area and pore volume of silica support is higher than those of cobalt based catalysts while the surface area of catalyst with higher cobalt content is minimised compared to the catalyst with lower cobalt loading. This trend is probably due to partial filling of silica pores by the added species of cobalt which seems to be more apparent in catalyst with the highest loading [14]. It appears that there is more filling of silica pores by cobalt species of the catalyst prepared by swelling in method which seems to be one of the advantage of this method compared to incipient wetness impregnation technique.

Table 5. 2. XRD and textural data for $Co/SiO_2$ catalyst prepared by impregnation method

| Sample designation | Co content, wt.% | XRD derived Crystallite diameter, nm | | S.A $_{BET,}$ $m^2\ g^{-1}$ | MPV, $cm^3\ g^{-1}$ | TPV, $cm^3\ g^{-1}$ | $P_w$ , Å |
|---|---|---|---|---|---|---|---|
| | | $Co_3O_4$ [a] | $Co^o$ [b] | | | | |
| $SiO_2$ | - | - | - | 182 | 0.07 | 0.09 | 19.8 |
| Co-A/$SiO_{2(IWIM)}$ | 2.5 | 13.0 | 9.8 | 155 | 0.06 | 0.08 | 21.3 |
| | 5 | 22.2 | 16.7 | 154 | 0.06 | 0.08 | 20.8 |
| | 10 | 19.9 | 14.9 | 144 | 0.05 | 0.08 | 22.4 |
| Co-AA/$SiO_{2(IWIM)}$ | 2.5 | 14.2 | 10.6 | 120 | 0.04 | 0.08 | 26.7 |
| | 5 | 16.7 | 12.5 | 107 | 0.04 | 0.08 | 30.0 |
| | 10 | 16.8 | 12.6 | 100 | 0.04 | 0.08 | 32.0 |
| Co-N/$SiO_{2(IWIM)}$ | 2.5 | 16.6 | 12.5 | 145 | 0.06 | 0.08 | 22.1 |
| | 5 | 13.3 | 10.0 | 134 | 0.05 | 0.08 | 24.0 |
| | 10 | 13.8 | 10.4 | 133 | 0.05 | 0.08 | 24.2 |

[a] calculated using Scherrer equation [12, 13]
[b] calculated using d ($Co^o$) = 0.75*d($Co_3O_4$) [14]

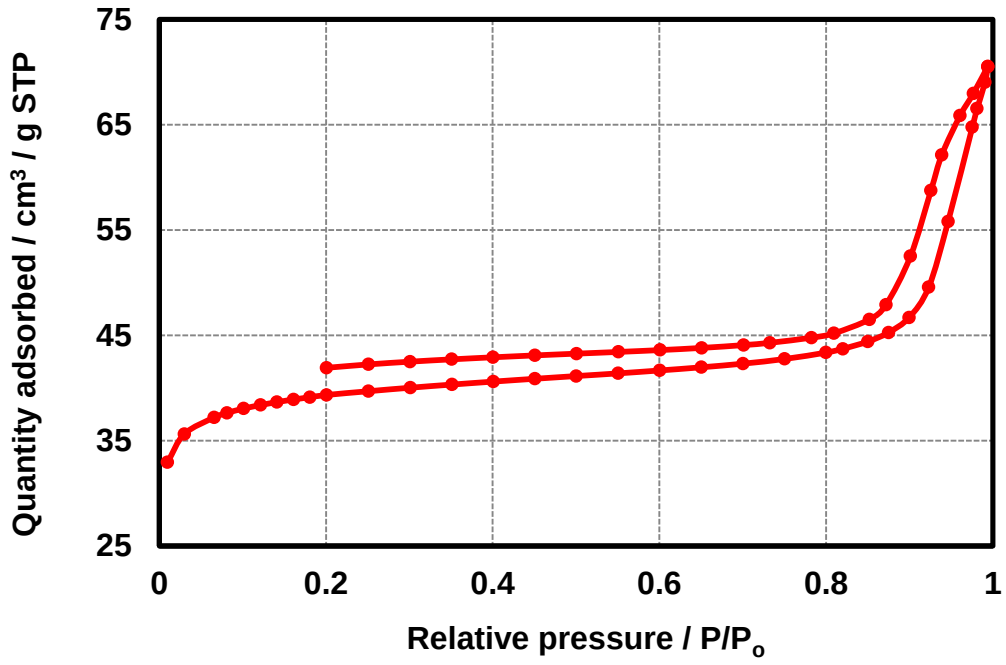


Figure 5. 14. $N_2$ adsorption-desorption isotherm of $Co/SiO_2$ catalyst prepared by the incipient wetness impregnation method.

A typical nitrogen adsorption – desorption isotherm of the catalyst synthesized by incipient wetness method is shown in Fig. 5.14. The related BJH pore size distribution which is typical of catalyst prepared by this method is shown in appendix 8. It can be seen that it is a type II isotherm with an H3 hysteresis loop which is characteristic of materials with aggregates of plate-like particles [19, 20]. The pore size distribution supports the presence of mesopores. The more narrow micropore volume of the catalyst synthesized by incipient wetness method compared to those prepared by the swelling in method (as already shown in Table 5.2 and Table 5.1) is likely responsible for this isotherm demonstrating nitrogen gas update remaining nearly horizontal over a wide range of the relative pressure ($P/P_o$). Based on this isotherm, the t-plot method was used to report pore volume of the catalyst.

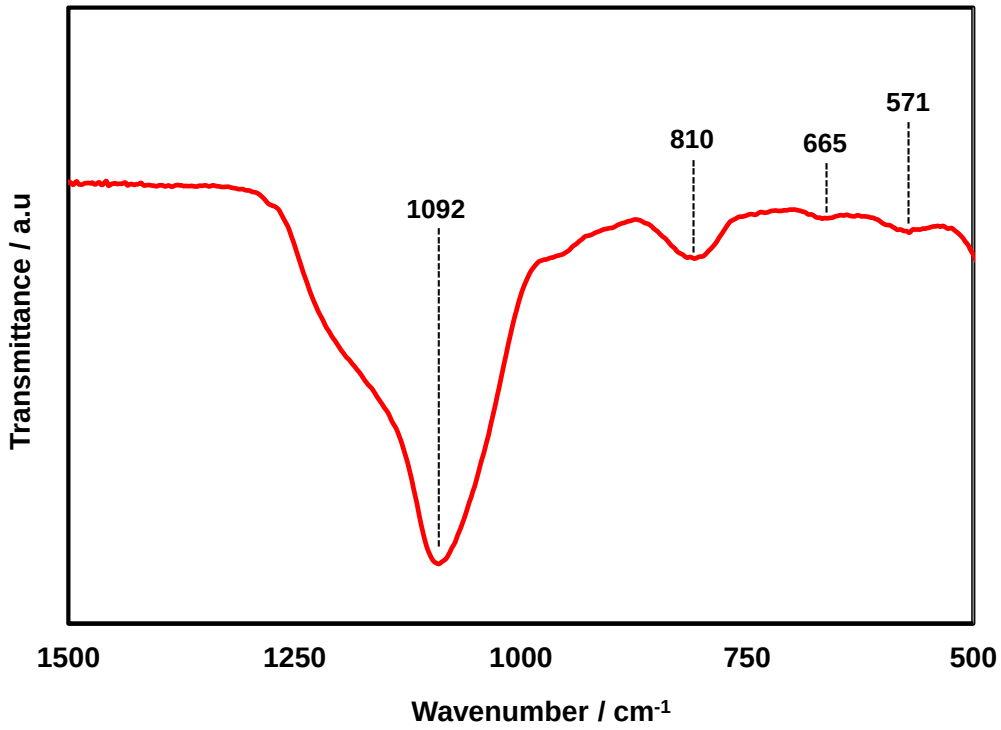


Figure 5. 15. FTIR spectrum of 10% Co-NP/$SiO_{2(SIM)}$ catalyst prepared by the colloidal route coupled with the swelling in method.

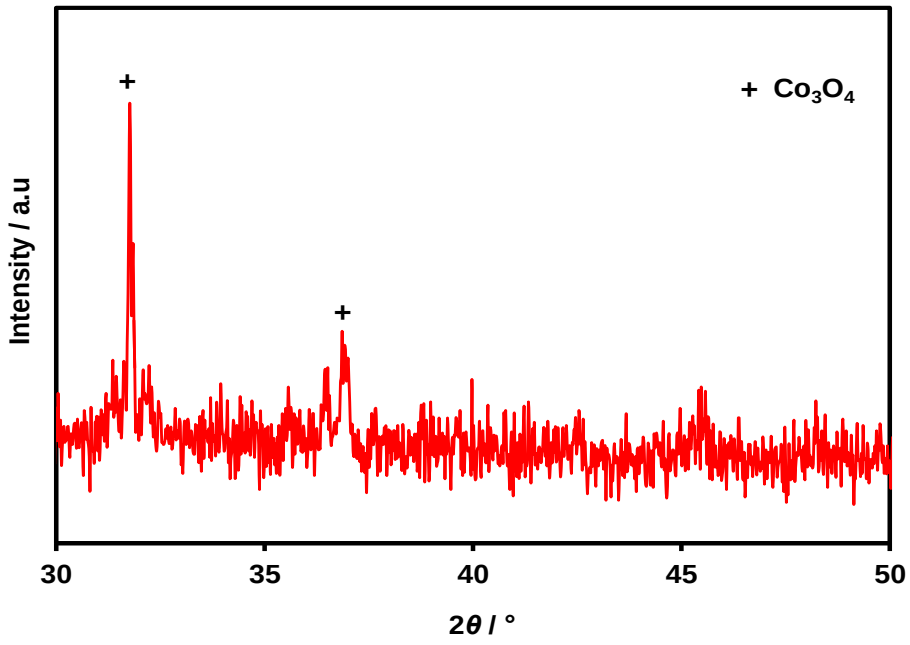


Figure 5. 16. XRD peaks pattern of 10% Co-NP/$SiO_{2(SIM)}$ catalyst prepared by the colloidal route and the swelling in method. (+) – Peak intensity of $Co_3O_4$ at $2\theta = 31.7^{o}$ and 36.9°.

A typical FTIR spectrum of silica-supported cobalt nanoparticles synthesized by colloidal route coupled with the swelling in method is shown in Fig. 5.15. The peaks at 1092cm$^{-1}$ and 810cm$^{-1}$ which can be attributed to asymmetric and symmetric stretching vibration of Si-O-Si bond correspond with formation of $SiO_2$ structure. The narrow bands at 665cm$^{-1}$ and 571cm$^{-1}$ point to vibration of Co(III)-O bond in $Co_3O_4$, these absorption peaks agreed with the catalyst thermal characterisation data. The XRD peaks pattern is shown in Fig. 5.16, $Co_3O_4$ indexed at $2\theta = 31.7°$ and 36.9° was the only detected cobalt containing crystalline phase. The intense peak shown in this XRD peaks pattern is characteristic of nanoparticles.

Table 5. 3. XRD and textural data for Co-NP/$SiO_2$ catalyst prepared by the SIM

| Catalyst designation | Co content, wt.% | XRD derived crystallite diameter, nm | | S.A $_{BET}$, $m^2\ g^{-1}$ | MPV, $cm^3\ g^{-1}$ | TPV, $cm^3\ g^{-1}$ | $P_w$, Å |
|---|---|---|---|---|---|---|---|
| | | $Co_3O_4$ [a] | $Co^o$ [b] | | | | |
| Co-NP/$SiO_{2(SIM)}$ | 2.5 | 16.1 | 12.1 | 166 | 0.05 | 0.09 | 21.7 |
| | 5 | 20.0 | 15.0 | 133 | 0.04 | 0.08 | 24.1 |
| | 10 | 17.0 | 12.7 | 96 | 0.02 | 0.08 | 33.3 |

[a] calculated using Scherrer equation [12, 13]

[b] calculated using $d(Co^o) = 0.75*d(Co_3O_4)$ [14]

The XRD derived particle sizes of $Co_3O_4$, surface area, pore volume and average pore width for this catalyst are listed in Table 5.3. It can be seen that the estimated particles sizes are well within the range of 6-25nm [12-14, 16] which suggest that these values are reasonably close to experimental values [9, 14]. A steady decline in surface area and pore volume of the catalyst can also be observed, this trend points to partial blockage of the silica pores by cobalt species [14].

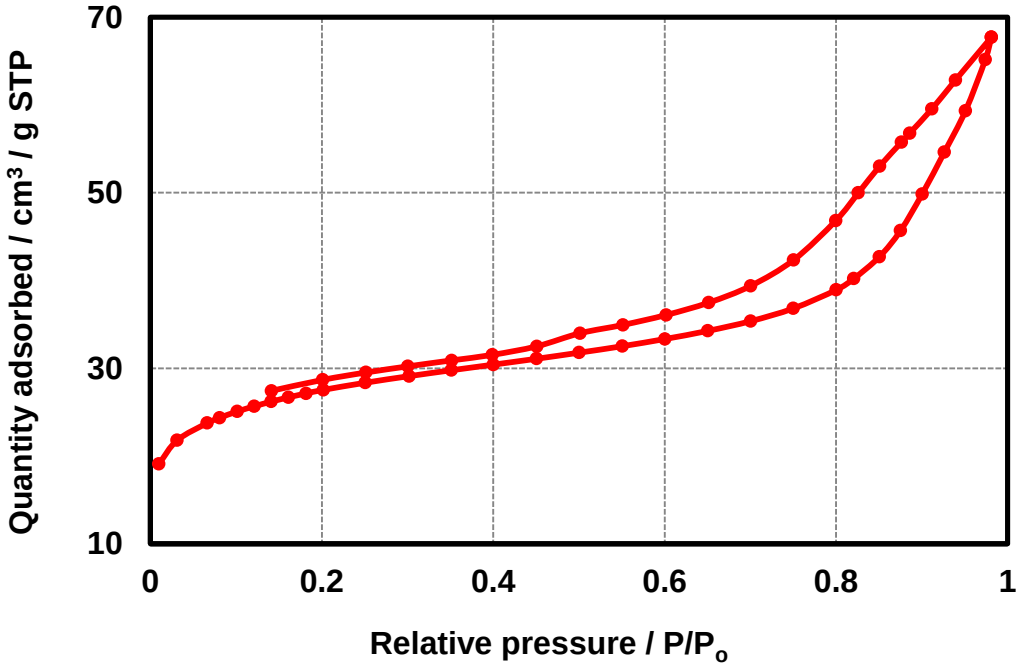


Figure 5. 17. $N_2$ adsorption-desorption isotherm of Co-NP/$SiO_2$ catalyst prepared by the colloidal route coupled with the swelling in method.

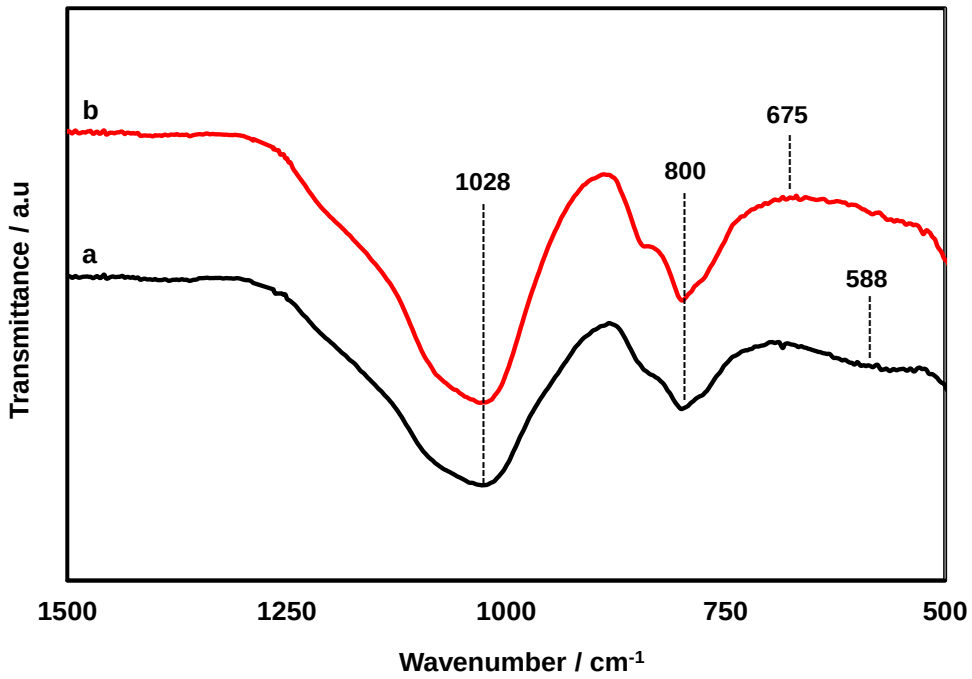


Figure 5. 18. FTIR spectra of silica-supported(a) iron and (b) nickel based catalysts prepared by the swelling in method.

The typical isotherm for silica-supported cobalt nanoparticles catalyst is shown in Fig. 5.17 while its related BJH pore size distribution is shown in appendix 9. It can be seen that it is a type IV isotherm with an H3 hysteresis loop [19, 20].

Figs 5.18 (a) – (b) is a typical spectra of iron and nickel based silica-supported catalysts which were synthesized via the swelling in method. It can be observed that the intense peaks at 1028cm$^{-1}$ and 800cm$^{-1}$ shown in both spectra suggest the presence of silica [7], the narrow and elongated peak centred at 588cm$^{-1}$ indicates vibration of Fe-O bond in $Fe_3O_4$ which is in agreement with literature values [26]. While the hump shape at around 675cm$^{-1}$ could probably suggest the presence of NiO [27]. Fig. 5.19 shows XRD peak of the related silica-supported iron based catalyst.

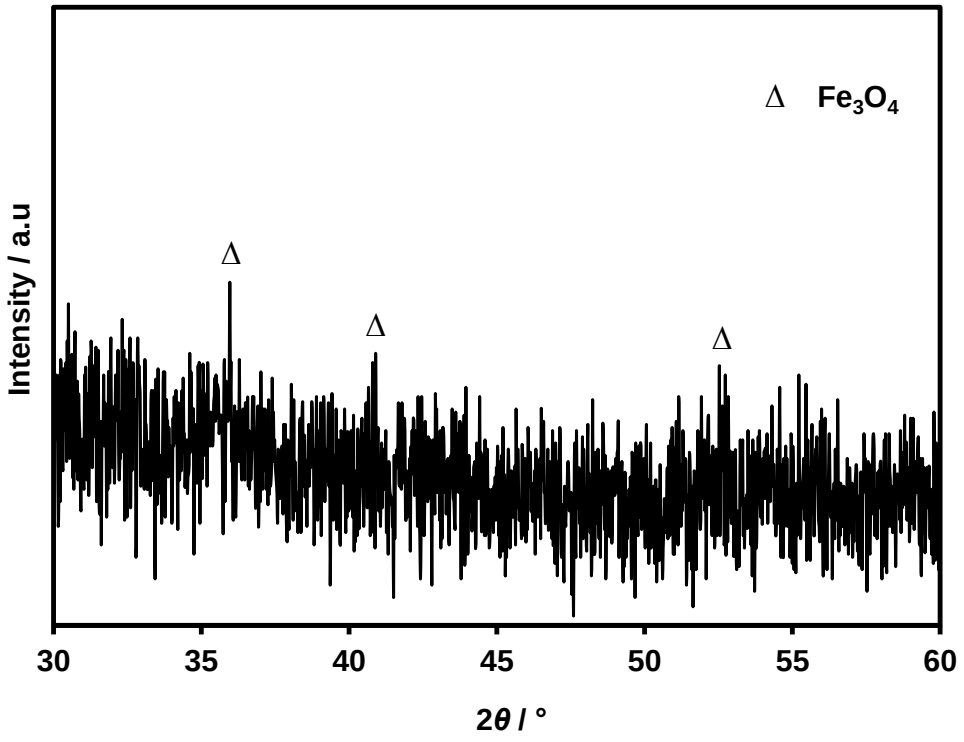


Figure 5. 19. XRD peaks patterns of 10% Fe/$SiO_{2(SIM)}$ catalyst prepared by the novel method. (Δ) – Peak intensity of $Fe_3O_4$ at 2θ = 35.9°, 40.9° and 52.7°.

It can be seen that the peaks of $Fe_3O_4$ indexed at 2θ = 35.9°, 40.9° and 52.7° has very poor intensity and appear almost inseparable from background noise [28]. This observation could be due to destructive interferences by iron oxides [29]. It might also indicate that there is not enough presence of $Fe_3O_4$ crystalline phase formed outside the pores of silica which means that the particles of $Fe_3O_4$ are uniformly locked within the silica frames [30].

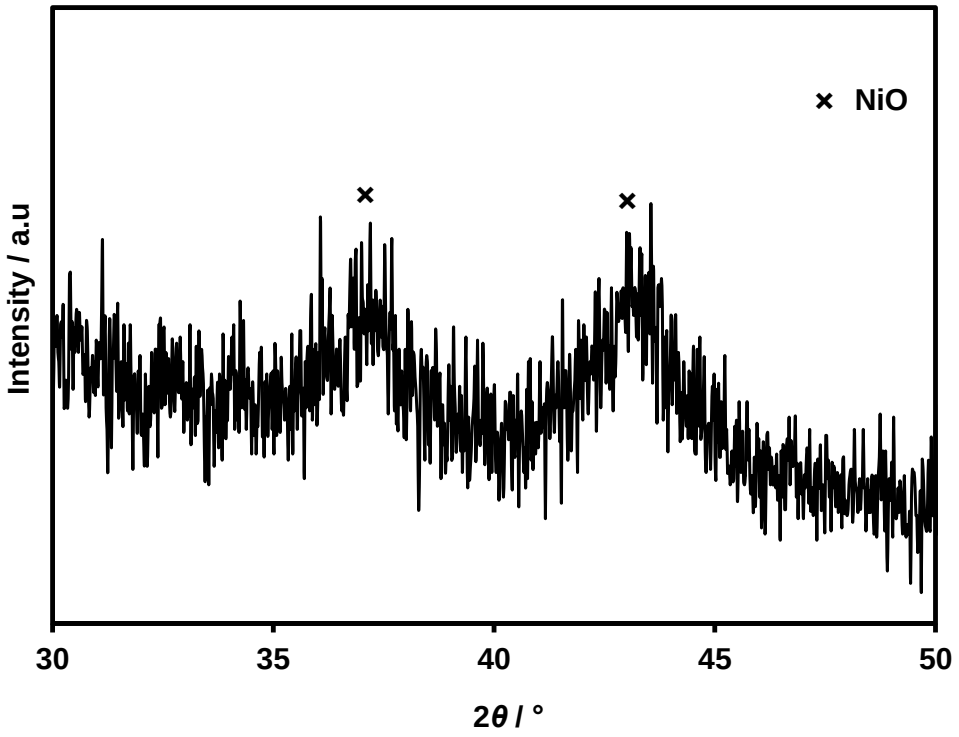


Figure 5. 20. XRD peaks patterns of 10% Ni/$SiO_{2(SIM)}$ catalyst prepared by the swelling in method. (×) – Peak intensity of NiO at 2θ = 36.9° and 43°.

XRD diffraction peaks for Ni/$SiO_{2(SIM)}$ catalyst is shown in Fig. 5.20, the peaks indicated at 2θ = 36.9° and 43° corresponds to NiO [31] which confirms that the hump-like absorption band at 675$cm^{-1}$ found in the spectrum of Ni/$SiO_{2(SIM)}$ catalyst represent oxides of nickel. Table 5.4 contains the surface area, pore volume and average pore width of both (silica-supported nickel and iron based) catalysts. It can be seen that as the amount of iron or nickel

content increases, the surface area and pore volume decreases. This is obviously due to partial filling of silica pores by oxides of iron or nickel [30, 31].

Table 5. 4. The properties of iron and nickel catalysts prepared by the swelling in method

| Samples | Fe/Ni content, wt.% | $S.A_{BET}$, $m^2\ g^{-1}$ | MPV, $cm^3\ g^{-1}$ | TPV, $cm^3\ g^{-1}$ | $P_w$, Å |
|---|---|---|---|---|---|
| $Fe/SiO_{2(SIM)}$ | 2.5 | 521 | 0.13 | 0.28 | 21.5 |
| | 5 | 517 | 0.13 | 0.26 | 20.1 |
| | 10 | 511 | 0.08 | 0.25 | 19.6 |
| $Ni/SiO_{2(SIM)}$ | 2.5 | 580 | 0.11 | 0.31 | 21.4 |
| | 5 | 382 | 0.10 | 0.20 | 20.9 |
| | 10 | 380 | 0.09 | 0.19 | 20.0 |

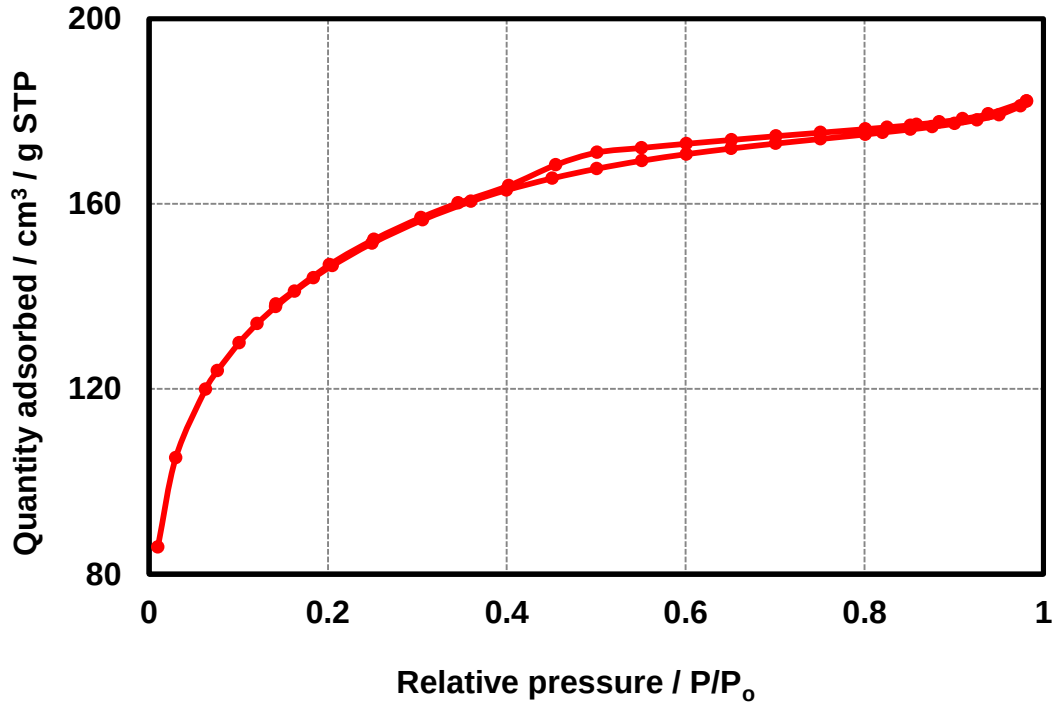


Figure 5. 21. $N_2$ adsorption-desorption isotherm of silica-supported iron catalyst prepared by the swelling in method.

Typical isotherms for silica-supported iron and nickel based catalysts prepared using the swelling in method can be seen in Figs. 5.21 and 5.22 while their related BJH pore size distribution are shown in appendixes 10 and 11.

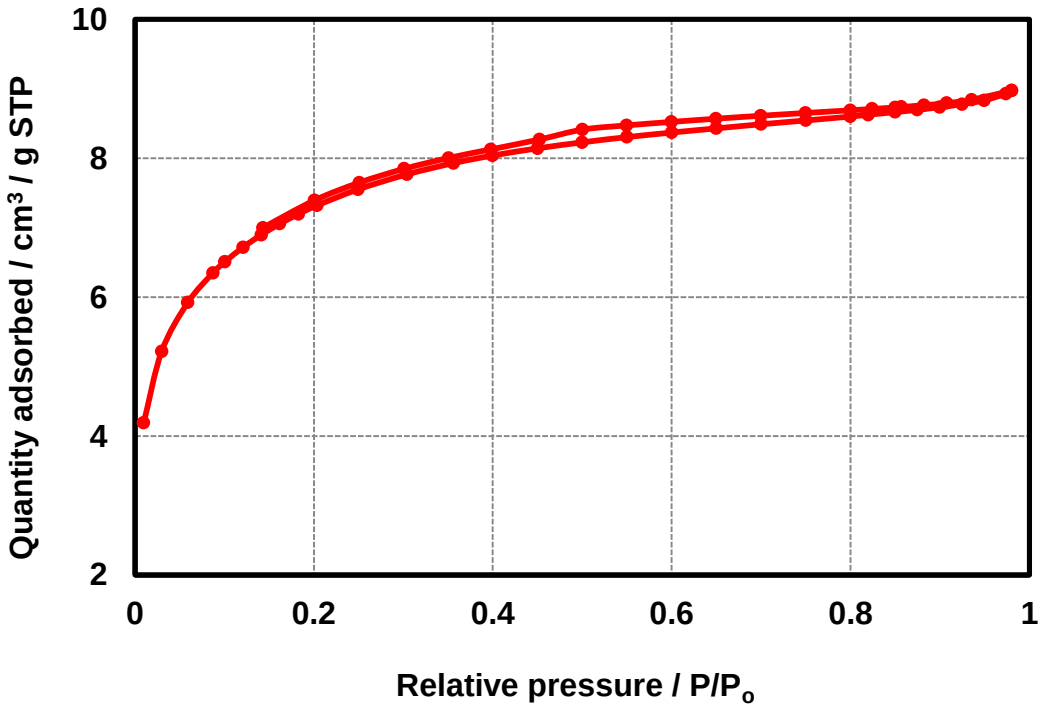


Figure 5. 22. $N_2$ adsorption-desorption isotherm of silica-supported nickel catalyst prepared by the swelling in method.

Both isotherms are pseudo type I isotherm (as the plateau is basically due to micropores filling and not monolayer limit), it indicates that the material is microporous while it also has an H4 hysteresis loop which suggest the presence of some mesopores with particles that are assembled in a coherently loosed manner [19, 20]. The related BJH pore size distributions indicate the presence of mesopores in the catalyst materials.

## 5.2. Conclusions

The results acquired from oxidative thermal decomposition of PDMS supported cobalt, iron and nickel based catalysts prepared by the swelling in method showed that the polymeric support (PDMS) converted to porous silica. However, when a separate batch of PDMS supported cobalt based catalyst was calcined under vacuum in the presence of nitrogen; it was found that PDMS still retained its polymeric form. The data obtained from FTIR and XRD confirmed the thermal characterisation results. The trends displayed by the surface area and pore volume of catalyst synthesized by the swelling in method as percentage loading of the different metals increased showed that oxides of the metals are present inside the silica pores. The same observation was seen by silica-supported cobalt based catalyst prepared by incipient wetness impregnation method. Meanwhile, nitrogen adsorption – desorption showed that all the catalysts prepared by the swelling in method had much improved surface area and pore volume compared to the catalysts prepared by incipient wetness impregnation method. The estimated values obtained for XRD particles sizes of all synthesized silica-supported cobalt based catalyst using both the swelling in and incipient wetness impregnation methods has previously been demonstrated to be in good agreement with experimental values. The isotherms, hysteresis loops and pore size distribution of all the catalyst showed that they are both microporous and mesoporous with particles that are assembled in a coherently loosed manner.

**References**

1. Luo, R.; Cho, I.S.; Feng, Y.; Cai, L.; Rao, P.M.; Zheng, X. Morphological control of heterostructured nanowires synthesized by sol-flame method. *Nanoscale research letters*. **2013**, 8, 1.
2. Girardon, J.-S.; Lermontov, A.S.; Gengembre, L.; Chernavskii, P.A.; Griboval-Constant, A.; Khodakov, A.Y. Effect of cobalt precursor and pretreatment conditions on the structure and catalytic performance of cobalt silica-supported Fischer–Tropsch catalysts. *Journal of Catalysis*. **2005**, 230, 339.
3. Camino, G.; Lomakin, S.M.; Lageard, M. Thermal polydimethylsiloxane degradation. Part 2. The degradation mechanisms. *Polymer*. **2002**, 43, 2011.
4. Jana, R.N.; Mukunda, P.G.; Nando, G.B. Thermogravimetric analysis of compatibilized blends of low density polyethylene and poly(dimethyl siloxane) rubber. *Polymer Degradation and Stability*. **2003**, 80, 75.
5. Cseri, T.; Békássy, S.; Kenessey, G.; Liptay, G.; Figueras, F. Characterization of metal nitrates and clay supported metal nitrates by thermal analysis. *Thermochimica Acta*. **1996**, 288, 137.
6. Ehrhardt, C.; Gjikaj, M.; Brockner, W. Thermal decomposition of cobalt nitrato compounds: Preparation of anhydrous cobalt(II)nitrate and its characterisation by Infrared and Raman spectra. *Thermochimica Acta*. **2005**, 432, 36.
7. Jahangiri, H.; Bennett, J.; Mahjoubi, P.; Wilson, K.; Gu, S. A review of advanced catalyst development for Fischer-Tropsch synthesis of hydrocarbons from biomass derived syn-gas. *Catalysis Science & Technology*. **2014**, 4, 2210.
8. Han, Y.; Zhang, J.; Shi, L.; Qi, S.; Cheng, J.; Jin, R. Improvement of thermal resistance of polydimethylsiloxanes with polymethylmethoxysiloxane as crosslinker. *Polymer degradation and stability*. **2008**, 93, 242.

9. Fouad, O.A.; Maklouf, S.A.; Ali, G.A.M.; El-Sayed, A.Y. Cobalt/silica nanocomposite via thermal calcination-reduction of gel precursors. *Materials Chemistry and Physics*. **2011**, 128, 70.

10. Jung, J.-S.; Kim, S.W.; Moon, D.J. Fischer–Tropsch Synthesis over cobalt based catalyst supported on different mesoporous silica. *Catalysis Today*. **2012**, 185, 168.

11. Khodakov, A.Y.; Zholobenko, V.L.; Bechara, R.; Durand, D. Impact of aqueous impregnation on the long-range ordering and mesoporous structure of cobalt containing MCM-41 and SBA-15 materials. *Microporous and Mesoporous Materials.* **2005**, 79, 29.

12. Schanke, D.; Vada, S.; Blekkan, E.A.; Hilmen, A.M.; Hoff, A.; Holmen, A. Study of Pt-promoted cobalt CO hydrogenation catalysts. *Journal of Catalysis*. **1995**, 156, 85.

13. Khodakov, A.Y.; Griboval-Constant, A.; Bechara, R.; Zholobenko, V.L. Pore size effects in Fischer-Tropsch synthesis over cobalt-supported mesoporous silicas. *Journal of Catalysis*. **2002**, 206, 230.

14. Venezia, A.M.; La Parola, V.; Liotta, L.F.; Pantaleo, G.; Lualdi, M.; Boutonnet, M.; Järås, S. $Co/SiO_2$ catalysts for Fischer–Tropsch synthesis; effect of Co loading and support modification by $TiO_2$. *Catalysis Today*. **2012**, 197, 18.

15. Shi, L.; Jin, Y.; Xing, C.; Zeng, C.; Kawabata, T.; Imai, K.; Matsuda, K.; Tan, Y.; Tsubaki, N. Studies on surface impregnation combustion method to prepare supported $Co/SiO_2$ catalysts and its application for Fischer–Tropsch synthesis. *Applied Catalysis A: General*. **2012**, 435, 217.

16. Khodakov, A.Y.; Chu, W.; Fongarland, P. Advances in the development of novel cobalt Fischer-Tropsch catalysts for synthesis of long-chain hydrocarbons and clean fuels. *Chemical Reviews*. **2007**, 107, 1692.

17. Xiong, H.; Zhang, Y.; Liew, K.; Li, J. Ruthenium promotion of Co/SBA-15 catalysts with high cobalt loading for Fischer–Tropsch synthesis. *Fuel Processing Technology*. **2009**, 90, 237.

18. Panpranot, J.; Kaewkun, S.; Praserthdam, P.; Goodwin, Jr. J.G. Effect of cobalt precursors on the dispersion of cobalt on MCM-41. *Catalysis letters*. **2003**, 91, 95.

19. Sing, K.S. Reporting physisorption data for gas/solid systems with special reference to the determination of surface area and porosity (Recommendations 1984). *Pure and applied chemistry*. **1985**, 57, 603.

20. Neimark, A.V.; Sing, K.S.; Thommes, M. Surface area and porosity. *Handbook of Heterogeneous Catalysis*. **2008**, 129.

21. Zhao, H.-X.; Chen, J.-G.; Sun, Y.-H. Effect of impregnation pH on the catalytic performance of Co/ZrO2 catalyst in Fischer-Tropsch synthesis. *Studies in surface science and catalysis*. **2004**, 147, 355.

22. Khodakov, A.Y.; Lynch, J.; Bazin, D.; Rebours, B.; Zanier, N.; Moisson, B.; Chaumette, P. Reducibility of Cobalt Species in Silica-Supported Fischer–Tropsch Catalysts. *Journal of Catalysis*. **1997**, 168, 16.

23. Lefez, B.; Nkeng, P.; Lopitaux, J.; Poillerat, G. Characterization of cobaltite spinels by reflectance spectroscopy. *Materials research bulletin*. **1996**, 31, 1263.

24. Lin, H.-K.; Chiu, H.-C.; Tsai, H.-C.; Chien, S.-H.; Wang, C.-B. Synthesis, characterization and catalytic oxidation of carbon monoxide over cobalt oxide. *Catalysis letters*. **2003**, 88, 169.

25. Soled, S.L.; Iglesia, E.; Fiato, R.A.; Baumgartner, J.E.; Vroman, H.; Miseo, S. Control of metal dispersion and structure by changes in the solid-state chemistry of supported cobalt Fischer–Tropsch catalysts. *Topics in catalysis*. **2003**, 26, 101.

26. Chen, L.; Lin, Z.; Zhao, C.; Zheng, Y.; Zhou, Y.; Peng, H. Direct synthesis and characterization of mesoporous $Fe_3O_4$ through pyrolysis of ferric nitrate-ethylene glycol gel. *Journal of Alloys and Compounds*. **2011**, 509, L1.

27. Infantes-Molina, A.; Mérida-Robles, J.; Braos-García, P.; Rodŕiguez-Castellón, E.; Finocchio, E.; Busca, G.; Maireles-Torres, P.; Jiménez-López, A. Nickel supported on porous silica as catalysts for the gas-phase hydrogenation of acetonitrile. *Journal of Catalysis*. **2004**, 225, 479.

28. Sharma, G.; Jeevanandam, P. Synthesis of self-assembled prismatic iron oxide nanoparticles by a novel thermal decomposition route. *RSC Advances*. **2013**, 3, 189.

29. Martinez, F., et al. Synthesis and characterisation of iron-containing SBA-15 mesoporous silica. *Studies in Surface Science and Catalysis*. **2002**, 142, 1109.

30. Liu, C.-Y.; Chen, C.-F.; Leu, J.J.; Lin, Y.-C. Iron oxide nanoparticles within the pore system of mesoporous SBA-15 in different acidity: the synthesis and characterization. *Journal of sol-gel science and technology*. **2007**, 43, 47.

31. Zhang, T.; Amiridis, M.D. Hydrogen production via the direct cracking of methane over silica-supported nickel catalysts. *Applied Catalysis A: General*. **1998**, 167, 161.

# CHAPTER 6

# Catalytic performance in FT synthesis

This chapter covers results and discussion on catalytic performance of all the synthesized catalysts in Fischer-Tropsch synthesis reaction. The rate of CO conversion and ratio of methane formation to CO converted were the two parameters considered for discussion. Here, the effect of preparation method, temperature and time on stream, percentage content of cobalt, impact of cobalt precursor as well as the influence of ruthenium as a promoter on the catalytic activity were discussed.

## 6.1. Results and discussion

The catalytic performance in Fischer-Tropsch synthesis of all the catalysts studied in this work was carried under the reaction conditions as already covered in chapter 3. Here, CO conversion and the ratio of methane formed to CO converted are outlined while the effect of preparation method, temperature and time on stream, and impact of cobalt precursor would be discussed. The effect of the presence of ruthenium on the catalytic behaviour of some of the catalyst was also outlined and discussed.

### 6.1.1. Effect of temperature, method of synthesis and cobalt content on catalyst performance

To outline and discuss the overall catalytic performance of the prepared catalyst, Tables 6.1 and 6.2 show CO conversions and the corresponding ratios of methane formed to CO converted as a function of temperature and time for 2.5 and 5 w/w % $Co/SiO_2$ catalyst while Table 6.3 show CO conversions and the corresponding ratios of methane formed to CO converted as a function of temperature and time for 10 w/w % $Co/SiO_2$ and Co/PDMS catalyst which were prepared by two different methods using cobalt acetate, acetylacetonate and nitrate as precursor. Specifically, $Co\text{-}A/SiO_{2(SIM)}$, $Co\text{-}AA/SiO_{2(SIM)}$ and $Co\text{-}N/SiO_{2(SIM)}$ catalyst was prepared by the swelling in method, $Co\text{-}A/PDMS_{(SIM)}$, $Co\text{-}AA/PDMS_{(SIM)}$ and 10% $Co\text{-}N/PDMS_{(SIM)}$ catalyst was prepared by the swelling in method but calcined under the flow of nitrogen in vacuum while $Co\text{-}A/SiO_{2(IWIM)}$, $Co\text{-}AA/SiO_{2(IWIM)}$ and $Co\text{-}N/SiO_{2(IWIM)}$ catalyst was prepared by the incipient wetness impregnation method.

Table 6. 1. CO conversions and ratios of methane formed to CO converted as a function of temperature for 2.5 w/w % $Co/SiO_{2(SIM)}$ and $Co/SiO_{2(IWIM)}$ catalyst prepared by the swelling in and incipient wetness impregnation methods

| Catalyst | Temp / °C | CO conversion / % after 20 mins on stream [a] | Ratio of $CH_4$ formed to CO converted after 20 mins on stream [a] |
|---|---|---|---|
| $Co\text{-}A/SiO_{2(SIM)}$ | 350 | 23.9 | 0.1 |
| | 450 | 9.3 | 0.3 |
| | 550 | 0.6 | 1.0 |
| $Co\text{-}A/SiO_{2(IWIM)}$ | 350 | 15.5 | 0.4 |
| | 450 | 23.1 | 0.3 |
| | 550 | 32.5 | 0.3 |
| $Co\text{-}AA/SiO_{2(SIM)}$ | 350 | 35.1 | 0.2 |
| | 450 | 45.3 | 0.1 |
| | 550 | 34.6 | 0.1 |
| $Co\text{-}AA/SiO_{2(IWIM)}$ | 350 | 11.5 | 0.5 |
| | 450 | 29.1 | 0.3 |
| | 550 | 29.1 | 0.2 |
| $Co\text{-}N/SiO_{2(SIM)}$ | 350 | 40.4 | 0.6 |
| | 450 | 30.1 | 0.7 |
| | 550 | 14.2 | 1.0 |
| $Co\text{-}N/SiO_{2(IWIM)}$ | 350 | 4.4 | 0.6 |
| | 450 | 8.8 | 0.3 |
| | 550 | 19.3 | 0.2 |

Reaction conditions: Pressure = 1bar, $H_2/CO = 4$. Co-A = Decomposed cobalt acetate. Co-AA = decomposed cobalt acetylacetonate. Co-N = decomposed cobalt nitrate.

[a] These conversion values were measured once but based on their variabilities, an estimate of the 95% confidence limit on these values for CO conversion is typically ±15% and on the ratio of $CH_4$ to CO is typically ±0.1.

Table 6. 2. CO conversions and ratios of methane formed to CO converted as a function of temperature and time-on-stream for 5 w/w % $Co/SiO_{2(SIM)}$ and $Co/SiO_{2(IWIM)}$ catalyst prepared by the methods as shown for Table 6.1

| Catalyst | Temp / °C | CO conversion / % with time on stream [a] | | Ratio $CH_4$ formed to CO converted with time on stream [a] | |
|---|---|---|---|---|---|
| | | 20mins | 60mins | 20mins | 60mins |
| $Co\text{-}A/SiO_{2(SIM)}$ | 350 | 80.7 | 72.8 | 0.1 | 0.1 |
| | 450 | 72.8 | 76.4 | 0.1 | 0.1 |
| | 550 | 74.9 | 10.6 | 0.1 | 0.5 |
| $Co\text{-}A/SiO_{2(IWIM)}$ | 350 | 64.1 | 38.0 | 0.2 | 0.1 |
| | 450 | 35.6 | 33.3 | 0.3 | 0.4 |
| | 550 | 6.3 | 2.6 | 0.7 | 1.0 |
| $Co\text{-}AA/SiO_{2(SIM)}$ | 350 | 80.5 | 78.3 | 0.1 | 0.1 |
| | 450 | 71.3 | 55.7 | 0.1 | 0.1 |
| | 550 | 61.2 | 13.9 | 0.1 | 0.4 |
| $Co\text{-}AA/SiO_{2(IWIM)}$ | 350 | 83.5 | 68.3 | 0.1 | 0.1 |
| | 450 | 71.4 | 71.8 | 0.2 | 0.2 |
| | 550 | 77.3 | 10.0 | 0.1 | 0.5 |
| $Co\text{-}N/SiO_{2(SIM)}$ | 350 | 55.5 | 22.2 | 0.1 | 0.2 |
| | 450 | 37.9 | 38.7 | 0.2 | 0.2 |
| | 550 | 13.8 | 11.5 | 0.3 | 0.4 |
| $Co\text{-}N/SiO_{2(IWIM)}$ | 350 | 19.9 | 16.7 | 0.2 | 0.2 |
| | 450 | 13.3 | 10.1 | 0.4 | 0.6 |
| | 550 | 10.1 | 6.1 | 0.5 | 0.8 |

Reaction conditions: As shown for Table 6.1.

Co-A, Co-AA and CO-N = As shown for Table 6.1.

[a] These conversion values were measured once but based on their variabilities, an estimate of the 95% confidence limit on these values for CO conversion is typically ±20% and on the ratio of $CH_4$ to CO is typically ±0.1.

Table 6. 3. CO conversions and ratios of methane formed to CO converted as a function of temperature and time-on-stream for 10 w/w % $Co/SiO_{2(SIM)}$, $Co/SiO_{2(IWIM)}$ and $Co/PDMS_{(SIM)}$ catalyst prepared by the methods as shown for Table 6.1

| Catalyst | Temp / °C | CO conversion / % with time on stream [a] | | Ratio $CH_4$ formed to CO converted with time on stream [a] | |
|---|---|---|---|---|---|
| | | 20mins | 60mins | 20mins | 60mins |
| $Co\text{-}A/SiO_{2(SIM)}$ | 350 | 16.7 | 21.2 | 0.2 | 0.2 |
| | 450 | 42.4 | 39.3 | 0.2 | 0.2 |
| | 550 | 36.3 | 40.1 | 0.1 | 0.1 |
| $Co\text{-}A/SiO_{2(IWIM)}$ | 350 | 50.8 | 42.1 | 0.5 | 0.5 |
| | 450 | 50.2 | 48.1 | 0.4 | 0.5 |
| | 550 | 23.4 | 17.6 | 0.5 | 0.6 |
| $Co\text{-}A/PDMS_{(SIM)}$ | 350 | 20.1 | 14.6 | 0.3 | 0.4 |
| | 450 | 17.9 | 19.6 | 0.4 | 0.4 |
| | 550 | 14.3 | 18.2 | 0.7 | 0.5 |
| $Co\text{-}AA/SiO_{2(SIM)}$ | 350 | 20.2 | 14.1 | 0.1 | 0.3 |
| | 450 | 16.5 | 13.7 | 0.2 | 0.5 |
| | 550 | 17.2 | 10.4 | 0.2 | 0.7 |
| $Co\text{-}AA/SiO_{2(IWIM)}$ | 350 | 85.1 | 78.5 | 0.1 | 0.1 |
| | 450 | 75.1 | 74.9 | 0.2 | 0.2 |
| | 550 | 55.9 | 36.1 | 0.2 | 0.2 |
| $Co\text{-}AA/PDMS_{(SIM)}$ | 350 | 1.2 | 5.8 | 1.0 | 0.5 |
| | 450 | 11.1 | 11.2 | 0.3 | 0.3 |
| | 550 | 11.7 | 14.8 | 0.3 | 0.2 |
| $Co\text{-}N/SiO_{2(SIM)}$ | 350 | 73.3 | 78.9 | 0.1 | 0.1 |
| | 450 | 81.6 | 82.8 | 0.1 | 0.1 |
| | 550 | 36.6 | 30.8 | 0.1 | 0.2 |
| $Co\text{-}N/SiO_{2(IWIM)}$ | 350 | 41.5 | 34.1 | 0.2 | 0.2 |
| | 450 | 49.1 | 40.1 | 0.2 | 0.3 |
| | 550 | 39.1 | 17.2 | 0.1 | 0.4 |
| $Co\text{-}N/PDMS_{(SIM)}$ | 350 | 19.6 | 19.3 | 0.2 | 0.2 |
| | 450 | 20.6 | 21.1 | 0.2 | 0.2 |
| | 550 | 20.4 | 23.1 | 0.2 | 0.2 |

Reaction conditions: As shown for Table 6.1. Co-A, Co-AA and Co-N = As shown for Table 6.1

[a] The 95% confidence limit was estimated to typically be ±20% and ±0.1 respectively.

It can be seen in Table 6.1 that at 2.5 w/w % cobalt content, Co-AA/$SiO_{2(SIM)}$ and Co-N/$SiO_{2(SIM)}$ catalyst are the most active while Co-N/$SiO_{2(IWIM)}$ has the least catalytic activity. The best catalytic behaviour of the two catalysts can be attributed to the method of preparation which could have encouraged better dispersion and reducibility. Although, methane generated by Co-N/$SiO_{2(SIM)}$ catalyst is relatively high; its catalytic performance seems not to drop because of possible carbon deposition from disproportionation of carbon monoxide that produced the excess methane. The poor catalytic behaviour of Co-N/$SiO_{2(IWIM)}$ catalyst is likely due to the preparation method with the use of cobalt nitrate as precursor, this seems to cause poor reducibility of $Co^{2+}$ and $Co^{3+}$ species and inhibition of Fischer-Tropsch reaction [1, 2]. Meanwhile, it is well established [3-6] that the representative Fischer-Tropsch reaction temperature range chosen to study these catalysts would readily encourage formation of methane and catalyst deactivation by sintering. Previous reports has also shown that continuous formation of hydrocarbons such as methane leads to poisoning of cobalt active sites by carbon deposition during FTS [7-9] and it can be seen that the catalytic activity of Co-A/$SiO_{2(SIM)}$ catalyst agrees with this.

In Table 6.2, it can be seen that Co-A/$SiO_{2(SIM)}$, Co-AA/$SiO_{2(SIM)}$ and Co-A/$SiO_{2(IWIM)}$ catalysts have the best catalytic activity with Co-A/$SiO_{2(IWIM)}$ catalyst generating more methane while Co-N/$SiO_{2(IWIM)}$ catalyst has the least catalytic activity. The catalytic behaviour shown by the best catalysts suggest the availability of more cobalt active sites, without much suffering from possible sintering effect, as temperature increases with time on stream. The amount of methane generated by Co-A/$SiO_{2(IWIM)}$ catalyst is likely due to its method of preparation as most of the active catalyst synthesized by the incipient wetness impregnation tends to produce more methane than the catalyst prepared by the swelling in method. The poor catalytic activity of Co-N/$SiO_{2(IWIM)}$ catalyst can be due to the method of

preparation with the use of cobalt nitrate as precursor. Meanwhile, the effect of cobalt precursor on catalytic performance will be covered in subsequent section.

In Table 6.3, it can be seen that Co-AA/$SiO_{2(IWIM)}$ and Co-N/$SiO_{2(SIM)}$ are the most active catalysts with the catalyst prepared by the incipient wetness impregnation method producing more methane. Co-AA/$PDMS_{(SIM)}$ catalyst has the least catalytic activity. The catalytic behaviour of the best catalysts is attributed to less sintering of their active sites. The higher amount of methane generated by Co-AA/$SiO_{2(IWIM)}$ is likely due to its method of preparation. The poor catalytic activity observed for PDMS supported cobalt catalyst is most likely due to the presence of excessive amount of carbon in the polymeric support which could be blocking active sites of the catalyst [2].

In considering the effect of cobalt content (w/w %) on catalytic activity of the catalysts prepared by both methods, it can be seen overall that 2.5 and 5% catalyst synthesized by the swelling in method are more active (with 5 w/w % being the most active) than the catalyst prepared by the incipient wetness impregnation method while 10% catalyst prepared by the incipient wetness impregnation technique is slightly more active than the catalyst synthesized by the swelling in method. Meanwhile, it is important at this point to mention that the catalytic behaviour displayed by most of the catalysts already discussed, showed that CO conversion is inversely dependent on the amount of methane formed which is in agreement with previous reports [7-9]. In addition, it has been reported [7, 9, 10] that silica-supported cobalt catalyst which produces smaller amount of light chain hydrocarbon product like methane (an unfavourable FT product) is usually more selective towards $C_{5+}$ hydrocarbons and it can be seen overall from all the data discussed so far, that silica-supported cobalt based catalyst prepared by the swelling in method generated less methane when compared to those prepared by the incipient wetness impregnation technique.

Table 6. 4. CO conversions and ratios of methane formed to CO converted as a function of temperature and time-on-stream for Co-NP/$SiO_{2(SIM)}$ catalyst prepared by the swelling in and colloidal techniques

| Catalyst | Temp / °C | CO conversion / % with time on stream [a] | | Ratio $CH_4$ formed to CO converted with time on stream [a] | |
|---|---|---|---|---|---|
| | | 20mins | 60mins | 20mins | 60mins |
| 2.5% Co-NP/$SiO_{2(SIM)}$ | 350 | 89.1 | 63.9 | 0.1 | 0.04 |
| | 450 | 48.2 | 40.1 | 0.04 | 0.1 |
| | 550 | 33.5 | 14.5 | 0.1 | 0.1 |
| 5% Co-NP/$SiO_{2(SIM)}$ | 350 | 94.9 | 78.5 | 0.1 | 0.02 |
| | 450 | 67.4 | 62.8 | 0.03 | 0.04 |
| | 550 | 54.5 | 35.5 | 0.1 | 0.04 |
| 10% Co-NP/$SiO_{2(SIM)}$ | 350 | 67.4 | 48.0 | 0.1 | 0.04 |
| | 450 | 36.1 | 24.3 | 0.1 | 0.1 |
| | 550 | 12.0 | 2.7 | 0.2 | 0.7 |

Reaction conditions: As shown for Table 6.1. Co-NP = cobalt nanoparticles

[a] The estimated 95% confidence limit on these values for CO conversion is typically ±20% and on the ratio of $CH_4$ to CO is typically ±0.1.

Table 6.4 shows catalytic performance of 2.5, 5 and 10 w/w % silica-supported Co-NP catalyst using cobalt chloride as precursor which was prepared by the colloidal and swelling in method. It can be seen that these catalysts are reasonably active with 5% Co-NP/$SiO_{2(SIM)}$ as the best catalyst. This catalytic behaviour is probably due to the colloidal method of preparation which has been extensively reported [11-15] to encourage even distribution of cobalt particle sizes. In the absence of 10% Co-NP/$SiO_{2(SIM)}$ catalyst, it is interesting to see that the catalyst prepared by this method generally produced the lowest amount of methane compared to other silica-supported cobalt based catalysts studied in this thesis.

Table 6. 5. CO conversions and ratios of methane formed to CO converted as a function of temperature and time-on-stream for silica-supported iron and nickel catalyst prepared by the swelling in method.

| Catalyst | Temp / °C | CO conversion / % with time on stream [a] | | Ratio $CH_4$ formed to CO converted with time on stream [a] | |
|---|---|---|---|---|---|
| | | 20mins | 60mins | 20mins | 60mins |
| 2.5% $Fe/SiO_{2(SIM)}$ | 350 | 65.7 | 60.1 | 0.1 | 0.04 |
| | 450 | 51.9 | 77.7 | 0.1 | 0.03 |
| | 550 | 67.2 | 72.2 | 0.04 | 0.1 |
| 5% $Fe/SiO_{2(SIM)}$ | 350 | 42.7 | 17.3 | 0.04 | 0.1 |
| | 450 | 9.3 | 1.7 | 0.2 | 1.0 |
| | 550 | 3.4 | 4.2 | 0.8 | 0.7 |
| 10% $Fe/SiO_{2(SIM)}$ | 350 | 81.1 | 57.8 | 0.04 | 0.03 |
| | 450 | 48.2 | 25.2 | 0.1 | 0.1 |
| | 550 | 9.4 | 5.4 | 0.2 | 0.2 |
| 2.5% $Ni/SiO_{2(SIM)}$ | 350 | 70.7 | 54.6 | 0.2 | 0.3 |
| | 450 | 24.8 | 20.1 | 0.1 | 1.0 |
| | 550 | 21.2 | 17.8 | 1.0 | 1.0 |
| 5% $Ni/SiO_{2(SIM)}$ | 350 | 77.5 | 55.6 | 0.1 | 0.1 |
| | 450 | 76.0 | 61.4 | 0.3 | 0.3 |
| | 550 | 56.0 | 59.9 | 0.4 | 0.3 |
| 10% $Ni/SiO_{2(SIM)}$ | 350 | 53.9 | 21.8 | 0.1 | 0.2 |
| | 450 | 30.0 | 23.2 | 0.2 | 0.3 |
| | 550 | 10.9 | 7.7 | 0.6 | 0.8 |

Reaction conditions: As shown for Table 6.1.

[a] These conversion values were measured once but based on their variabilities, an estimate of the 95% confidence limit on these values for CO conversion and the ratio of $CH_4$ to CO is typically ±20% and ±0.1 for silica-supportediron and ±20% and ±0.1 for nickel catalyst.

Catalytic activity of silica-supported iron and nickel based catalyst synthesized by the swelling in method, using iron nitrate and nickel nitrate as precursor was also studied. Table 6.5 shows CO conversions and ratios of methane formed to CO converted for 2.5, 5, and 10% silica-supported iron and nickel catalyst. In view of silica-supported iron catalyst, it can be seen that 2.5% $Fe/SiO_{2(SIM)}$ is the most active catalyst while 5% $Fe/SiO_{2(SIM)}$ catalyst has the least CO conversion with the highest amount of methane. The catalytic behaviour shown by 2.5% $Fe/SiO_{2(SIM)}$ catalyst suggests that increase in temperature did not have significant sintering effect on its active sites. The poor catalytic activity of 5% $Fe/SiO_{2(SIM)}$ catalyst is possibly due to high rate of deactivation by sintering and surface covering of the metallic iron phases by carbon deposition due to disproportionation of carbon as evidenced by the high amount of methane produced [16].

Catalytic performance of silica-supported nickel based catalyst shows that 5% $Ni/SiO_{2(SIM)}$ has the best catalytic activity while 10% $Ni/SiO_{2(SIM)}$ catalyst is the least active and as expected, it can be observed that regardless of the reasonable CO conversion, the amount of methane produced by this catalyst is relatively quite high when compared to most of the silica-supported cobalt based catalyst [17, 18]. 5% $Ni/SiO_{2(SIM)}$ catalyst has better activity due to less deactivation by sintering as reaction temperature increases while 10% $Ni/SiO_{2(SIM)}$ catalyst seems to suffer from more sintering effect and slight carbon deposition. Meanwhile, the high amount of methane produced by nickel catalyst makes it less favourable for Fischer-Tropsch synthesis [ 18].

### 6.1.2. Effect of cobalt precursor on catalytic performance of silica-supported cobalt catalyst

The influence of cobalt precursor on catalytic activity of silica-supported cobalt based Fischer-Tropsch catalyst has been demonstrated in the literature [7, 19, 20]. In Tables 6.1 -

6.3 (as already shown), it can be seen overall that the catalyst prepared by the swelling in method using cobalt nitrate is the most active catalyst while the ones prepared from cobalt acetate has the least catalytic performance. This trend in catalytic behaviour is likely due to cobalt nitrate being more soluble in the methanol-swollen PDMS gel and therefore ends up more evenly dispersed on the catalyst support during the loading stage of the catalyst preparation. The result is in agreement with the work of Sirirat et al [22], where it was found that catalyst prepared from cobalt nitrate demonstrated the highest activity which was put down to ease of reduction to cobalt metal and a comparative absence of interactions between neighbouring metal crystallites and therefore little tendency to sintering. Others have reported similar results [21-22] that Fischer-Tropsch catalysts prepared from cobalt nitrate exhibited better dispersion and higher reducibility which resulted in higher concentrations of cobalt metal sites for CO chemisorption.

### 6.1.3. Effect of ruthenium addition on catalytic activity of silica-supported cobalt catalyst

The impact of noble metal addition such as ruthenium (between 0.05 – 0.5wt.%) on the catalytic behaviour of silica-supported cobalt catalyst in Fischer-Tropsch synthesis reaction has been well documented [24-27]. In this study the effect of 0.5 w/w % ruthenium on the catalytic activity of 2.5, 5 and 10% $Co/SiO_2$ catalyst prepared from cobalt nitrate by the swelling in method was investigated. Table 6.6 shows CO conversions and ratios of methane formed to CO converted for un-promoted and ruthenium promoted silica-supported cobalt catalyst. It can be seen that promoted silica-supported cobalt catalyst with the exception of 5 % $Co\text{-}N\text{-}Ru/SiO_{2(SIM)}$ generated less amount of methane than the unpromoted catalyst. This observation is in agreement with previous report by Haifeng et al. [25] where it was found that methane selectivity decrease, with increasing amount of ruthenium.

Table 6. 6. CO conversions and ratios of methane formed to CO converted as a function of temperature and time-on-stream for un-promoted and ruthenium promoted silica-supported cobalt catalyst prepared by the swelling in method

| Catalyst | Temp / °C | CO conversion / % with time on stream [a] | | Ratio $CH_4$ formed to CO converted with time on stream [a] | |
|---|---|---|---|---|---|
| | | 20mins | 60mins | 20mins | 60mins |
| 2.5 % Co-N/$SiO_{2(SIM)}$ | 350 | 40.4 | - | 0.6 | - |
| | 450 | 30.1 | - | 0.7 | - |
| | 550 | 14.2 | - | 1.0 | - |
| 2.5 % Co-N-Ru/$SiO_{2(SIM)}$ | 350 | 29.2 | - | 0.1 | - |
| | 450 | 7.2 | - | 0.5 | - |
| | 550 | 5.7 | - | 0.5 | - |
| 5 % Co-N/$SiO_{2(SIM)}$ | 350 | 55.5 | 22.2 | 0.1 | 0.2 |
| | 450 | 37.9 | 38.7 | 0.2 | 0.2 |
| | 550 | 13.8 | 11.5 | 0.3 | 0.4 |
| 5 % Co-N-Ru/$SiO_{2(SIM)}$ | 350 | 24.5 | 27.2 | 0.2 | 0.2 |
| | 450 | 27.4 | 18.4 | 0.2 | 0.4 |
| | 550 | 18.4 | 18.6 | 0.4 | 0.4 |
| 10 % Co-N/$SiO_{2(SIM)}$ | 350 | 73.3 | 78.9 | 0.1 | 0.1 |
| | 450 | 81.6 | 82.8 | 0.1 | 0.1 |
| | 550 | 36.6 | 30.8 | 0.1 | 0.2 |
| 10 % Co-N-Ru/$SiO_{2(SIM)}$ | 350 | 89.0 | 83.8 | 0.1 | 0.1 |
| | 450 | 78.0 | 79.3 | 0.1 | 0.1 |
| | 550 | 79.7 | 30.3 | 0.1 | 0.1 |

Reaction conditions: As shown for Table 6.1. Co-N = Decomposed cobalt nitrate. Co-N-Ru = Decomposed mixture of cobalt and ruthenium nitrates.

[a] These conversion values were measured once but based on their variabilities, an estimate of the 95% confidence limit on these values for CO conversion is typically ±15% and on the ratio of $CH_4$ to CO is typically ±0.1.

Here, it was suggested that ruthenium inhibits the formation of unreduced cobalt oxides ($Co^{2+}$ or $Co^{3+}$ species) which can catalyse the water gas shift reaction so as to increase the ratio of $H_2$/CO on the surface of cobalt active sites which eventually causes hydrogenation of carbon monoxide leading to more methane formation [25, 27]. It can also be seen that the catalyst containing ruthenium except 2.5 % Co-N-Ru/$SiO_{2(SIM)}$ catalyst has better catalytic performance. Although, CO conversion of 5 % Co-N/$SiO_{2(SIM)}$ seems to be slightly higher than 5 % Co-N-Ru/$SiO_{2(SIM)}$ catalyst but overall Ru-promoted catalyst has better catalytic activity in terms of its confidence limit. The better catalytic performance of the promoted catalyst is likely due to ruthenium forming Ru-Co bimetallic particles and to help decrease the amount of unreduced $Co^{2+}$ and $Co^{3+}$ species leading to an enrichment of more cobalt active sites on the surface of the catalyst support [24, 27].

The results demonstrate in-line with other works that the presence of ruthenium retards methane formation and improves catalytic performance of silica-supported cobalt based catalyst used for Fischer-Tropsch synthesis [24-25, 27].

## 6.2. Conclusions

Catalytic behaviour of all the catalyst prepared in this work was evaluated using high temperature low pressure Fischer-Tropsch synthesis. On examining what the influence of preparation method, cobalt content, temperature and time on stream would have on the catalytic performance of the catalyst, it was found that silica-supported cobalt based catalyst prepared by the novel (swelling in method) were slightly more active, generated less amount of methane and was less susceptible to deactivation by sintering and carbon deposition compared to the catalyst synthesized by incipient wetness technique. Silica-supported cobalt catalyst prepared by the swelling in method with 5 w/w % cobalt content was more active

than the catalyst containing 2.5 and 10 w/w % content. PDMS supported cobalt catalyst prepared by the swelling in method is the least active, which from every indication the choice of the polymeric support must have contributed to its poor catalytic behaviour. Silica-supported cobalt nanoparticles catalyst prepared by colloidal and swelling in methods demonstrated the highest catalytic activity with the least amount of methane in comparison to the rest silica-supported cobalt based catalyst studied in this thesis. Catalytic activity of silica-supported iron and nickel based catalyst prepared by the swelling in method were also tested. It was observed that the catalyst were also quite active in the chosen reaction conditions and as expected, silica-supported nickel catalyst generated the highest amount of methane in view of all the silica-supported catalysts that were investigated. On the discussion of cobalt precursor affecting catalytic performance of silica-supported cobalt based catalyst prepared by the swelling in method. It was shown that the catalyst prepared from cobalt nitrate is more active than the ones synthesized from cobalt acetate. Catalytic behaviour of ruthenium promoted silica-supported cobalt catalyst was also considered and it was found that the presence of ruthenium inhibited methane formation in comparison to the catalyst without ruthenium.

In overall conclusion, it has been shown that temperature and time on stream have effect on catalytic performance of the catalyst prepared by the swelling in and incipient wetness impregnation methods. The catalyst synthesized by the colloidal technique coupled with the swelling in method generated the least amount of methane and was the most active of all the catalysts studied in this thesis. Cobalt precursor and the addition of ruthenium influenced catalytic behaviour of silica-supported cobalt based catalyst prepared by the swelling in method.

**References**


1. Yan, Z.; Wang, Z.; Bukur, D.B.; Goodman, D.W. Fischer–Tropsch synthesis on a model $Co/SiO_2$ catalyst. *Journal of Catalysis*. **2009**, 268, 196.
2. Schulz, H.; Nie, Z.; Ousmanov, F. Construction of the Fischer–Tropsch regime with cobalt catalysts. *Catalysis Today*. **2002**, 71, 351.
3. Hu, J.; Yu, F.; Lu, Y. Application of Fischer–Tropsch Synthesis in Biomass to Liquid Conversion. *Catalysts*. **2012**, 2, 303.
4. Jahangiri, H.; Bennett, J.; Mahjoubi, P.; Wilson, K.; Gu, S. A review of advanced catalyst development for Fischer-Tropsch synthesis of hydrocarbons from biomass derived syn-gas. *Catalysis Science & Technology*. **2014**, 4, 2210.
5. Bartholomew, C.H. Mechanisms of catalyst deactivation. *Applied Catalysis A: General*. **2001**, 212, 17.
6. Tsakoumis, N.E.; Rønning, M.; Borg, Ø.; Rytter, E.; Holmen, A. Deactivation of cobalt based Fischer–Tropsch catalysts: a review. *Catalysis Today*. **2010**, 154, 162.
7. Girardon, J.-S.; Lermontov, A.S.; Gengembre, L.; Chernavskii, P.A.; Griboval-Constant, A.; Khodakov, A.Y. Effect of cobalt precursor and pretreatment conditions on the structure and catalytic performance of cobalt silica-supported Fischer–Tropsch catalysts. *Journal of Catalysis*. **2005**, 230, 339.
8. Shi, L.; Jin, Y.; Xing, C.; Zeng, C.; Kawabata, T.; Imai, K.; Matsuda, K.; Tan, Y.; Tsubaki, N. Studies on surface impregnation combustion method to prepare supported $Co/SiO_2$ catalysts and its application for Fischer–Tropsch synthesis. *Applied Catalysis A: General*. **2012**, 435, 217.
9. Gnanamani, M.K.; Jacobs, G.; Shafer, W.D.; Davis, B.H. Fischer–Tropsch synthesis: activity of metallic phases of cobalt supported on silica. *Catalysis Today*. **2013**, 215,13.

10. Park, J.-Y.; Lee, Y.-J.; Karandikar, P.R.; Jun, K.-W.; Ha, K.-S.; Park, H.-G. Fischer–Tropsch catalysts deposited with size-controlled $Co_3O_4$ nanocrystals: Effect of Co particle size on catalytic activity and stability. *Applied Catalysis A: General*. **2012**, 411, 15.

11. Escalera, E.; Ballem, M.A.; Córdoba, J.M.; Antti, M.-L.; Odén, M. Synthesis of homogeneously dispersed cobalt nanoparticles in the pores of functionalized SBA-15 silica. *Powder Technology*. **2012**, 221, 359.

12. Adam, F.; Andas, J.; Rahman, I.A. The Synthesis and Characterization of Cobalt-Rice Husk Silica Nanoparticles. *The Open Colloid Science Journal*. **2011**, 4, 12.

13. Balela, M.D.L.; Lockman, Z.; Azizan, A.; Matsubara, E.; Amorsolo Jr, A.V. Protective Agent-Free Synthesis of Colloidal Cobalt Nanoparticles. *Journal of Physical Science*. **2008**, 19, 1.

14. Li, J.; Xu, Y.; Wu, D.; Sun, Y. Hollow mesoporous silica sphere supported cobalt catalysts for F–T synthesis. *Catalysis Today*. **2009**, 148, 148.

15. Gual, A.; Godard, C.; Castillón, S.; Curulla-Ferré, D.; Claver, C. Colloidal Ru, Co and Fe-nanoparticles. Synthesis and application as nanocatalysts in the Fischer–Tropsch process. *Catalysis Today*. **2012**, 183, 154.

16. Eliason, S.A.; Bartholomew, C.H. Reaction and deactivation kinetics for Fischer–Tropsch synthesis on unpromoted and potassium-promoted iron catalysts. *Applied Catalysis A: General*. **1999**, 186, 229.

17. Chai, G.-Y.; Falconer, J.L. Alkali promoters on supported nickel: Effect of support, preparation, and alkali concentration. *Journal of Catalysis*. **1985**, 93, 152.

18. Vannice, M.A. The catalytic synthesis of hydrocarbons from $H_2$:CO mixtures over the Group VIII metals: V. The catalytic behavior of silica-supported metals. *Journal of Catalysis*. **1977**, 50, 228.

19. Rosynek, M.P.; Polansky, C.A. Effect of cobalt source on the reduction properties of silica-supported cobalt catalysts. *Applied Catalysis*. **1991**, 73, 97.

20. Panpranot, J.; Kaewkun, S.; Praserthdam, P.; Goodwin, Jr. J.G. Effect of cobalt precursors on the dispersion of cobalt on MCM-41. *Catalysis letters*. **2003**, 91, 95.

21. Rojanapipatkul, S.; Goodwin Jr. J. G.; Praserthdam, P.; Jongsomjit, B. Effect of Cobalt Precursors on Properties of $Co/CoAl_2O_4$ Catalysts Synthesized by Solvothermal Method. *Engineering Journal*. **2012**, 16, 4.

22. Iglesia, E. Design, synthesis, and use of cobalt-based Fischer-Tropsch synthesis catalysts. *Applied Catalysis A: General*. **1997**, 161, 59.

23. Girardon, J.-S.; Quinet, E.; Griboval-Constant, A.; Chernavskii, P.A.; Gengembre, L.; Khodakov, A.Y. Cobalt dispersion, reducibility, and surface sites in promoted silica-supported Fischer–Tropsch catalysts. *Journal of Catalysis*. **2007**, 248, 143.

24. Huang, L.; Xu, Y. "Studies on the interaction between ruthenium and cobalt in supported catalysts in favor of hydroformylation." *Catalysis letters*. **2000**, 69, 145.

25. Xiong, H.; Zhang, Y.; Liew, K.; Li, J. Ruthenium promotion of Co/SBA-15 catalysts with high cobalt loading for Fischer–Tropsch synthesis. *Fuel Processing Technology*. **2009**, 90, 237.

26. Tsubaki, N.; Sun, S.; Fujimoto, K. Different functions of the noble metals added to cobalt catalysts for Fischer–Tropsch synthesis. *Journal of Catalysis*. **2001**, 199, 236.

27. Rodrigues, J.J.; Pecchi, G.; Fernandes, F.A.N.; Gláucia, M.; Rodrigues, F. Ruthenium promotion of Co/SBA-15 catalysts for Fischer-Tropsch synthesis in slurry-phase reactors. *Journal of Natural Gas Chemistry*. **2012**, 21, 722.

# CHAPTER 7

# General conclusions and future work

This chapter covers summary of all the results presented in this thesis as well as recommendations for future work.

## 7.1. General conclusions

The overall objective of this work was to develop an alternative and novel method for the synthesis of silica-supported cobalt catalyst for Fischer-Tropsch synthesis

In chapter 4, a preliminary study on thermal synthesis and characterisation of porous silica using Polydimethylsiloxane (PDMS) as the starting material was reported. The results obtained showed that when PDMS is isothermally heat treated at a certain temperature for almost 24 hours, it only decomposes from its initial flexible state to brittle due to loss of plasticizers without conversion to $SiO_2$. FTIR, XRD and nitrogen adsorption characterisation confirmed thermal characterisation data that PDMS undergoes complete conversion from its polymeric form to porous silica at temperature range between 450 and 500°C. Synthesized porous silica at this temperature range also has the best surface area and pore volume. Isothermal studies on the synthesized porous silica indicated that increase in isothermal time at constant temperature as well as increase in temperature at a constant time has adverse impact on its textural properties. Nitrogen adsorption desorption isotherm of the silica powder suggested that it is microporous with the presence of some mesopores. Meanwhile, it was considered that this same approach used in preparing silica powder could be very viable as a one-step synthesis of silica-supported catalyst for Fischer-Tropsch synthesis.

In chapter 5, the swelling in method was successfully employed to prepare silica-supported cobalt, iron and nickel based Fischer-Tropsch catalyst where the oxidative thermal characterisation results showed that the initial PDMS support for the catalyst prepared by the swelling in method and calcined in air decomposed to silica powder. PDMS supported cobalt based catalyst was also thermally decomposed under vacuum in the presence of only nitrogen and it was discovered that the polymeric form of PDMS was still retained. Data from FTIR and XRD confirmed thermal characterisation results. Consistency in reduction of surface area

and pore volume by the entire catalyst prepared by the swelling in method as percentage loading of the different metals increases suggested that oxides of the metals were present inside the silica pores. The same trend was displayed by silica-supported cobalt based catalyst prepared by the incipient wetness method. Meanwhile, nitrogen adsorption – desorption analysis showed that the catalyst synthesized by the swelling in method has the highest surface area and pore volume compared to the catalyst prepared by the incipient wetness impregnation method. The estimated values obtained for XRD particles sizes of all synthesized silica-supported cobalt based catalyst using both the swelling in and incipient wetness impregnation methods has previously been demonstrated to be in good agreement with experimental values. Typical isotherms and BJH distribution for pore size of the catalyst prepared by the swelling in and incipient wetness methods indicated that most of them are microporous with the presence of mesopores.

In chapter 6, results obtained from catalytic activity in Fischer-Tropsch synthesis of the catalyst prepared using both the swelling in and incipient wetness impregnation methods suggested that the routes of synthesis, cobalt content and reaction temperature and time on stream had influence on the catalyst performance. Here, it was shown that silica-supported cobalt catalyst prepared by the swelling in method was slightly more active, generated less methane and less susceptible to deactivation by sintering and carbon deposition in comparison to the catalyst prepared by the incipient wetness impregnation method. Silica-supported cobalt catalyst prepared by the swelling in method with cobalt content of 5 w/w % was more active than the catalyst containing 2.5 and 10 w/w %. Catalytic performance of PDMS supported cobalt catalyst prepared by the swelling in method indicated that it is not very promising for Fischer-Tropsch synthesis reaction. Silica-supported cobalt nanoparticles catalyst prepared by the colloidal and swelling in methods demonstrated the highest catalytic activity with the least amount of methane in comparison to the rest silica-supported cobalt

based catalyst studied in this thesis. Catalytic activity of silica-supported iron and nickel based catalyst prepared by the swelling in method were also found to be quite active except that one of the silica-supported iron catalyst deactivated quite rapidly as temperature and time on stream increases which suggests the possibility of sintering or carbon deposition on the surface of metallic iron phases. On the discussion of cobalt precursor affecting the catalytic performance of synthesised silica-supported cobalt based catalyst. It was shown that the catalyst prepared from cobalt nitrate is more active than the catalyst synthesized from cobalt acetate. Finally, it was observed that the presence of ruthenium seems to minimise methane formation in comparison to the catalyst without ruthenium. In view of these results, some possible recommendations were made for future work.

## 7.2. Recommendations for future work

To carry out quantitative catalytic performance testing of silica-supported cobalt based catalyst prepared by the swelling in method using an ideal Fischer-Tropsch reaction condition which entails low temperature and high pressure in a fixed bed reactor. The catalyst should be used to study external mass transfer limitation, so as to find out the optimum reaction conditions that will readily encourage higher hydrocarbons chain growth formation.

The swelling in method should be used to synthesize and characterise bimetallic catalyst using cobalt, iron, nickel, platinum and palladium metals and be used to study the influence of varying each metal composition, optimum percentage loading of catalyst on the support, precursor and promoters (Ru, Re, Pt and Pd) on catalytic performance. Meanwhile, another study that will be worth carrying out, is to examine the extent of catalytic deactivation in Fischer-Tropsch synthesis by employing XRD, SEM and other surface chemistry related analytical techniques.

# Appendix

This section includes appendices showing a typical worked example of percentage cobalt content in silica as catalyst support, Mass Spectrometry diagram of ion current against temperature and time of 10% Co-A/$SiO_{2(SIM)}$ catalyst in Fischer-Tropsch synthesis, T-plot of porous silica powder synthesized from polydimethylsiloxane, BJH distribution of pore size for silica-supported cobalt, iron and nickel based catalyst prepared by the swelling in method as well as that of silica-supported cobalt catalyst prepared by incipient wetness impregnation technique. It also contains a typical worked examples to show percentage CO conversion, $CH_4$ formation as well as the ratio of $CH_4$ formed to CO converted of 10% Co-A/$SiO_{2(SIM)}$ catalyst and a typical $N_2$ adsorption-desorption isotherm of porous silica synthesized from PDMS.

## Appendix 1

A typical worked example to show calculation of 10 wt.% of cobalt content in PDMS (which decomposed by oxidation to silica) using cobalt (II) acetate tetrahydrate.

3.86g of cobalt (II) acetate tetrahydrate was dissolved in 5ml of methanol to obtain 3.1 mol/L solution.

Molecular weight of cobalt (II) acetate tetrahydrate = 249.08g/mol

Molar mass of cobalt = 58.933g/mol

Amount of cobalt present in 3.86g of dissolved cobalt salt

= 3.86g/mol × 58.933g/mol ÷ 249.08g/mol = 0.9134615g of Co

Mass of PDMS as initial support of catalyst = 8g

Therefore, 10 wt.% of silica-supported cobalt catalyst

= 0.9134615 ÷ (0.9134615 + 8) × 100 = ≈10.3%

This worked example was used to calculate percentage by weight of all the catalysts studied in this thesis

## Appendix 2

A typical mass spectrometry plot of ionic current of CO and methane against temperature and time of 10% Co-A/$SiO_{2(SIM)}$ catalyst in Fischer-Tropsch synthesis

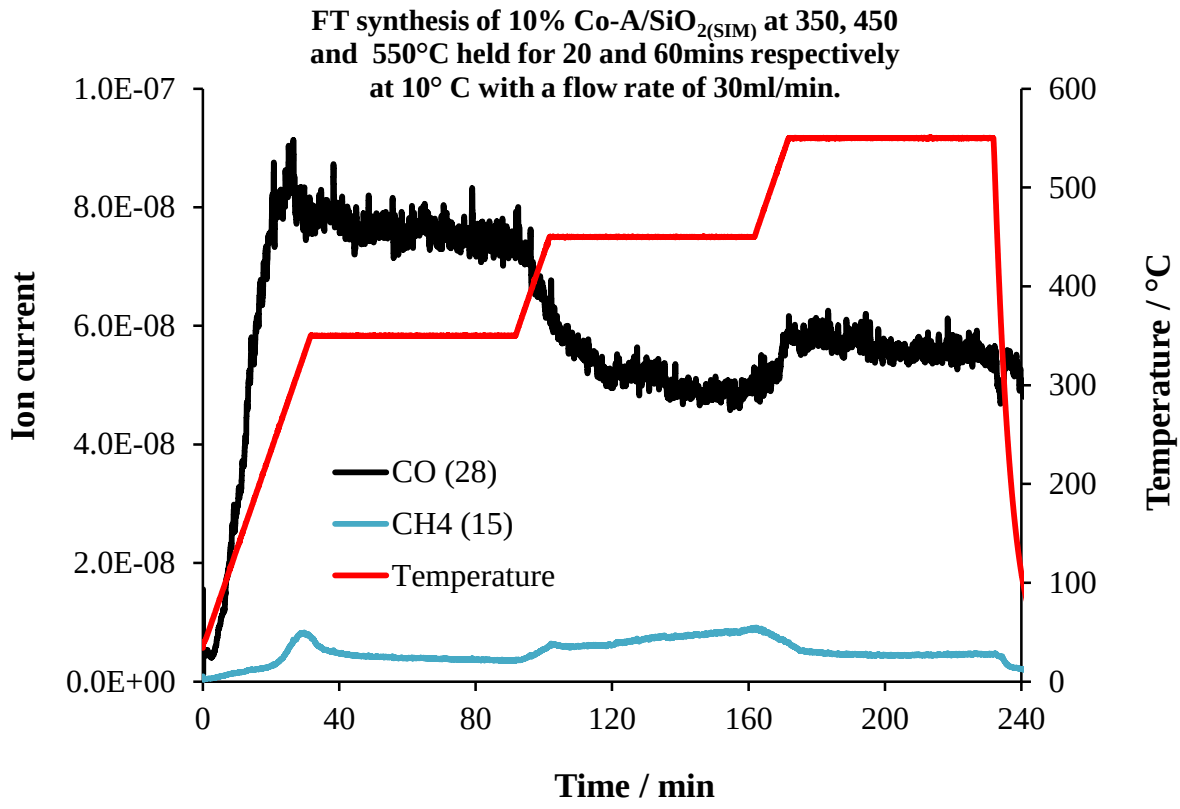


## Appendix 3

A typical worked example to show calculation of percentage CO conversion using 10% Co-A/$SiO_{2(SIM)}$ catalyst at 350°C held for 20 mins on stream.

$$\text{CO conversion / \%} = \text{normalised ion current level of } \frac{\text{CO (before reaction - after reaction)}}{\text{CO (before reaction)}} \times 100$$

Relative sensitivity of CO = 1.05

Normalised ion current level of CO = $\frac{\text{Ion current of CO}}{\text{Relative sensitivity of CO}}$

Ion current level of CO before reaction = $9.14 \times 10^{-8}$

Normalised ion current level of CO before reaction = $8.70 \times 10^{-8}$

Ion current level of reacted CO at 350°C held for 20 mins on stream = $7.61 \times 10^{-8}$

Normalised ion current level of reacted CO at 350°C held for 20 mins on stream = $7.25 \times 10^{-8}$

Hence,

$$\text{CO conversion / \%} = \frac{(8.70 \times 10^{-8} - 7.25 \times 10^{-8})}{(8.70 \times 10^{-8})} \times 100 = 16.7\%$$

Therefore,

CO conversion (%) of 10% Co-A/$SiO_{2(SIM)}$ at 350°C for 20 mins on stream = 16.7%

**Appendix 4**

A typical worked example to show calculation of $CH_4$ formation in percentage using 10% Co-A/$SiO_{2(SIM)}$ catalyst at 350°C held for 20 mins on stream.

$CH_4$ formation / % = normalised ion current level of $\frac{(CH_4 \text{ formed})}{(CH_4 \text{ formed + CO after reaction})} \times 100$

Relative sensitivity of $CH_4$ = 1.6

Normalised ion current level of $CH_4$ = $\frac{\text{Ion current level of } CH_4}{\text{Relative sensitivity of } CH_4}$

Ion current level of methane formed = $4.09 \times 10^{-9}$

Normalised ion current level of methane formed = $2.56 \times 10^{-9}$

Hence,

$$CH_4 \text{ formation / \%} = \frac{(2.56 \times 10^{-9})}{(2.56 \times 10^{-9} + 7.25 \times 10^{-8})} \times 100 = 3.41\%$$

Therefore,

$CH_4$ formation (%) of 10% Co-A/$SiO_{2(SIM)}$ at 350°C for 20 mins on stream = 3.41%

**Appendix 5**

A typical worked example to show calculation of ratio of $CH_4$ formation to CO conversion using 10% Co-A/$SiO_{2(SIM)}$ catalyst at 350°C held for 20 mins on stream.

$$\text{Ratio of } CH_4 \text{ formation to CO conversion} = \frac{CH_4 \text{ formation / \%}}{\text{CO conversion / \%}}$$

Hence,

$$\text{Ratio of } CH_4 \text{ formation to CO conversion} = \frac{3.41}{16.7} = 0.2$$

Therefore,

Ratio of $CH_4$ formation to CO conversion using 10% Co-A/$SiO_{2(SIM)}$ catalyst at 350°C held for 20 mins on stream = 0.2

**Appendix 6**

A typical t-plot of porous silica powder synthesized from PDMS heated at 10°C $min^{-1}$ from 50 to 500°C.

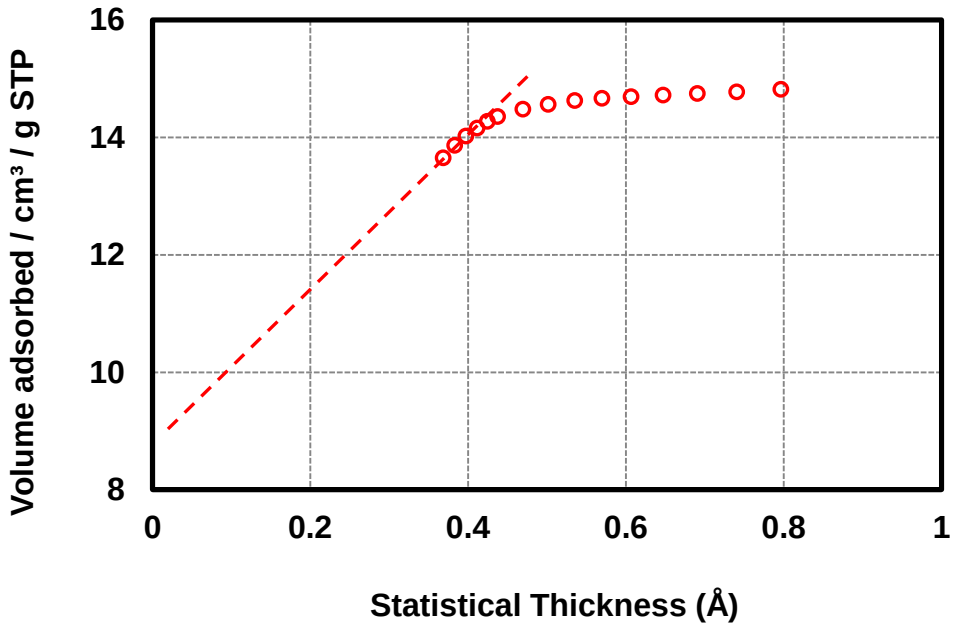


**Appendix 7**

A typical BJH pore size distribution of cobalt based silica-supported catalyst synthesized by the swelling in method

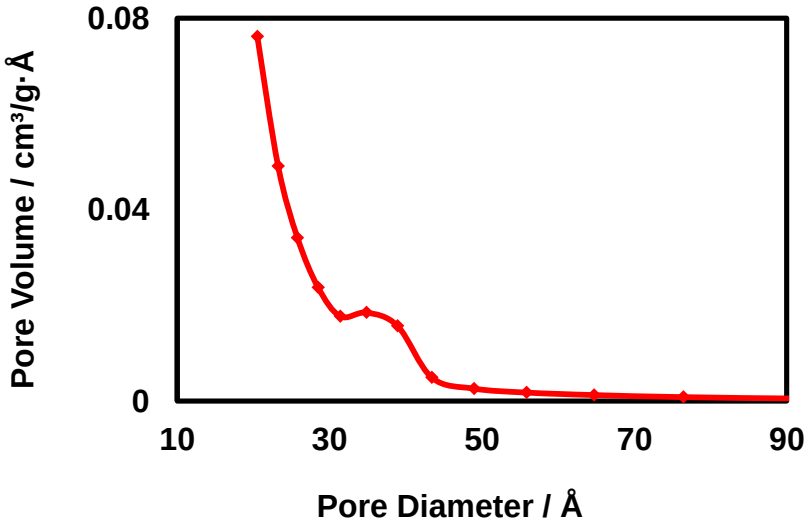

**Appendix 8**

A typical BJH pore size distribution of cobalt based silica-supported catalyst synthesized by incipient wetness impregnation method

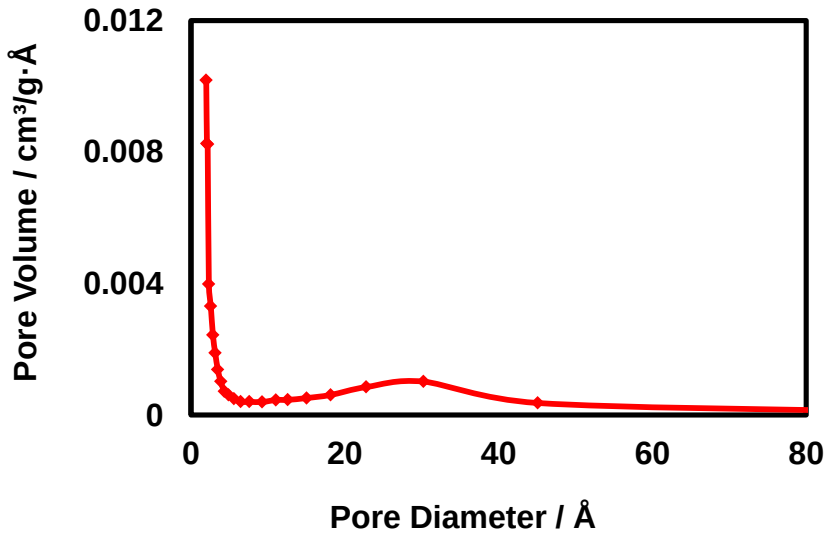


**Appendix 9**

A typical BJH pore size distribution of silica-supported cobalt nanoparticles catalyst synthesized by colloidal coupled with the swelling in method

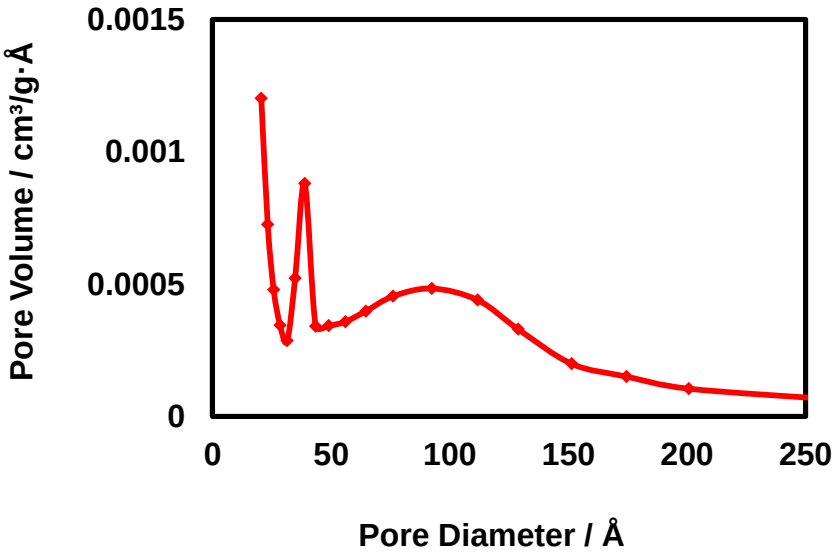

**Appendix 10**

A typical BJH pore size distribution of silica-supported iron catalyst synthesized by the swelling in method

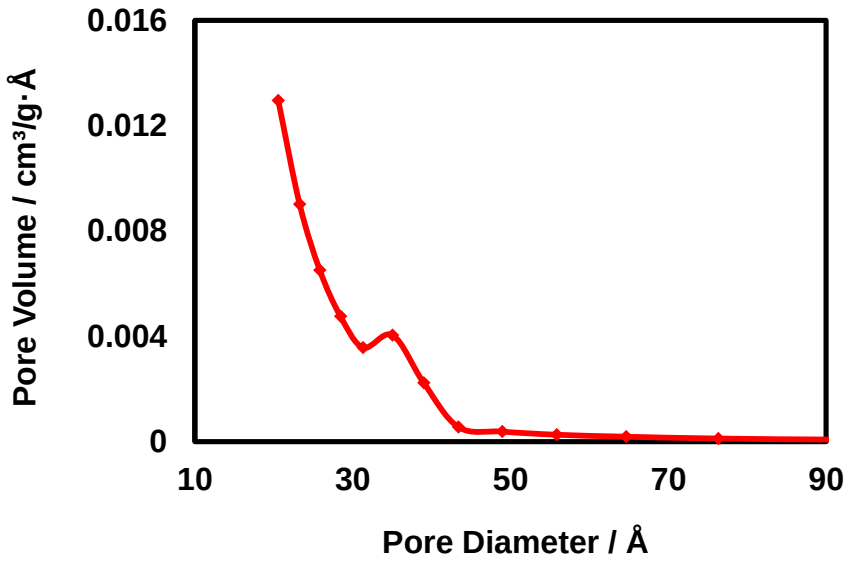


**Appendix 11**

A typical BJH pore size distribution of silica-supported nickel catalyst synthesized by the swelling in method